

DIGITAL ACCESS TO SCHOLARSHIP AT HARVARD
DASH.HARVARD.EDU

HARVARD LIBRARY


Search for Evidence of Dark Matter Production in Monojet Events With the ATLAS Detector

Link
http://nrs.harvard.edu/urn-3:HUL.InstRepos:37944978

Terms of use
This article was downloaded from Harvard University's DASH repository, and is made available under the terms and conditions applicable to Other Posted Material (LAA), as set forth at
https://harvardwiki.atlassian.net/wiki/external/NGY5NDE4ZjgzNTc5NDQzMGIzZWZhMGFlOWI2M2EwYTg

Accessibility
https://accessibility.huit.harvard.edu/digital-accessibility-policy

Share Your Story
The Harvard community has made this article openly available.
Please share how this access benefits you. Submit a story

©2016 – Emma Tolley
all rights reserved.

Search for Evidence of Dark Matter Production in Monojet Events with the ATLAS Detector

Abstract

Dark Matter production at colliders may be evinced in topologies with an energetic jet recoiling against large missing transverse momentum, known as the "monojet" final state. This thesis presents a search for new physics in a sample of monojet events obtained from proton–proton collision data corresponding to an integrated luminosity of $3.2\ \text{fb}^{-1}$ and center–of–mass energy $\sqrt{s} = 13$ TeV collected in 2015 with the ATLAS detector at the Large Hadron Collider. Monojet events are required to have at least one jet with a transverse momentum above 250 GeV and no leptons. Several signal regions are constructed with sequential missing transverse momentum thresholds ranging from $E_T^{\text{miss}} > 250$ GeV to $E_T^{\text{miss}} > 700$ GeV. The number of events observed in data is consistent with Standard Model predictions. In the absence of an excess, limits are placed on the dark matter production cross section and compared to constraints from direct detection experiments and other collider searches.

Contents

0 Introduction 1

I Dark Matter 3

1 Cosmological Dark Matter 4
1.1 Galactic Rotation Curves . . . 5
1.2 Galactic Clusters . . . 6
1.3 The Cosmic Microwave Background . . . 7
1.4 The Standard Model of Particle Physics . . . 10
1.5 WIMP Dark Matter . . . 11

2 Detecting Dark Matter 13
2.1 Dark Matter at Colliders . . . 14
2.2 Direct Detection . . . 15
2.3 Indirect Detection . . . 17
2.4 Interpretation Framework . . . 18
2.5 Relic Density Calculation . . . 23

II Experimental Background 26

3 The Large Hadron Collider 27
3.1 Accelerator Design . . . 27
3.2 Instantaneous luminosity . . . 29
3.3 Beam Cleaning and Beam Halo . . . 30

4 The ATLAS Detector 32
4.1 Magnetic Field . . . 34
4.2 Inner detector . . . 35
4.3 Calorimeters . . . 39
4.4 Muon spectrometer . . . 43
4.5 Trigger system . . . 45

5 Object Reconstruction in ATLAS 47
5.1 Inner Detector Tracks . . . 47
5.2 Jet Reconstruction and Calibration . . . 50
5.3 Jet Identification and Cleaning . . . 52
5.4 Electrons and Muons . . . 65
5.5 Missing Transverse Energy . . . 66

III Searching for Evidence of Dark Matter in Mono–Jet Events 68

6 Event Selection 69
6.1 Data Sample and Trigger . . . 70
6.2 Background and Signal Simulation . . . 70
6.3 Object Selection . . . 72
6.4 Signal Region Event Selection . . . 73

7 Background Estimation 76
7.1 W/Z + jets Background and Control Regions . . . 77
7.2 Non–Collision Background . . . 83
7.3 Multijet Background . . . 88
7.4 Experimental Systematics . . . 89
7.5 Theoretical Uncertainties . . . 92
7.6 Simultaneous Shape Fit . . . 94
7.7 Fit Results . . . 98

8 Results and Interpretation 101
8.1 Signal Region Yields . . . 101
8.2 Setting Limits . . . 105
8.3 Model Independent Limits . . . 106
8.4 Dark Matter Interpretation . . . 106
8.5 Monojet and Dijet Complementarity . . . 110

IV Looking Ahead 114

9 Ongoing Analysis Improvements 115
9.1 Photon Control Region . . . 116
9.2 Two-Dimensional Fit . . . 118

10 Conclusions 121

Appendix A Jet Quality Variables 123
A.1 Good and Fake Jet Topologies 123
A.2 Correlations between Jet Quality Variables 128
A.3 Jet Quality Variables at Low p_T 131

Appendix B Beam Background Tagging Efficiency 135

Appendix C Search for Dijet Resonances 138
C.1 Overview 138
C.2 Limits 139

References 142

Listing of figures

1.1 Rotation curve of a dwarf spiral galaxy 5
1.2 Diagram of gravitational lensing 6
1.3 The reconstructed mass density not associated with visible galaxies in a galactic cluster . . 7
1.4 Sensitivity of a CMB power spectrum model to four fundamental cosmological parameters 8
1.5 The CMB power spectrum 9
1.6 Summary of selected Standard Model cross-section measurements 10
1.7 Comoving number density of a WIMP in the early universe 12

2.1 Diagrams depicting DM detection methods 14
2.2 Illustration of a hypothetical limit on the DM-nucleon interaction cross-section 16
2.3 Exclusion upper limits for the spin-independent DM-nucleon cross section 17
2.4 Exclusion upper limits for the spin-dependent DM-nucleon cross-section 17
2.5 The gamma ray spectrum of the galactic center 18
2.6 Fermi-LAT upper limits on the DM annihilation cross-sections for various channels . . . 19
2.7 An example comparison of an LHC result to the Fermi-LAT limit 23
2.8 The predicted relic density Ωh^2 in the $(m_{\mathrm{med}}, m_\chi)$ plane 25

3.1 A diagram of the LHC ring with the four main experiments 28
3.2 Scattering and absorption of the beam halo by the LHC collimation system 31

4.1 A full diagram of the ATLAS detector 33
4.2 The ATLAS coordinate system 34
4.3 Geometry of magnet and predicted field integral 35
4.4 Layout of the ATLAS Inner Detector system 36
4.5 A candidate Z boson event in the dimuon decay with 25 reconstructed vertices 37
4.6 Layout of the ATLAS calorimeter system 39
4.7 Diagram of the EM calorimeter in the barrel 40
4.8 The LAr detector signal shape 42
4.9 The ATLAS muon system 44
4.10 ATLAS trigger rates 46

5.1 Illustration of particle interactions in ATLAS 48
5.2 Efficiency to extend a track 49

5.3 Illustration of the track impact parameters . . . 50
5.4 The stages of EM jet calibration . . . 51
5.5 Jet response of EM-scale jets . . . 52
5.6 Distributions of f_Q^{LAr}, f_Q^{HEC}, $\langle Q \rangle$, and E_{neg} . . . 55
5.7 Distributions of f_{EM}, f_{HEC}, and f_{max} . . . 57
5.8 Distributions of f_Q^{LAr} as a function of the electromagnetic fraction . . . 58
5.9 Distributions of f_{ch} and f_{ch}/f_{max} . . . 58
5.10 Distributions of f_{ch} as a function of the electromagnetic fraction . . . 59
5.11 Jet p_T, H_T^{miss}, η, and ϕ distributions for fake jets . . . 61
5.12 Jet quality selection efficiency as a function of η . . . 63
5.13 Jet quality selection efficiency as a function of p_T . . . 64
5.14 Electron reconstruction efficiency . . . 65
5.15 Muon reconstruction efficiency . . . 66

7.1 Distributions in the 1–muon control region for $E_T^{miss} > 250$ GeV . . . 79
7.2 Distributions in the 1–electron control region for $E_T^{miss} > 250$ GeV . . . 81
7.3 Distributions in the 2–electron control region for $E_T^{miss} > 250$ GeV . . . 82
7.4 The leading jet p_T and ϕ distributions of the data events passing the signal region selection without the tight cleaning criteria applied on the leading jet . . . 83
7.5 Selected distributions for the events in the signal region $E_T^{miss} > 250$ GeV that are tagged as non–collision background . . . 87
7.6 Measured distribution of the E_T^{miss} and jet multiplicity in the multijet control region . . . 88
7.7 Comparison of truth level quantities in the W and Z Monte Carlo samples . . . 91
7.8 Distribution of E_T^{miss} in the 1–muon control region for the 8TeV mono–jet analysis . . . 95
7.9 Values of the 21 normalization factors determined from the background–only fit. . . . 99
7.10 Distributions in the control regions before and after the fit . . . 100

8.1 Observed and expected events in the signal and control regions . . . 102
8.2 Measured distributions of the $E_T^{miss} > 250$ GeV signal region selection . . . 104
8.3 95% CL exclusion contours in the m_χ–m_A parameter plane . . . 108
8.4 95% CL upper limits on signal strength for different choices of the coupling $g = g_q = g_\chi$. 109
8.5 A comparison of the production cross section limits to the constraints from direct detection experiments . . . 110
8.6 Regions of 95% CL exclusion in the m_χ–m_A parameter plane for various ATLAS Dark Matter searches with dark matter coupling $g_{DM} = 1.0$ and quark coupling $g_q = 0.25$ . . 112
8.7 An alternate version of Figure 8.6 with exclusions computed for dark matter coupling $g_{DM} = 1.5$ and quark coupling $g_q = 0.1$ . . . 113

9.1 The p_T distributions and ratio of γ+jets and $Z(\mu\mu)$+jets . . . 117

9.2 The E_T^{miss} distributions and ratio of γ+jets and $Z(\mu\mu)$+jets . . . 117
9.3 Jet multiplicity in the signal region with the N_{jet} cut removed . . . 120
9.4 Expected excluded (m_χ, m_{med}) phase space for dark matter production when constraining the background uncertainties with the nominal and two–dimensional fitting schemes . . . 120

10.1 Projected sensitivities for near-future experiments . . . 122

A.1 Distributions of p_T, η, and ϕ for the good and fake jet selections . . . 125
A.2 Distributions of p_T as a function of η for good and fake jets . . . 126
A.3 Distributions of p_T as a function of ϕ for good and fake jets . . . 126
A.4 Distribution of η as a function of ϕ for good and fake jets . . . 127
A.5 Distribution of η as a function of t_{jet} for good and fake jets . . . 127
A.6 Distributions of f_{ch} as a function of f_{max} for good and fake jets . . . 128
A.7 Distributions of f_Q^{HEC} as a function of f_{HEC} for good and fake jets . . . 129
A.8 Distributions of f_Q^{HEC} as a function of $\langle Q \rangle$ for good and fake jets . . . 129
A.9 Distributions of f_Q^{LAr} as a function of $\langle Q \rangle$ for the good and fake jets . . . 130
A.10 Distributions of E_{neg} as a function of f_Q^{HEC} for good and fake jets . . . 130
A.11 Distributions of p_T, η, and ϕ in the loose good jets sample . . . 131
A.12 Distributions of f_Q^{LAr} , $\langle Q \rangle$, and f_Q^{HEC} in the loose good jets sample . . . 132
A.13 Distributions of f_{EM}, f_{HEC}, and f_{max} in the loose good jets sample . . . 133
A.14 Distributions of E_{neg} and t_{jet} in the loose good jets sample . . . 134
A.15 Distributions of f_{ch} and $f_{\text{ch}}/f_{\text{max}}$ in the loose good jets sample . . . 134

B.1 The BIB tagger efficiency as a function of jet time . . . 137
B.2 The evolution of the fake jet rate in the full dataset . . . 137

C.1 The reconstructed dijet mass m_{jj} distribution using the data collected by the ATLAS detector in 2015 and 2016 . . . 139
C.2 95%CL upper limits on predicted cross-section obtained from the $\sqrt{s} = 8$ TeV m_{jj} distribution . . . 140
C.3 95%CL upper limits on predicted cross-section obtained from the $\sqrt{s} = 13$ TeV m_{jj} distribution . . . 140
C.4 95%CL upper limits on predicted cross-section obtained from the $\sqrt{s} = 13$ TeV trigger-level m_{jj} distribution . . . 141
C.5 95%CL upper limits on predicted cross-section obtained from the $\sqrt{s} = 13$ TeV dijet + ISR m_{jj} distribution . . . 141

Listing of tables

3.1 LHC nominal and operational parameters 30

4.1 ATLAS inner detector parameters 36

6.1 Trigger efficiency for the E_T^{miss} trigger requirement 70
6.2 Signal region event selection criteria applied 74
6.3 Signal region selection cut flow for a simplified axial-vector model 75

7.1 Summary of the methods and control samples used to constrain the different background contributions in the signal regions 77
7.2 Data and SM background prediction, before and after the fit, in the 1–muon control region 79
7.3 Data and SM background prediction, before and after the fit, in the 1–electron control region 80
7.4 Data and SM background prediction, before and after the fit, in the 2–muon control region 81
7.5 Evaluation of the BIB tagger efficiency and mistag rate 84
7.6 Number of fake jet events in the full 3.2 fb^{-1} of data collected in 2015 85
7.7 Total amount of non–collision background in the specified regions 86
7.8 Amount of NCB in the signal region with and without applying the Tight cleaning criteria 86
7.9 `WZtransfer` uncertainties 92
7.10 Final V+jets systematic uncertainties 93
7.11 Data and background predictions in the control regions before and after the fit is performed for $E_T^{\text{miss}} > 250$ GeV 99

8.1 Data and SM background predictions in the signal region for several inclusive and exclusive missing transverse momentum selections 103
8.2 Data and SM background predictions in the signal region 103
8.3 Observed and expected 95% CL upper limits on the number of signal events 106

9.1 MC event yield and purity with 5 fb^{-1} luminosity 118
9.2 Impact of experimental systematics on signal region yield when constrained with a fit only to the control regions 119
9.3 Upper 95% CL limit on μ for different signal points using both the nominal fit and two-dimensional fit. 119

Acknowledgments

I owe a debt of gratitude to the many people whose time, help, and support made the completion of this thesis possible. An acknowledgments section that would truly do everyone justice might comprise a hundred-page document in and of itself. The following acknowledgments are certainly too terse but perhaps more readable.

First and foremost I would like to thank my advisor Masahiro Morii for his constant support and advice for the past five years. Thank you for your patience and perspective in everything from ATLAS magnetic field simulation to American election results.

Valerio Ippolito, thank you for teaching me how to properly pronounce *mai una gioia*. Also, you have my deep gratitude for your invaluable guidance, mentorship, and trust over the past two years. Thank you for taking the time to discuss the finer points of both physics and Italian cuisine.

Many of results presented in this thesis were produced as a collaborative effort with other physicists, especially Giuliano Gustavino, who I would additionally like to thank for being an excellent colleague and friend. David Lopez Mateos deserves thanks for his indispensable guidance in matters of jets and jetty physics, as well as Nikola Makovec and Caterina Doglioni for their advice and assistance during the jet cleaning saga.

I would like to thank Melissa Franklin, Joao Guimaraes da Costa, and John Huth for sharing valuable advice and interesting stories: never have I been more terrified at the prospect of kayaking. Matt Reece, thank you for your insightful comments and suggestions. I am grateful to Stefano Zambito for many interesting and fruitful discussions (especially those concerning muons), Chris Rogan for taking the time to explain the intricacies of the razor and jigsaw, and Geraldine Conti for sharing her expertise with me.

The past five years would not have been the same without my partners-in-crime[1] Tomo Lazovich and Siyuan Sun. Thank you for years of science, cooking, laughter. Upon conferral of my degree, I would humbly request that you refer to me only by the following title: "Queen Emma of Palfrey, cleaner of jets, hunter of dark matter, and khaleesi of the great electromagnetic ring"[2]. Also, I acknowledge that I shouldn't make bets with Tomo Lazovich that allow him to add sentences to my thesis.

All of the current and former graduate students deserve thanks: Laura Jeanty for showing me the ropes, Brian Clark for many varied and interesting conversations, Stephen Chan for superb tea, Tony Tong and Karri DiPetrillo for being the new *moral center*, Jennifer Roloff for fighting the good fight, Julia Gonski for picking up the torch, and Ann Wang for appreciating the birds. Gareth Kafka, LPPC confederate and taco Tuesday veteran, thank you for being a fellow beer snob. To all my cherished friends in Boston and dear friends in Geneva: thank you all for everything.

Finally, I would like to thank my mother and father, who have been there since the beginning, my brother, for his unwavering support, and David, for accompanying me on this journey.

[1] The crime is doing good physics.

[2] Alternative titles: 'The Doctor formerly known as Emma', 'DJ Jazzy Emma', 'The Emma-nator'.

0 Introduction

Several astrophysical and cosmological anomalies observed in the universe are inconsistent with our current understanding of gravitation and particle physics [1]. The existence of a new non–luminous, non–interacting "dark matter" (DM) particle could explain these phenomena. Several theories [2] propose that dark matter will take the form of a weakly interacting massive particle (WIMP), which would couple very weakly to the Standard Model and might be produced in proton-proton collisions at the LHC.

Although WIMP Dark Matter is invisible to the ATLAS detector, the creation of Dark Matter can be inferred when it is produced in association visible particles such as jets, photons, or electroweak bosons. This event topology is known as the "mono-X" signature, and is typified by a visible particle "X" recoiling against the missing transverse momentum vector missing transverse momentum . Mono-X searches with the ATLAS experiment [3] look for new physics in signal regions composed of events with large missing transverse momentum, strict quality requirements on "X", and a lepton veto to reduce contributions from processes such as $W \rightarrow \ell\nu$. Background processes are constrained using control regions constructed by

inverting signal region vetoes. The monojet search looks for dark matter production in association with jets from initial state radiation [4]. It is the most sensitive mono-X channel, as X (the jet) has α_s coupling to initial state quarks, as opposed to α for a photon or α_w for a W or Z boson.

This dissertation presents dark matter searches in monojet states with the ATLAS [3] experiment with proton–proton center–of–mass energies of 13 TeV in data corresponding to an integrated luminosity of 3.2 fb^{-1}. Results are interpreted within a simplified model framework, and the complementary of mono-X search limits with dijet resonance constraints and dark matter direct detection experiments are presented.

Chapter 1 provides an overview cosmological evidence for dark matter, including galactic rotation curves, and gravitational lensing, and the cosmic microwave background power spectrum. Weakly interacting massive particles are presented as a well-motivated candidate for dark matter.

Chapter 2 presents a short discussion of Dark Matter detection strategies, including reviews and indirect detection experiments and their complementarity with LHC searches. The WIMP simplified models used as benchmark signal models in this thesis are presented, and specific mediator and parameter choices are motivated.

Chapter 3 provides an overview of the Large Hadron Collider and Chapter 4 reviews the detector systems of the ATLAS experiment. Chapter 5 covers the reconstruction of physics objects at ATLAS, including jets, electrons, muons, and missing transverse energy.

Chapter 6 presents the criteria used to select events that are used in the analysis, and provides details on the Monte Carlo simulation used to estimate background an signal yields.

Chapter 7 covers the background estimation strategy. All of the backgrounds and the corresponding techniques for estimating their contributions to the monojet topology are discussed. Analysis uncertainties and the results of background fits are presented.

Chapter 8 presents the analysis results and interpretation. The final results are used to set limits on the production of Dark Matter. These LHC limits are then compared to the results of direct detection experiments and other LHC searches.

Chapter 9 discusses limitations of the analysis, possible avenues toward increasing sensitivity, and future prospects for searching for Dark Matter at the LHC. Chapter 10 concludes the thesis.

Part I

Dark Matter

1

Cosmological Dark Matter

The kinematics of galaxies, the dynamics of galactic clusters, and anisotropies of the cosmic microwave background are all incompatible with modern gravitation and known matter. These anomalies are all consistent with the existence of a new "dark" particle. This chapter presents an overview evidence for cosmological dark matter and WIMP dark matter motivations.

While many of these anomalies can be resolved by modifying dynamical laws rather than introducing a new kind of matter [5], there is no single modified dynamical theory that accounts for all of the anomalies while satisfactorily describing the observed universe [1]. As such, the following overview of cosmological anomalies discusses them in the framework of the Dark Matter hypothesis, rather than introducing additional contrivances.

1.1 Galactic Rotation Curves

Galactic kinematics indicate that something is missing from our understanding of cosmology or gravitation. The kinematics of a galaxy can be studied via the Doppler shift of the 21-cm line emitted by galactic hydrogen. In this way the circular velocity can be mapped as a function of the distance from the galactic center. The expected circular velocity according to Newtonian dynamics is $v(r) = \sqrt{GM(r)/r}$, where $M(r) \equiv 4\pi \int \rho(r) r^2 dr$ and $\rho(r)$ is the dynamical mass density profile. When compared with the distribution of visible mass in a galaxy, determined with optical surface photometry, a massive discrepancy between this visible mass and the dynamical mass is observed, as shown in Figure 1.1. Additional non-luminous "dark" mass in galaxies would account for this difference [1]. The fact that the observed $v(r)$ is approximately constant implies the existence of a dark halo with $M(r) \propto r$ and $\rho(r) \propto r^{-2}$.

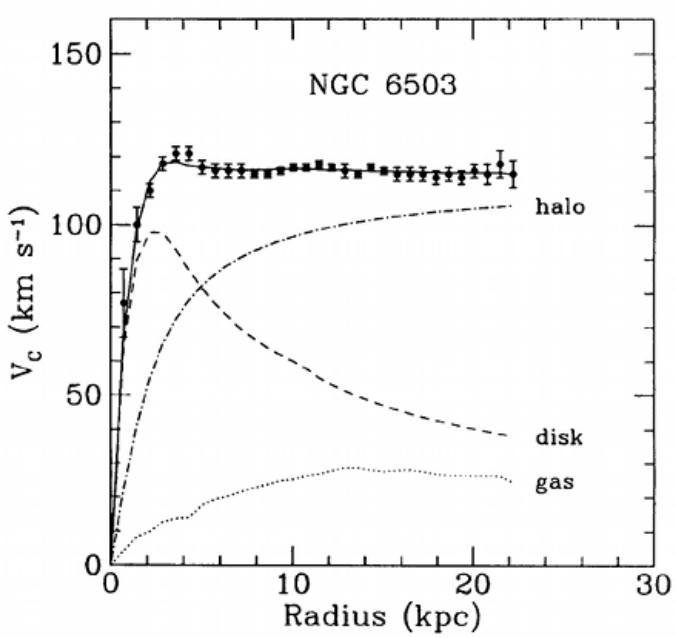


Figure 1.1: Rotation curve of dwarf spiral galaxy NGC 6503 [6]. Circular velocity v_c is plotted as a function of distance to the galactic center. The gravitational contributions of gas (dotted) and stellar matter (dashed) cannot explain the observed radial velocity. However, an additional halo of dark matter (dash-dotted) would explain the observed dynamics, shown as the three-parameter dark halo fit (solid).

1.2 Galactic Clusters

The mass and kinematics of a galactic cluster can be determined with several different methods. All of the techniques discussed below reveal a discrepancy between the visible and dynamical or gravitational mass of galactic clusters. Specifically, the visible mass is much smaller than the gravitational mass, implying the prevalence of invisible dark matter at galactic cluster scales.

The virial theorem [7] as applied to the observed distribution of radial galactic velocities relates the total kinetic energy of the objects to the total gravitational potential energy under the assumption that the objects are contained in the gravitational potential well. This technique yielded one of the first observations of dark matter in a galactic cluster via the substantial discrepancy between visible and dynamical mass [8]. Similarly, the x-rays produced via thermal bremsstrahlung of hot emitting gas can be used to estimate the kinematics of non–stellar mass, and reaveal a similar discrepancy [9].

Gravitational lensing can be used to determine the mass of heavy objects. According to General Relativity, light propagates along geodesics which deviate from straight lines when passing near intense gravitational fields. A strong field can bend light rays from a single source in a way that allows multiple rays to reach an observer, resulting in multiple images of the source object, as shown in Figure 1.2. The distortion and multiplication of background sources can be used to infer the shape of the gravitational potential well [10]. This principle is applied to galactic clusters to determine the total gravitational mass and examine the gravitational mass not associated with visible mass, as shown in Figure 1.3.

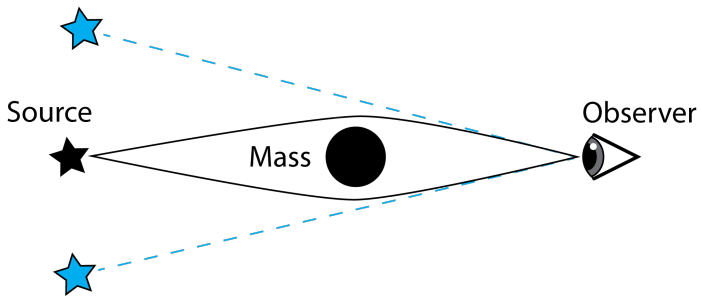


Figure 1.2: Diagram of gravitational lensing. A strong gravitational field can bend light rays from a single source in a way that allows multiple rays to reach an observer, resulting in multiple images of the source object.

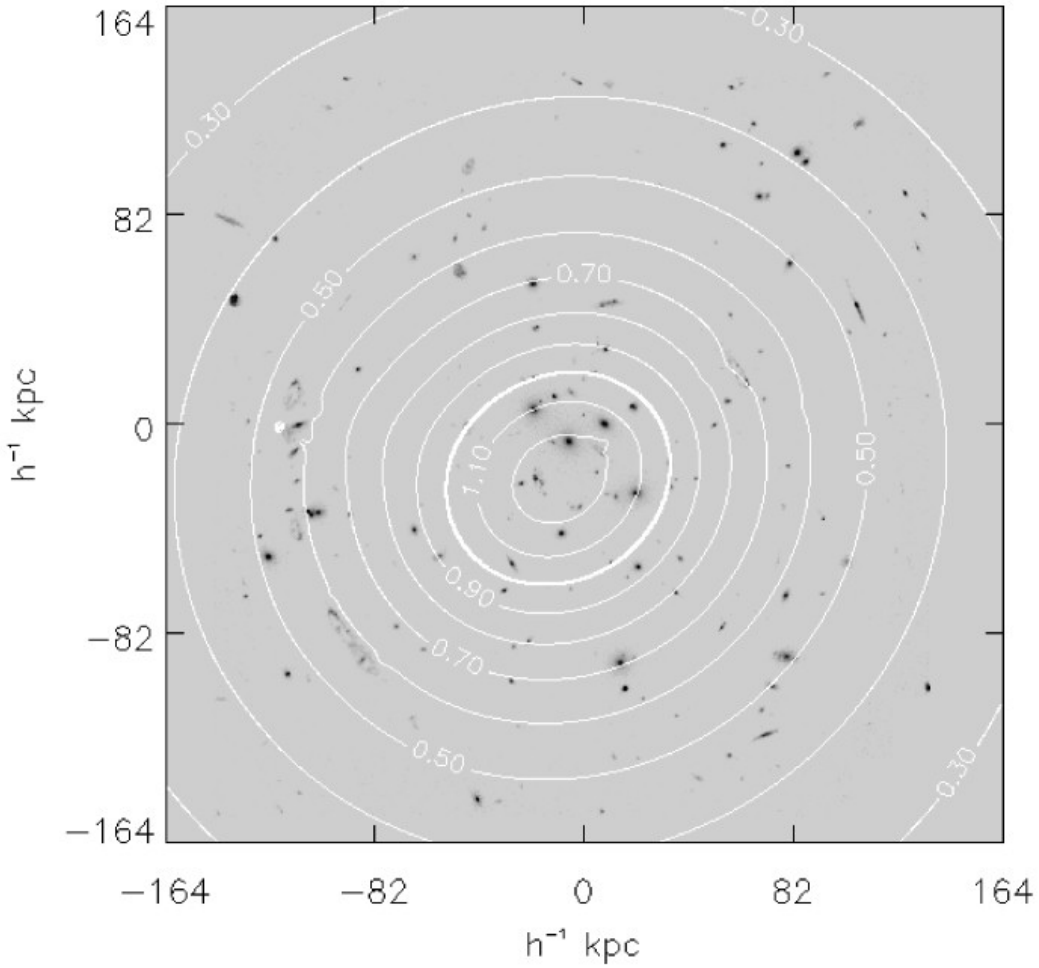


Figure 1.3: The reconstructed mass density not associated with visible galaxies in galactic cluster CL 0024 shown as a contour plot (white contours), superimposed on an image from the Hubble Space Telescope for reference [11]. The mass density is determined from gravitational lensing. On scales larger than 10 kpc the distribution of dark matter becomes smooth. Mass density contours for this dark mass are shown at intervals of $0.1\ \Sigma_c$ in projected mass density, where $\Sigma_c = 4497\ h\ d_{0.57}^{-1} M_\odot \mathrm{pc}^2$. The dimensionless distance ratio $d_{0.57}^{-1} = 1 \pm 0.15$ contains the uncertainty in the source redshift. h is a parameter in the range $0.5 < h < 0.75$ reflecting the uncertainty in the value of the Hubble constant H for the rate of expansion of the universe: $h = \frac{H}{100\ \mathrm{km/s/Mpc}}$.

1.3 The Cosmic Microwave Background

In the early universe, free electrons, photons, and baryons acted as a tightly coupled photon-baryon fluid [12]. As the universe expanded and cooled to 3000K, electrons combined with protons to form neutral hydrogen, decoupling photons from matter. The cosmic microwave background (CMB) is the thermal background radiation created by these photons.

The CMB is remarkably smooth, unlike the distribution of matter in the universe. While inhomogeneities in the distribution of matter grow due to gravitational instability, radiation pressure keeps the distribution of photons uniform. Nevertheless, there are small fluctuations in temperature of the CMB, known as the power spectrum. The position and amplitude of acoustic peaks in the power spectrum put strong constraints on cosmological density parameters [13], as shown in Figure 1.4.

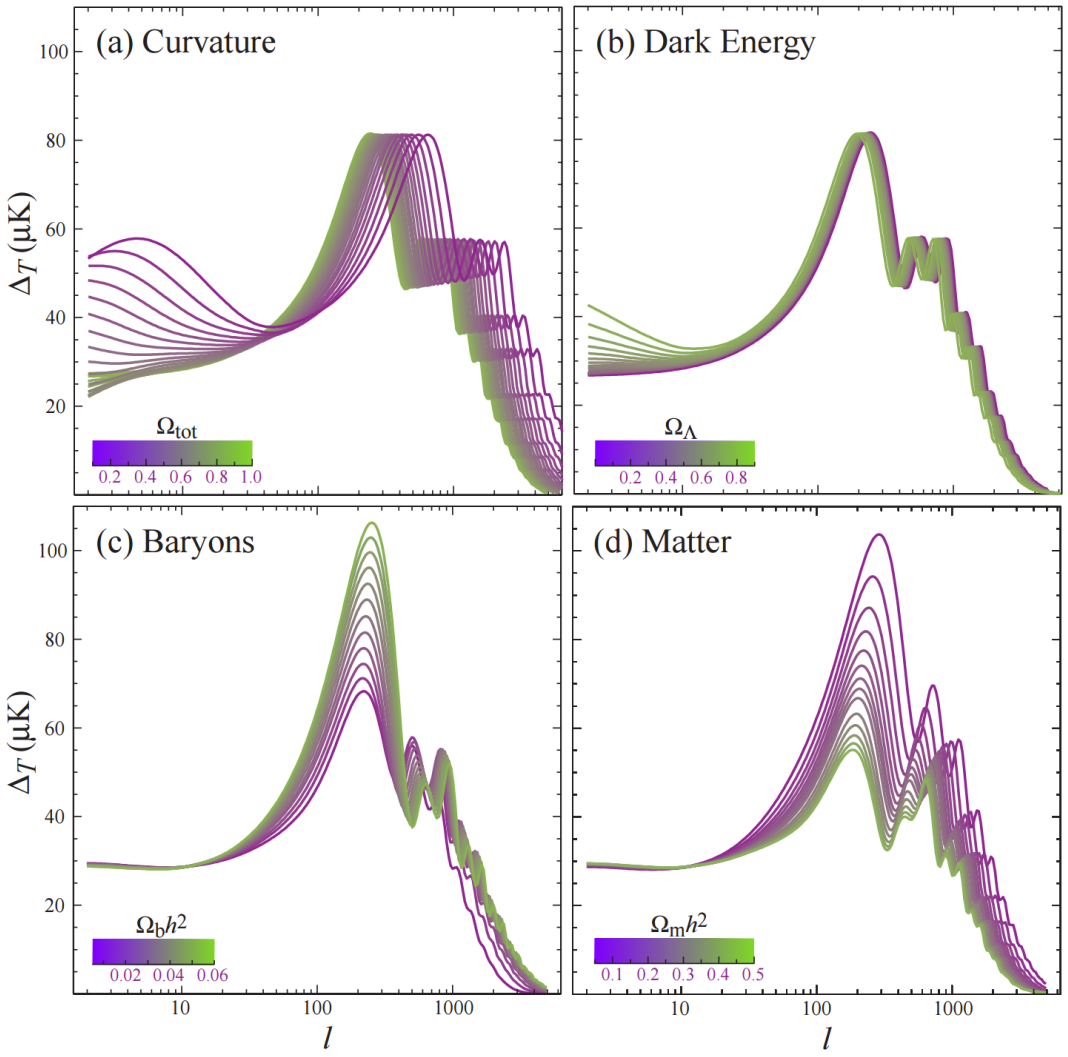


Figure 1.4: Sensitivity of a CMB power spectrum model to four fundamental cosmological parameters [13]: the curvature of the universe $\Omega_{\rm tot}$ (a), the dark energy density Ω_Λ (b), the physical baryon density $\Omega_b h^2$ (c), and the physical matter density $\Omega_m h^2$ (d). Measuring the position and amplitude of acoustic peaks in the observed power spectrum of Figure 1.5 puts strong constraints on these cosmological density parameters.

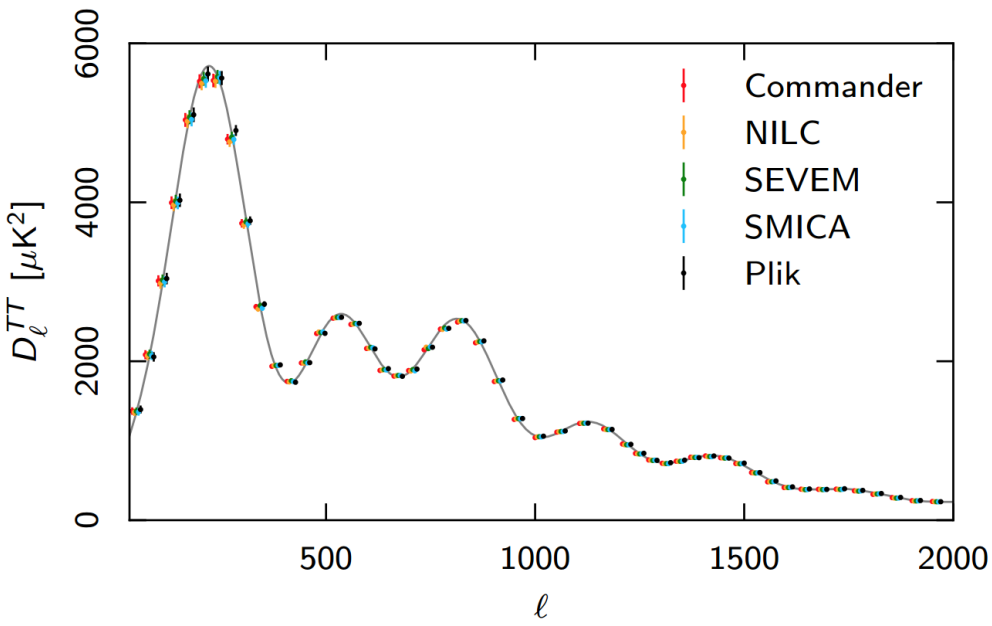


Figure 1.5: The CMB power spectrum measured by Planck [14], showing the fluctuations in temperature ΔD_ℓ^{TT} as a function of multipole moment ℓ for five foreground-cleaned maps of the CMB. The multipole moment is inversely proportional to the angular scale of the fluctuations $\ell \propto 1/\theta$.

The CMB power spectrum as measured by the Planck Collaboration [14] is shown in Figure 1.5. From analysis of the power spectrum, the abundance of baryonic matter in the universe is found to be:

$$\Omega_b h^2 = 0.022 \tag{1.1}$$

where h is the Hubble constant in units of 100 km s^{-1} Mpc$^{-}1$. However, the matter density is found to be:

$$\Omega_m h^2 = 0.14 \tag{1.2}$$

This discrepancy is attributed to non-baryonic dark matter, with a relic density of:

$$\Omega_c h^2 = 0.12 \tag{1.3}$$

Thus dark matter must comprise $\sim$ 30% of the total energy density of the universe and $\sim$ 86% of all matter in the universe.

1.4 The Standard Model of Particle Physics

The Standard Model of particle physics is a quantum field theory that describes all known fundamental particles and their interactions [15–20]. The Standard Model is a powerful and accurate model, successfully predicting a wide range of experimental results, as shown in Figure 1.6.

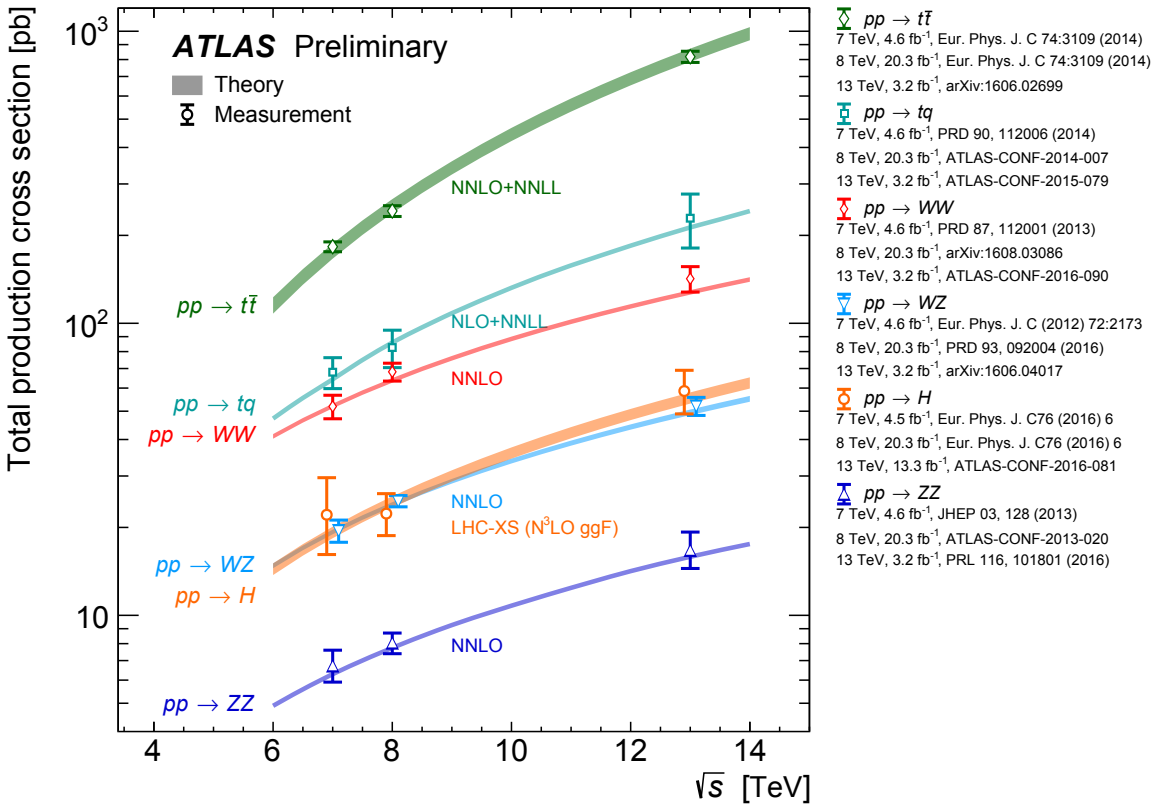


Figure 1.6: Summary of selected Standard Model cross-section measurements as a function of center–of–mass energy from 7 TeV to 13 TeV [21]. The Standard Model successfully predicts a wide range of experimental results for various energies and interactions.

In the Standard Model, the fundamental constituents of matter are spin $1/2$ particles known as fermions. Their interactions are mediated by integer spin particles called gauge bosons. Strong interactions are mediated by gluons g, electromagnetic interactions by the photon γ, and weak interactions by the $W^{\pm}$ and Z^0 bosons (often truncated to W and Z). Finally, the spin-zero Higgs boson H^0 arises from the Higgs mechanism of electroweak symmetry breaking. The fermions are arranged into three generations of quarks and leptons. Quarks (u, c, t and d, s, b) interact with all three forces, charged leptons (e, μ, τ) interact via

electromagnetic and weak interactions, and neutral leptons (ν_e, ν_μ, ν_τ) interact only via the weak force. Each particle also has a corresponding antiparticle with the same mass and opposite quantum numbers.

No particle in the Standard Model can explain the cosmological phenomena presented in Section 1. Dark Matter is nonluminous, noninteracting, and long–lived, which rules out the bosons, quarks, and charged leptons. Dark matter is non–baryonic, and thus cannot be a neutral combination of quarks such as the neutron. Finally, neutrinos are too light to account for the observed relic density of Dark Matter; the CMB power spectrum implies $\Omega_\nu h^2 < 0.0067$ [1]. A viable dark matter candidate must be found *beyond the Standard Model* (BSM).

1.5 WIMP Dark Matter

There are many potential particle candidates for dark matter, including sterile neutrinos [22], axions [23], and Kaluza–Klein states [24]. A stable weakly interacting massive particle is predicted by supersymmetry [2] and several other BSM theories [1]. This thesis will focus on the motivation and theoretical framework for thermal WIMP dark matter of the Dirac fermion variety.

WIMP dark matter would exist in thermal equilibrium in the early universe before freezing out and leaving a relic density, similar to the decoupling of the CMB. When the temperature of the universe T exceeds the mass of the particle m_χ, equilibrium abundance is maintained by annihilation of the particle with its antiparticle $\bar{\chi}$ into lighter Standard Model particles $\chi\bar{\chi} \rightarrow f\bar{f}$ and vice versa. However, once the universe cools to $T < m_\chi$, the equilibrium abundance drops exponentially until the rate for the annihilation reaction falls below the expansion rate H, at which point the interactions which maintain thermal equilibrium "freeze out" leaving a relic cosmological abundance of χ and $\bar{\chi}$. The relic density is approximately [2]:

$$\Omega_\chi h^2 \approx \frac{3 \times 10^{-27} \mathrm{cm}^3 \mathrm{s}^{-1}}{\langle \sigma v \rangle} \tag{1.4}$$

where $\langle \sigma v \rangle$ is the annihilation cross section. The relationship between, $\langle \sigma v \rangle$, the relic density, and universal expansion are shown in Figure 1.7.

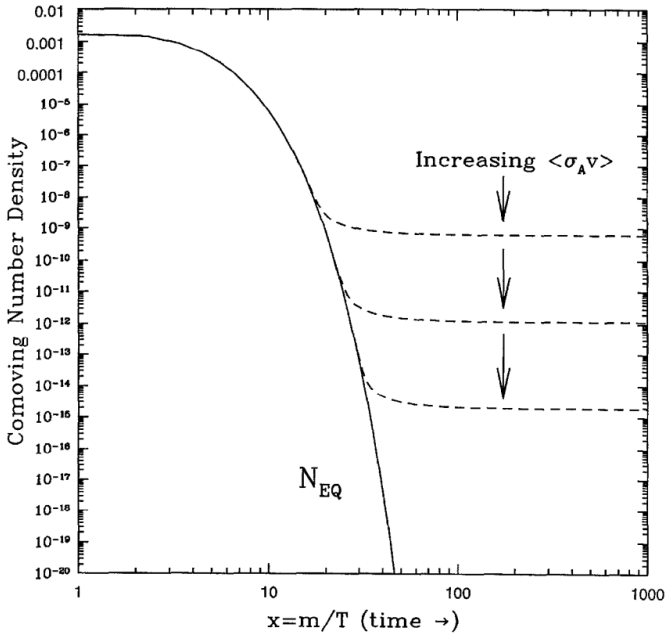


Figure 1.7: Comoving number density of a WIMP in the early universe [2]. The dashed curves show the predicted abundance as a function of the thermal annihilation cross section $\langle \sigma v \rangle$. The solid curve shows the equilibrium abundance as a function of x, a dimensionless parameter which scales as $1/T$. As the universe cools the interactions which maintain thermal equilibrium "freeze out" leaving a relic cosmological abundance of WIMPs. A higher thermal interaction cross section leads to a later freezeout and therefore lower relic density.

If a new particle with weak-scale interactions $g_{\text{weak}} \sim 0.1$ and a mass of ~ 100 GeV exists, then its annihilation cross section is approximately [2]:

$$\langle \sigma v \rangle \sim g_{\text{weak}}^4 (m)^{-2} \sim 10^{-25} \text{cm}^3 \text{s}^{-1} \tag{1.5}$$

Using Equation 1.4, this corresponds to an expected relic density is $\Omega_{\text{wimp}} h^2 \approx 0.01$. This is remarkably close to the measured dark matter relic abundance is $\Omega_c h^2 = 0.12$, especially considering that there is no reason for a weak-scale interaction to have any relation to the cosmological parameter Ω_c. This coincidence is known as the "WIMP miracle", and is compelling motivation to search for new particles at the electroweak scale.

2

Detecting Dark Matter

Although all evidence for dark matter is gravitational, the WIMP dark matter hypothesis allows for the possibility of detecting particle dark matter through other channels. If WIMPs were in thermal equilibrium with Standard Model particles in the early universe, they must have some nonzero coupling to ordinary matter. This chapter presents an overview of experimental strategies to detect cosmological dark matter, prospects for dark matter production and detection at the Large Hadron Collider, and simplified models of dark matter.

There are three principal strategies for detecting WIMP dark matter:

- Dark matter production at a particle collider via WIMP pair production.
- *Direct detection* of dark matter via cosmological WIMPs scattering off ordinary matter.
- *Indirect detection* of dark matter via cosmological WIMP pair–annihilation into ordinary matter.

These three processes are illustrated in Figure 2.1.

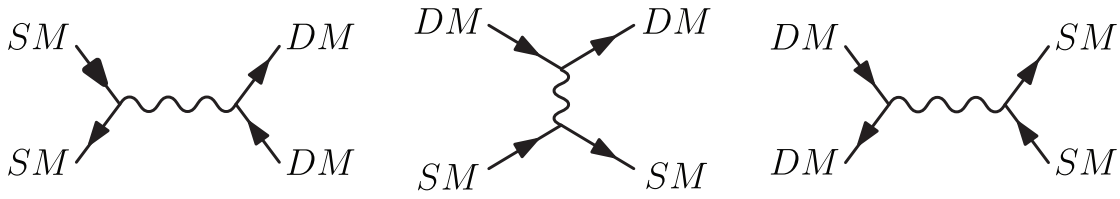


Figure 2.1: Diagrams depicting collider production of dark matter (left), direct detection (center), and indirect detection (right).

2.1 Dark Matter at Colliders

If dark matter couples to standard model particles, it may be possible to create dark matter at a particle collider through $f\bar{f} \to \chi\bar{\chi}$. One advantage of collider searches is that they are independent of astrophysical uncertainties on the density and velocity of cosmological dark matter.

There is no clean, distinct signature for dark matter production at a collider. Any WIMPs produced in a collision would be invisible to all detector systems. Therefore, instead of directly looking for dark matter production, collider searches look for WIMPs produced in association with other particles.

Invisible dark matter produced in association with a visible particle "X" appears as tracks and energy deposits consistent with X recoiling against nothing in a particle detector. Conservation of momentum can be applied to the energy measured in the transverse plane to construct the missing transverse momentum (E_T^{miss}). For an event in which all visible objects are perfectly reconstructed, the E_T^{miss} perfectly corresponds to the vector sum of transverse momentum of any invisible particles.

At a proton–proton collider such as the LHC [25], a hadronic jet is a natural choice for X, as a gluon is likely to be produced as initial state radiation from the initial colliding partons. The resulting final state with a jet and E_T^{miss} is called the monojet topology.

Even if a WIMP is discovered at the LHC, the existence of a new massive, stable, invisible particle would not be sufficient enough to prove that the new particle is cosmological dark matter. Results from direct detection experiments, indirect detection observations, and cosmological measurements are needed to validate any discoveries from collider searches.

2.2 Direct Detection

If our galaxy is embedded in a halo of WIMP dark matter, then hundreds to thousands of WIMPS must pass through every square centimeter of the Earth's surface every second [2]. Direct detection of these particles may be possible by observing the nuclear recoil from DM-nucleus elastic scattering, although the weak coupling of WIMPs would make this interaction very rare. Direct detection experiments attempt to measure, and distinguish from background, the tiny energy deposited by the very occasional DM-nucleus interaction. Alternatively, without any such signal these experiments set a strong limit on the rate of interactions between the local dark matter halo and atomic nuclei [26].

Two classes of interactions are probed with direct detection techniques. First, axial-vector and pseudoscalar interactions result from couplings to the spin content of a nucleon, and are therefore spin–dependent (SD). The cross sections for these interactions are proportional to $J(J+1)$, where J is the total nuclear spin. Because this coupling is independent of the number of nucleons in the target nucleus, little sensitivity is gained by using heavier target nuclei. However, scalar and vector mediator scattering is spin–independent (SI). The cross sections for both of these interactions increase dramatically with the mass of the target nuclei. For a scalar interaction with zero momentum transfer, the cross section for a WIMP to scatter from an atomic nucleus is:

$$\sigma = \frac{4m_r^2}{\pi}\big(Zf_p + (A-Z)f_n\big)^2 \tag{2.1}$$

where m_r is the DM-nucleon reduced mass, f_p is the DM-proton coupling, f_n is the DM-neutron coupling, and Z and $A-Z$ are the numbers of protons and neutrons in the nucleus, respectively. Similarly, the vector interaction cross section is:

$$\sigma = \frac{m_r^2}{64\pi}\big(2Zf_p + (A-Z)f_n\big)^2 \tag{2.2}$$

The direct detection limits on spin-independent interactions are much stronger than spin-dependent scattering in current experiments which use heavy atoms as targets [1].

There are large number of direct detection experiments use different target nuclei and different detection technologies. The relevant experiments for the results discussed in this thesis are XENON100 [27], LUX [28], and PICO [29, 30]. XENON100 and LUX employ liquid xenon detection masses in time-projection chambers to identify individual particle interactions, whereas PICO uses a bubble detector of superheated chlorofluorocarbon (Freon) as the active mass and is more sensitive to spin–dependent interactions. The qualitative dependence of various detector properties on a direct detection limit is shown in Figure 2.2. An overview of different direct detection limits is given in Figures 2.3 and 2.4.

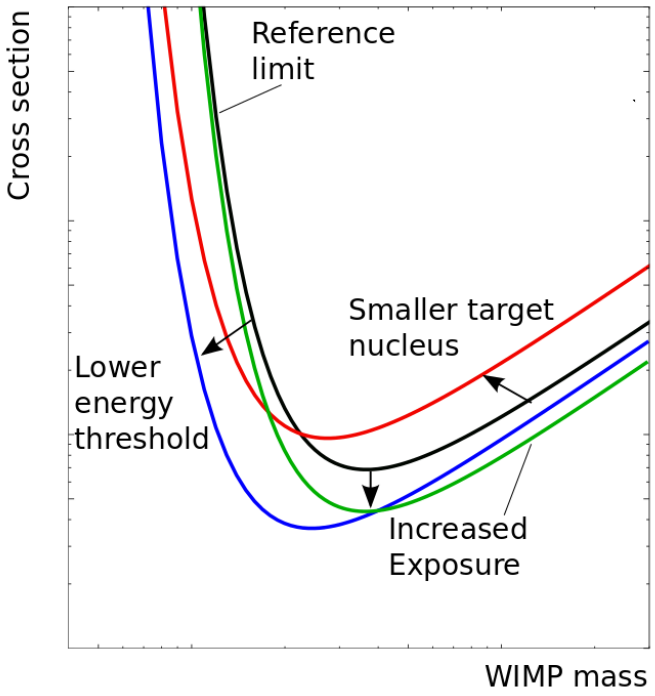


Figure 2.2: Illustration of a hypothetical limit on the DM-nucleon interaction cross-section[31] as function of WIMP mass (black) from a direct detection experiment (black), with limit variations corresponding to changes in the detector design or properties (colored lines).

Direct detection limits set some of the strongest bounds on WIMP-matter interactions. However, these experiments cannot detect light dark matter with $m_{\text{target}} \gg m_{\chi}$, when dark matter is too light for DM-nucleus recoil to be observable. Additionally, they lose sensitivity for high values of dark matter mass. Given the expected local dark matter relic density, as the mass of the particle becomes larger the expected dark particle flux through the earth becomes smaller.

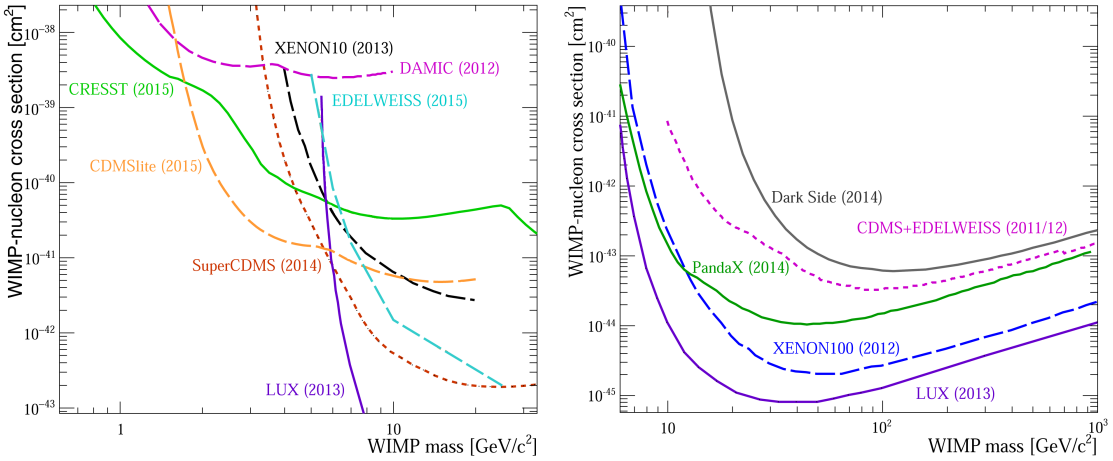


Figure 2.3: Exclusion upper limits for the spin-independent DM-nucleon cross section for low WIMP masses (left) and high WIMP masses (right)[31] .

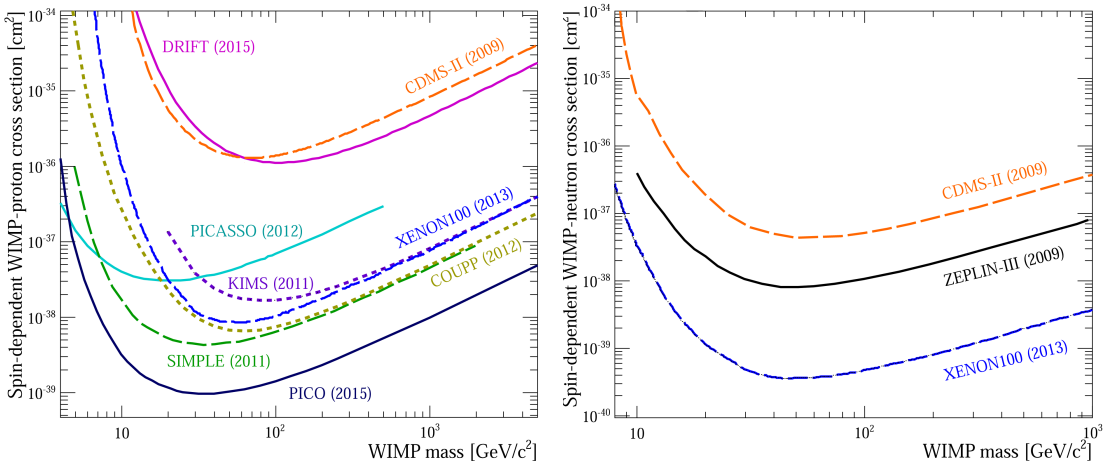


Figure 2.4: Exclusion upper-limits for the spin-dependent DM-nucleon cross-section assuming pure proton coupling (left) and pure neutron coupling (right). [31].

2.3 Indirect Detection

Cosmological WIMPs may pair–annihilate into Standard Model particles. Indirect detection experiments search for evidence of energetic particles created by dark matter annihilation. The Fermi Large Area Telescope [32] (Fermi-LAT) is an imaging, wide field-of-view, high-energy γ-ray telescope which is sensitive to γ-ray energies from 20 MeV to 300 GeV. Fermi-LAT places 95% CL constraints on the self-annihilation cross section from observations of dwarf spheroidal galaxies [33] for both $\chi\bar{\chi} \rightarrow \gamma\gamma$ and $\chi\bar{\chi} \rightarrow f\bar{f}$ with subsequent γ-ray cascades. Cross section limits as a function of m_χ are presented in Figure 2.6.

The galactic dark matter halo model predicts a high density of dark matter at the center of our galaxy. In fact,the inner Milky Way is expected to be the brightest source of dark matter annihilation radiation in the sky. However, this region is also astrophysically complex, containing the supermassive black hole Sagittarius A* and a myraid of other stellar objects. Separating the dark matter annihilation signal from backgrounds is challenging. Nevertheless, when known gamma ray sources are subtracted from the spectrum measured by Fermi–LAT, an excess remains in the galactic center. This excess could be consistent with dark matter annihilation [34] as shown in Figure 2.5, but may also be explained by more mundane sources of gamma radiation [35, 36].

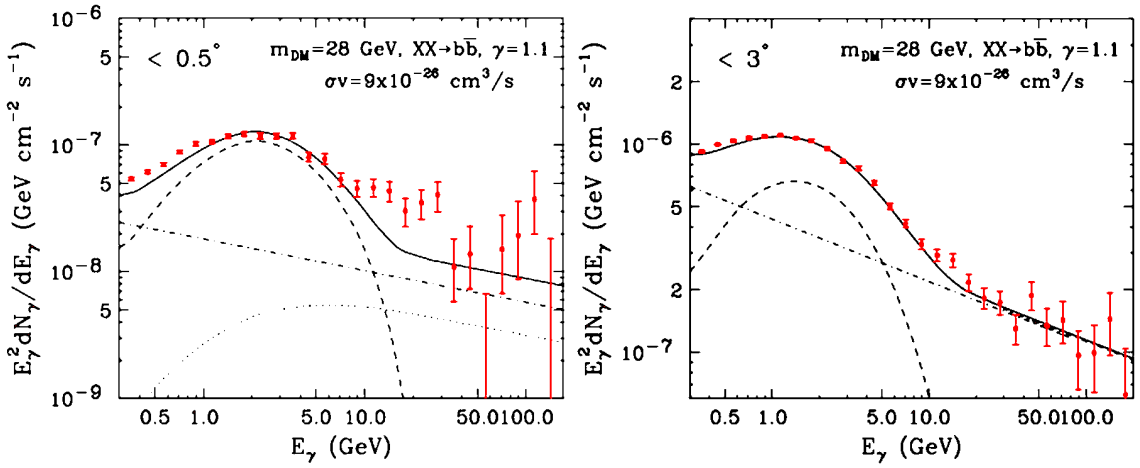


Figure 2.5: The gamma ray spectrum within $0.5°$ (left) and $3°$ (right) of the dynamical center of the Milky Way Galaxy, measured by Fermi-LAT [34]. The dashed line denotes the predicted spectrum from a 28 GeV dark matter particle annihilating to $b\bar{b}$ with a cross section of $\sigma v = 9 \times 10^{-26}$. The dotted and dot-dashed lines denote the contributions from the previously discovered TeV point source located at the Milky Way's dynamical center and the diffuse background, respectively. The solid line is the sum of these contributions. This excess may also be consistent with more mundane sources of gamma radiation [35, 36].

2.4 Interpretation Framework

A simplified model framework allows LHC dark matter results to be compared with direct and indirect dark matter detection experiments and dark matter relic density measurements [38, 39].

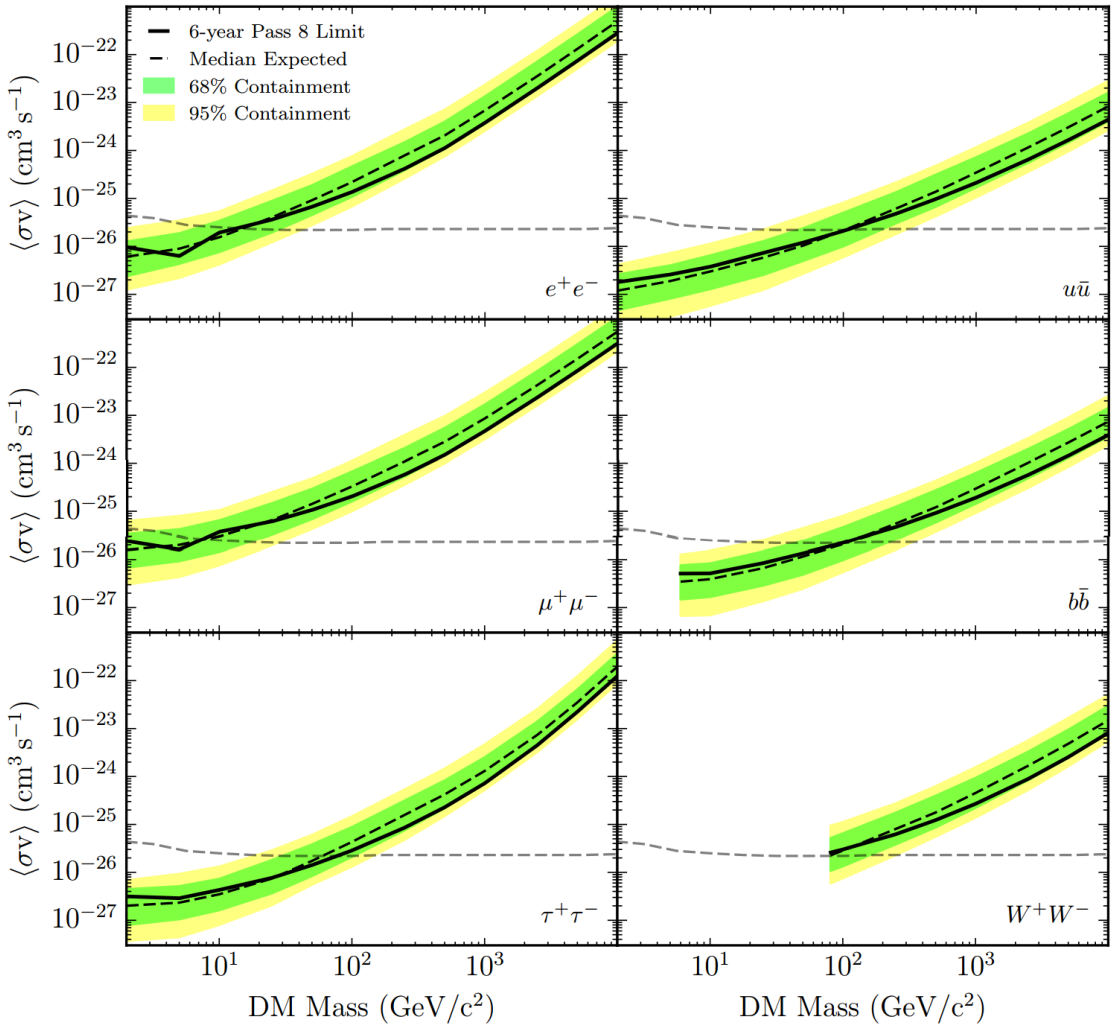


Figure 2.6: Fermi-LAT upper limits on the cosmological Majorana fermion DM annihilation cross-sections $\langle\sigma v\rangle$ as a function of DM mass for various channels [33]. Each plot shows the cross section upper limit on $\chi\bar{\chi} \to f\bar{f}$ assuming a 100% branching fraction into $f\bar{f}$ for various species of $f\bar{f}$: e^+e^-, $u\bar{u}$, $\mu^+\mu^-$, $b\bar{b}$, $\tau^+\tau^-$ and W^+W^-. The dashed gray curve corresponds to the thermal relic cross section from Reference [37] needed to explain the relic abundance of dark matter. When the upper limit on $\langle\sigma v\rangle$ is smaller than the thermal relic cross section the model may be considered excluded. However, different assumptions for the DM particle species and branching fractions change the limits on $\langle\sigma v\rangle$ and the predicted thermal relic cross section.

2.4.1 Simplified Models

A theory of dark matter is needed to interpret production cross section limits from collider searches and relate these bounds to constraints from direct direct and indirect detection experiments. Several theories offer a complete theoretical framework that could account both the Standard Model and dark matter.

However, the preferred theoretical treatment remains agnostic to any physics beyond the dark matter particle and its interaction with the Standard Model [38].

An effective field theory [40] would comprise the most general treatment of dark matter and Standard Model interactions, without relying on any assumptions on mediator particles and their masses. However, the EFT approach breaks down if the momentum transfer of the interaction approaches the scale of new physics. The large momentum transfer inherent in LHC WIMP pair production threatens EFT validity [41].

Unlike EFTs, simplified models are able to describe correctly the full kinematics of dark production at the LHC at the cost of adding an additional particle which mediates the interaction [38]. This mediator particle connects the Standard Model quarks to dark matter WIMPs through an s–channel or t–channel exchange. The model depends on four parameters: mass of the dark matter particles m_χ, mass of the mediator m_{med}, the flavor-universal coupling between the mediator and the quarks g_q, and the coupling between the mediator and dark matter particles g_χ. The mediator is assumed to have minimal width, only decaying to dark matter or quarks.

As direct detection experiments provide powerful constraints on spin independent DM-matter interactions, only models with a pseudoscalar mediator ϕ or axial vector mediator A are considered in this thesis. The Lagrangian for the pseudoscalar mediator model is:

$$\mathcal{L}_\phi = -ig_\chi \phi \bar{\chi}\gamma^5\chi - ig_q\frac{\phi}{\sqrt{2}}\sum_{q=u,d,s,c,b,t} y_q \bar{q}\gamma^5 q \tag{2.3}$$

where $y_q = \sqrt{2}m_q/v$ are the quark Yukawa couplings with the Higgs vacuum expectation value $v = 246$ GeV. The mediator to dark matter coupling is parameterized by g_χ rather than by a Yukawa coupling $y_\chi = \sqrt{2}m_\chi/v$ to remain agnostic to the mass generation mechanism for dark matter. Assuming that all particles are kinematically accessible, the mediator width is:

$$\Gamma_\phi = \frac{g_\chi^2 m_\phi}{8\pi}\left(1-4\frac{m_\chi^2}{m_\phi^2}\right)^{1/2} + \sum_q \frac{3g_q^2 y_q^2 m_\phi}{16\pi}\left(1-4\frac{m_q^2}{m_\phi^2}\right)^{1/2} + \frac{\alpha_s^2 g_q^2 m_\phi^3}{32\pi^3 v^2}\left|f_\phi\left(4\frac{m_t^2}{m_\phi^2}\right)\right|^2 \tag{2.4}$$

where

$$f_\phi(x) = x \arctan^2\left(\frac{1}{\sqrt{1-x}}\right) \tag{2.5}$$

The first term in Equation 2.4 corresponds to the decay to dark matter, the second to quarks, and the third to gluons. The Lagrangian for the axial vector mediator model is:

$$\mathcal{L}_A = -g_\chi A_\mu \bar{\chi}\gamma^\mu\gamma^5\chi - g_q \sum_{q=u,d,s,c,b,t} A_\mu \bar{q}\gamma^\mu\gamma^5 q \tag{2.6}$$

and the corresponding width is:

$$\Gamma_A = \frac{g_\chi^2 m_a}{12\pi}\left(1-4\frac{m_\chi^2}{m_a^2}\right)^{3/2} + \frac{g_\chi^2 m_a}{4\pi}\left(1-4\frac{m_q^2}{m_a^2}\right)^{3/2} \tag{2.7}$$

assuming that the particles are kinematically accessible. The first term corresponds to the decay to dark matter and the second to the decay to quarks.

Couplings are subject to perturbativity bounds [42]:

$$g_q, g_\chi < 4\pi \tag{2.8}$$

but otherwise the specific choice of couplings for a given model is a matter of preference, although couplings cannot be reduced arbitrarily without coming into tension with thermal relic density motivations. Models with other couplings are examined, but the main results of this thesis are presented for couplings:

$$g_q = 0.25 \qquad g_\chi = 1 \tag{2.9}$$

This choice allows for a consistent comparison across collider results within a given simplified model, ensuring that the mediator has $\Gamma_{\text{med}}/m_{\text{med}} \simeq 10\%$ and that the theory is far from the strong coupling regime. Additionally, the choice of $g_\chi > g_q$ and $g_q = 0.25$ for spin-1 mediators is motivated by the desire to circumvent dijet constraints from the LHC and earlier hadron colliders, although as shown in Figures 8.6 and 8.7 this is best achieved with $g_q = 0.1$ and $g_\chi = 1.5$.

2.4.2 Direct Detection

Direct detection experiments set limits on the DM-nucleon scattering cross section for both spin–independent and spin-dependent interactions. As pseudoscalar and axial-vector bosons mediate the latter, only the SD case is considered below. Additionally, unlike other interactions the pseudoscalar mediator case has additional velocity-suppression in the non-relativistic limit [39]. As a consequence, direct detection experiments are not sensitive to pseudoscalar interactions. Only the axial-vector mediator limits are compared to direct detection experiments in this thesis.

The spin-dependent scattering cross section for an axial vector mediator is:

$$\sigma_{\mathrm{SD}} = \frac{3f^2(g_q)g_\chi^2\mu_{n\chi}^2}{\pi m_a^2} \tag{2.10}$$

where f is the nucleon form factor and $\mu_{c\chi}$ is the DM-nucleon reduced mass. If the coupling g_q is equal for all quarks then $f(g_q) = 0.32g_q$, and the scattering cross section may be written as:

$$\sigma_{\mathrm{SD}} \simeq 2.4 \times 10^{-42}\mathrm{cm}^2 \cdot \left(\frac{g_q g_\chi}{0.25}\right)^2 \left(\frac{1\mathrm{TeV}}{m_a}\right)^4 \left(\frac{\mu_{n\chi}}{1\mathrm{GeV}}\right)^2 \tag{2.11}$$

This relation is used to translate limits on the dark matter production cross section to limits on the DM-nucleon scattering cross section, as shown in Figure 8.5.

2.4.3 Indirect Detection

Indirect detection experiments set limits on the cross section for dark matter to annihilate to a single particle-anti-particle final state. These limits assume that dark matter is a Majorana fermion, which can be compared to limits on Dirac fermion dark matter though a simple rescaling by a factor of two [39]. The axial-vector mediator annihilation process $\chi\bar{\chi} \to A \to q\bar{q}$ is helicity suppressed [38]. As such, only interpretation for the pseudoscalar mediator is considered. The annihilation into a $q\bar{q}$ final state for the

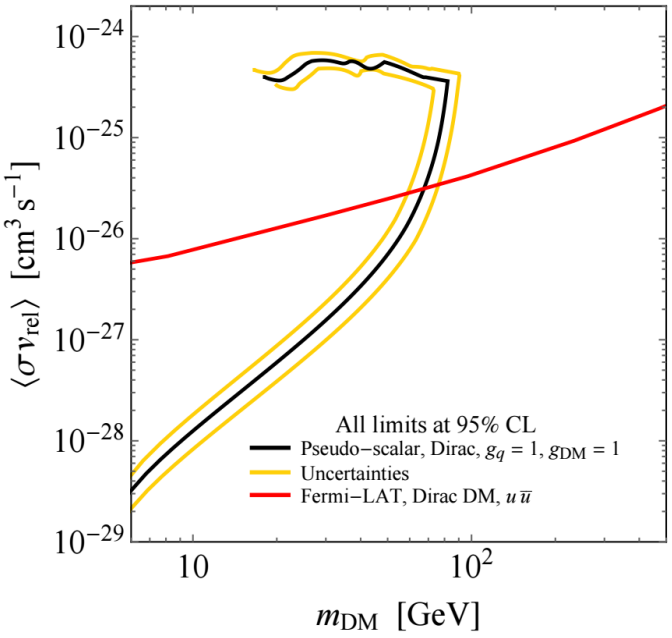


Figure 2.7: An example comparison of an LHC result to the Fermi-LAT upper limit on $\chi\bar{\chi} \to u\bar{u}$ [39]. The LHC limit is intended for illustration only and is not based on real data. Models corresponding to the phase space to the left of the LHC contour and above the Fermi-LAT contour are considered excluded. LHC results are expected to have superior sensitivity at low values of dark matter mass.

pseudoscalar mediator model is [39]:

$$\langle \sigma v_{\rm rel} \rangle_q = \frac{3m_q^2}{2\pi v^2} \frac{g_q^2 g_\chi^2 m_\chi^2}{(M_\phi^2 - 4m_\chi^2)^2 + M_\phi^2 \Gamma_\phi^2} \sqrt{1 - \frac{m_q^2}{m_\chi^2}} \tag{2.12}$$

In principle this expression can be used to compare LHC limits to constraints from indirect detection such as Fermi-LAT, but the 3.2 fb^{-1} ATLAS results lack sensitivity to the pseudoscalar mediator models. A qualitative comparison using a hypothetical LHC limit is shown in Figure 2.7. LHC results are expected to have superior sensitivity at low values of dark matter mass.

2.5 Relic Density Calculation

The relic density measured by the Planck experiment provides an additional constraint to any dark matter model. The relic density of thermal WIMP dark matter strongly depends on the strength of the coupling between dark matter and Standard Model particles. If the coupling is large, dark matter will readily decay

into matter and the relic abundance will be smaller. If the coupling is small, dark matter will freeze out when the universe is smaller and the corresponding relic density will be higher. The calculation of the dark matter relic abundance for the simplified models relies on the following assumptions:

- Dark matter only couples to the Standard Model via the mediator.
- No additional undiscovered particles couple to the mediator.
- No additional undiscovered particles couple to dark matter.

A numerical calculation of the relic density is performed using the program MadDM [43], which considers all tree-level $2 \to 2$ interaction modes between DM and SM particles. The processes are thermalized and the resulting relic density is computed.

Figure 2.8 shows the dark matter relic density in the $m_{\mathrm{med}} - m_{\mathrm{DM}}$ plane for the benchmark scalar, pseudo-scalar, vector, and axial vector mediator simplified models [38]. Solid contours indicate regions where the calculated relic density is consistent with the observed value. Regions where the relic density is either higher or lower than the observed value are referred to as over- and under-abundance regions, respectively. In all coupling scenarios, over-abundance of dark matter is observed for $m_\chi < M_{\mathrm{med}}$. The size of this region is generally anti-correlated with the coupling strength g_q. For larger values of g_q, dark matter can more easily annihilate into quarks, reducing the expected relic density and decreasing the size of over-abundance regions. In the axial vector mediator model the generic overabundance region extends to higher m_χ than in the vector mediator case. The region of under-abundance along $m_\chi = M_{\mathrm{med}}/2$ is generated by resonant DM annihilation into the mediator particle. The calculated relic density for models with scalar and pseudo-scalar couplings is additionally shaped by top–quark processes.

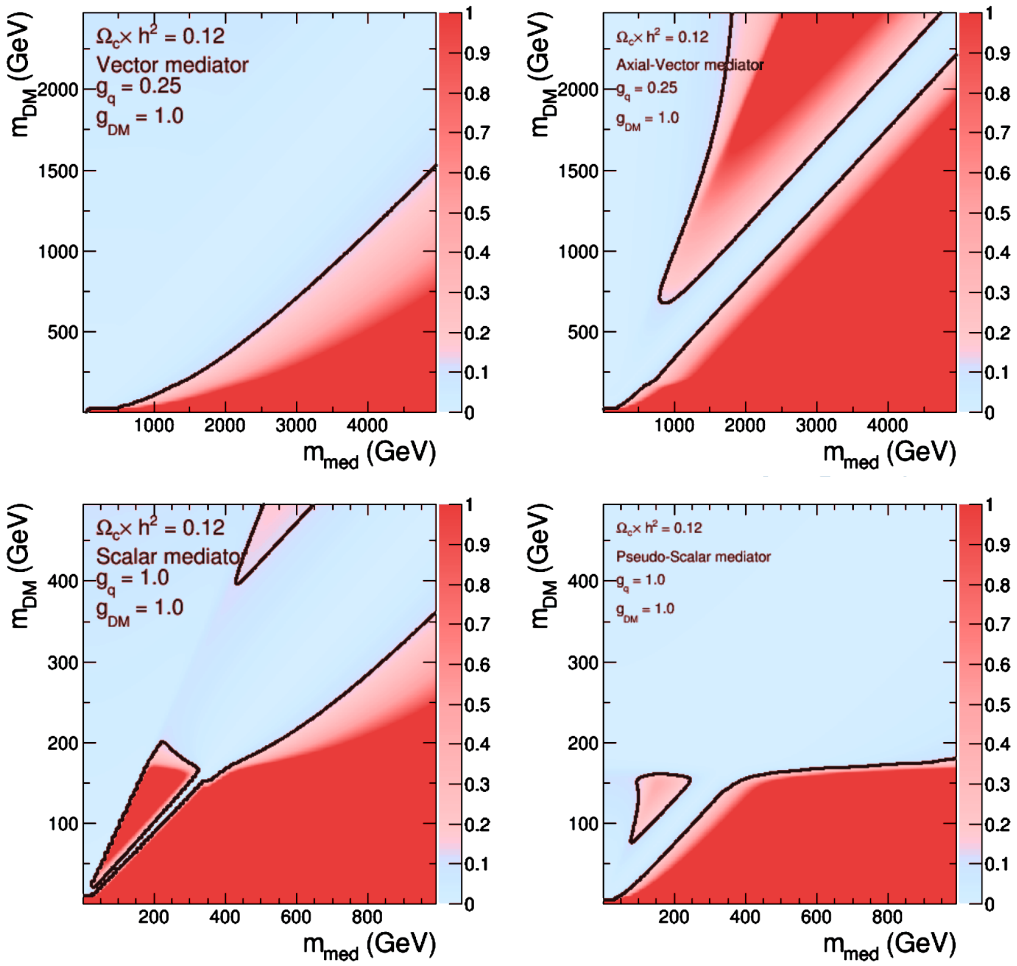


Figure 2.8: The predicted relic density Ωh^2 in the $(M_{\text{rediator}}, m_\chi)$ plane for a vector (top left) and axial-vector mediator (top right), both with couplings $g_q = 0.25$ and $g_\chi = 1.0$, and for a scalar (bottom left) and pseudo-scalar mediator (bottom right) with couplings $g_q = g_\chi = 1.0$ [44]. The contour lines correspond to the region where the relic density is consistent with the value $\Omega h^2 = 0.1185 \pm 0.0020$, as measured by the Planck collaboration. Red regions correspond to an *over-abundance* of dark matter, while pale blue regions indicate an *under-abundance*. In all coupling scenarios, over-abundance of dark matter is observed for $m_\chi < M_{\text{med}}$. The size of this region is generally anti-correlated with the coupling strength g_q. For larger values of g_q, dark matter can more easily annihilate into quarks, reducing the expected relic density and decreasing the size of over-abundance regions. In the axial vector mediator model the generic overabundance region extends to higher m_χ than in the vector mediator case. The region of under-abundance along $m_\chi = M_{\text{med}}/2$ is generated by resonant DM annihilation into the mediator particle. The calculated relic density for models with scalar and pseudo-scalar couplings is additionally shaped by top–quark processes.

Part II

Experimental Background

3

The Large Hadron Collider

The Large Hadron Collider (LHC) is the world's largest and most powerful particle collider [25]. It consists of 27 kilometers of over 8000 superconducting magnets and accelerating structures designed to achieve a proton-proton collision center of mass energy of $\sqrt{s} = 14\,\text{TeV}$ at an instantaneous luminosity of $1 \times 10^{34}\,\text{cm}^{-2}\,\text{s}^{-1}$. The unprecedented center-of-mass energy and luminosity allows for the discovery of the Higgs Boson, precision measurements of the Standard Model, and the ability to search for and constrain the production of BSM particles such as dark matter candidates.

3.1 Accelerator Design

Protons accelerated in the LHC originate from a bottle of hydrogen gas. An electric field strips the electrons from the hydrogen to create protons, which are then passed to a series of accelerators: Linac 2 accelerates the protons to 50 MeV, the Proton Synchrotron Booster (PSB) pushes the protons to 1.4 GeV, the Proton Synchrotron (PS) brings the beam energy up to 25 GeV, and the Super Proton Synchrotron (SPS)

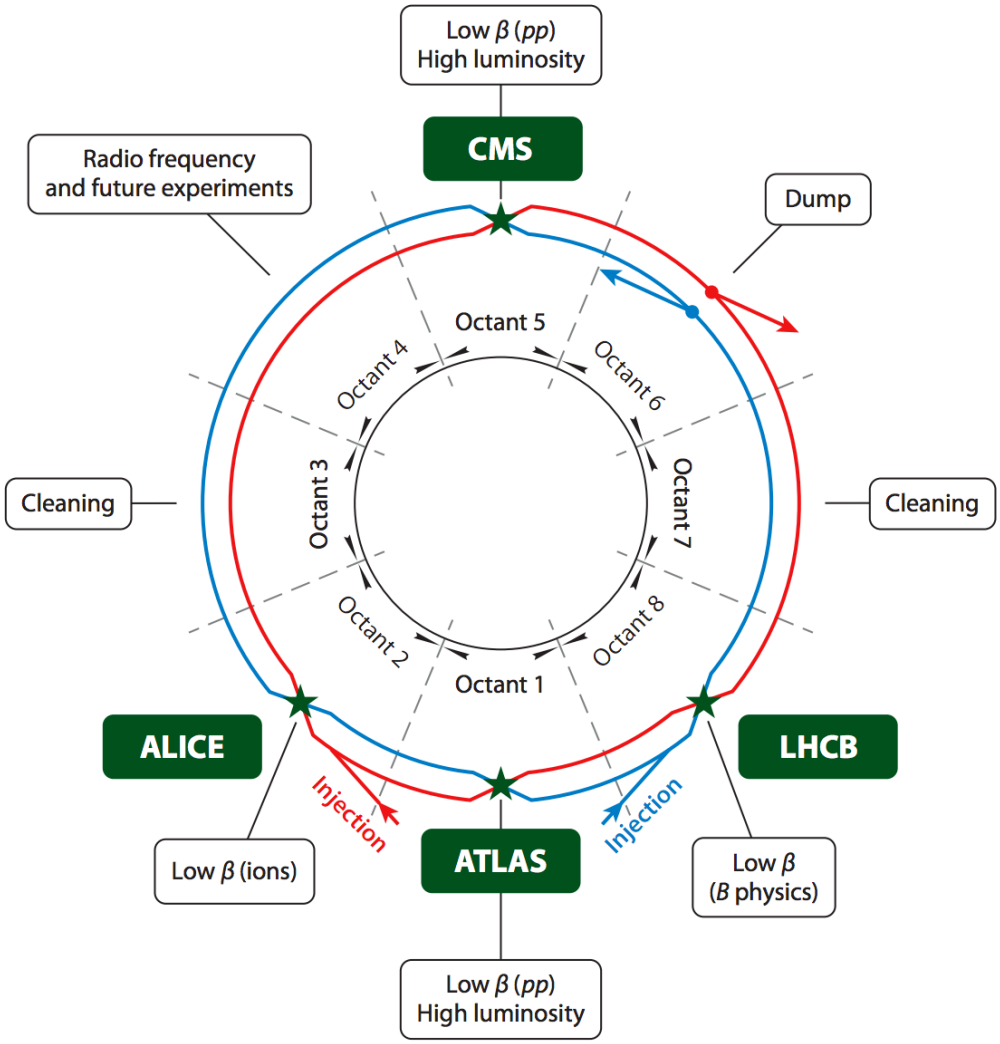


Figure 3.1: A diagram of the LHC ring [45] with the four main experiments. ATLAS and CMS are general purpose experiments, while ALICE analyzes heavy ion collisions and LHC*b* studies B physics. Betatron beam cleaning is located in octant 7 and momentum cleaning in octant 3 [46]. β is roughly the width of the beam squared divided by the emittance, and determines the instantaneous luminosity of any collision point as described in Section 3.2.

accelerates the protons to 450 GeV. Finally, the protons are transferred to the LHC.

A single magnetic dipole field cannot be used to collide two counter-rotating proton beams as in particle–anti–particle colliders. The LHC uses a twin-bore [47] design in which both proton rings are contained within one cryostat but subject to separate magnetic fields and vacuum systems, with common sections only at the insertion regions where the experimental detectors are located [25]. The beams are bent around the ring with a 8.33 T magnetic field produced by superconducting dipole magnets, which are cooled to a

temperature of 1.9 K with superfluid helium.

Within the ring protons are accelerated with RF cavity systems running at 400 MHz. After accelerating the proton beams from the injection energy of 450 GeV to 7 TeV, the RF acceleration compensates for the 7 keV of energy lost per beam per revolution due to synchrotron radiation. The LHC receives protons in bunches of approximately 10^{11} particles, which accelerated around the ring in RF buckets. Each collision event can result in multiple proton–proton interactions, of which only one might occasionally manifest interesting physics. The superfluous collisions are known as pileup.

The two beams collide at four experiments around the ring: ATLAS (A Toroidal LHC ApparatuS), CMS (the Compact Muon Solenoid), ALICE (A Large Ion Collider Experiment), and LHC*b* [3, 48–50]. Figure 3.1 shows a schematic of the LHC ring and experiments.

3.2 Instantaneous luminosity

The rate of physics events for a specified physics process R_{events} expected from the accelerator is dependent on the instantaneous luminosity L of the machine and the cross section σ of the physics process: $R_{\text{events}} = L\sigma$. The instantaneous luminosity of the LHC is determined by numerous factors related to beam parameters and conditions [45]:

$$L = \frac{N_b^2 n_b f_{\text{rev}} \gamma_r}{4\pi\epsilon_n \beta^*} F \tag{3.1}$$

N_b is the number of protons per bunch and n_b is the number of bunches per beam. f_{rev} is the revolution frequency of the accelerator, and is fixed by the size of the LHC tunnel and the velocity of the protons. γ is the relativistic Lorentz factor. ϵ_n is the normalized transverse beam emittance, a measurement of the average spread of the particles in position and momentum space. β^* is the β function at the interaction point, which relates the emittance to the Gaussian width of the beam with $\sigma_{\text{beam}} = \sqrt{\epsilon \cdot \beta}$. Finally, F is a geometric factor related to the crossing angle of the beams at the interaction point. If the crossing angle θ_c is small, then $F \approx 1/\sqrt{1 + (\frac{\theta_c \sigma_z}{2\sigma_{\text{beam}}})^2}$ where σ_z is the RMS length of each bunch.

The instantaneous luminosity can be maximized by tuning the parameters of equation 3.1. Increasing the number of bunches in the beam or the number of protons per bunch raises the luminosity. However,

Parameter [unit]	Nominal design value	Operating value in 2015
Beam Energy	7 TeV	6.5 TeV
Peak instantaneous luminosity	10^{34}cm^2 s^{-1}	5×10^{33}cm^2 s^{-1}
Bunch spacing	25 ns	25 ns
Intensity per bunch	1.15×10^{11} p	1.15×10^{11} p
Number of filled bunches	2808	1825
f_{rev}	11245 kHz	–
β^*	55 cm	80–40 cm
σ^*	16.7 μ m	13 μm
θ_c	285 μ rad	–
σ_z	7.55 cm	–
F	0.84	–

Table 3.1: LHC nominal [25] and operational parameters [51]. Unchanged values are omitted.

this number cannot be increased arbitrarily as too many particles in the beam can lead to damage to the detectors or accelerator if control of the beam is lost. A smaller crossing angle will result in higher luminosity, but can also create collisions outside of the interaction point [46], which is not ideal for reconstructing the results of the collision or avoiding damage to expensive detector systems. The main parameter which can be controlled by the LHC operation is β^*, where lower β^* corresponds to higher luminosity. The target peak luminosity for both the ATLAS and CMS experiments is $L = 10^{34}$ cm^{2}s^1 [25]. The main parameters of the LHC beam are displayed in Table 3.1.

3.3 Beam Cleaning and Beam Halo

The proton beams are not perfect. Off–momentum and off–orbit particles circulating in the LHC ring are known as "beam halo". These particles are largely absorbed by the collimation system to avoid damaging accelerator and detector components. At special beam cleaning insertions (shown in Figure 3.1) primary collimators intercept particles that have drifted from the beam core. A secondary collimator is designed to stop any particles that that scatter from the primary collimator and remain in the beam, known as secondary halo. The combined efficiency of this system is greater than 99.9% [1], but some particles persist in the beam as tertiary halo. The cleaning process is shown in Figure 3.2. A small fraction of the beam

[1] Local beam cleaning inefficiency is the ratio of losses in a segment of beam to distance-normalized losses in the collimator system: $\epsilon = N_{\text{lost}}^{\Delta s}/(\Delta s \cdot N_{\text{col}})$ where $\Delta s = 10$ cm [52].

halo intersects with the collimators close to interaction points, and the subsequent particle showers will interact with detector systems. Additionally, protons in the beam can scatter off of residual particles in the vacuum system, creating another source of non–collision interactions with detector systems [46].

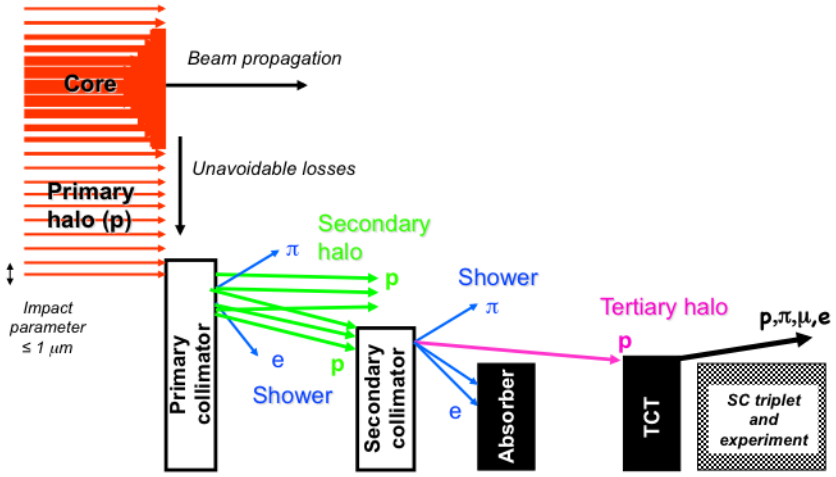


Figure 3.2: Scattering and absorption of the beam halo by the LHC collimation system [46].

4

The ATLAS Detector

A Toroidal LHC Apparatus (ATLAS) is a particle detector built to study proton-proton collisions at energies up to $\sqrt{s} = 14$ TeV at the LHC [3]. ATLAS is a multi-purpose detector capable of measuring of Standard Model physics processes with extreme precision and searching for evidence of new physics at hitherto unexplored energies. Particles created in proton–proton collisions can pass through four detector systems:

- The inner detector (ID), which measures the momentum charged particles
- The electromagnetic (EM) calorimeter, which measures the energy of electrons and photons and contributes to the energy measurement of hadronic showers
- The hadronic calorimeter, which measures the energy of hadronic showers
- The muon spectrometer, which measures the momentum of muons

This chapter reviews the geometry and materials of these detector systems.

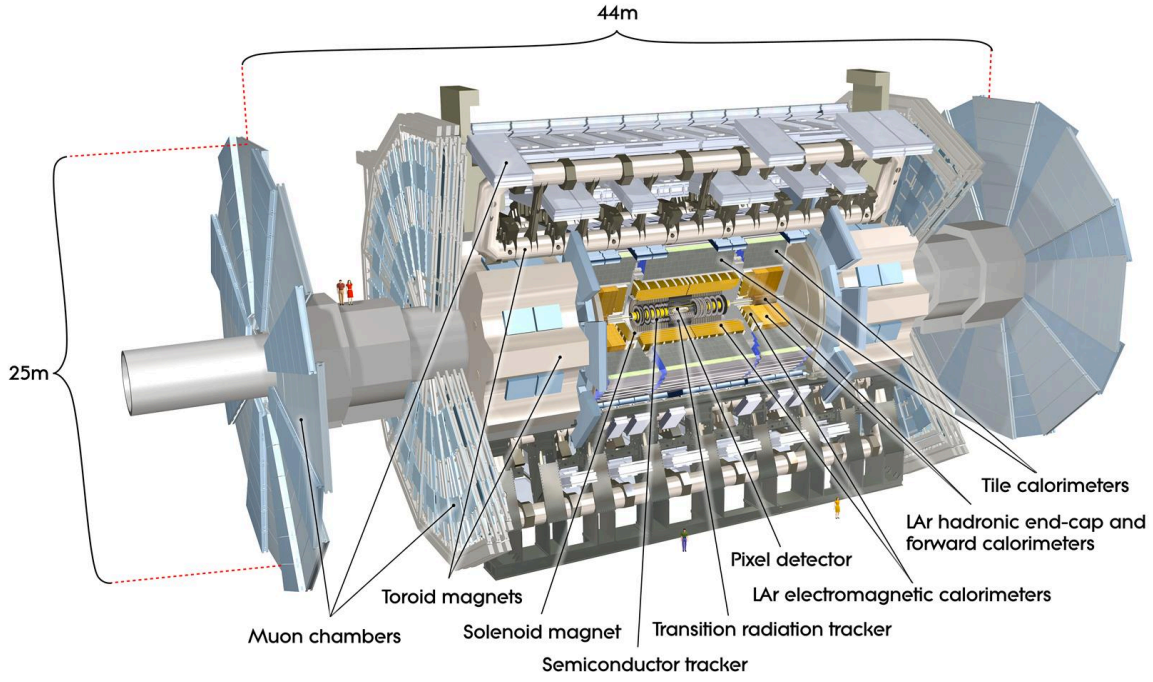


Figure 4.1: A full diagram of the ATLAS detector [3].

ATLAS uses a right-handed coordinate system with origin at the proton–proton interaction point in the center of the detector, z-axis along the beam pipe, and x–y plane transverse to the beam direction, as shown in Figure 4.2. Cylindrical coordinates (r, ϕ) are used in the transverse plane, ϕ being the azimuthal angle around the beam pipe. The pseudorapidity η is defined in terms of the polar angle θ as $\eta = -\ln\tan(\theta/2)$ [1]. Particles traveling perpendicular to the beam pipe will have $\eta = 0$ and particles traveling parallel to the beam pipe will have $\eta = \pm\infty$. The ATLAS detector has nearly 4π coverage in solid angle around the interaction point with layers of tracking detectors up to $|\eta| = 2.5$, calorimeters up to $|\eta| = 4.9$, and muon chambers up to $|\eta| = 2.7$.

Figure 4.1 shows an overview of the detector. Cylindrical "barrel" elements of the detector surround the beam line cylindrically in the central low-η region. In the forward high-η region "endcap" elements are arranged as disks perpendicular to the beam line.

[1] Pseudorapidity is the massless approximation of rapidity, the angle used to parameterize boosts in special relativity.

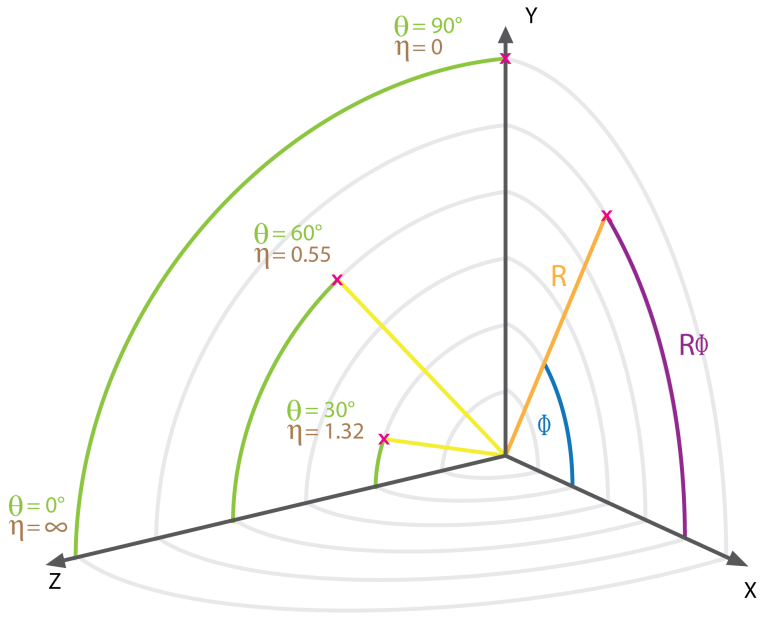


Figure 4.2: The ATLAS coordinate system. The z direction corresponds to the beam axis, while x and y define the transverse plane. θ is the angle relative to the beam axis and ϕ is the azimuthal angle. η, the pseudorapidity, approaches infinity at small angles relative to the beam axis.

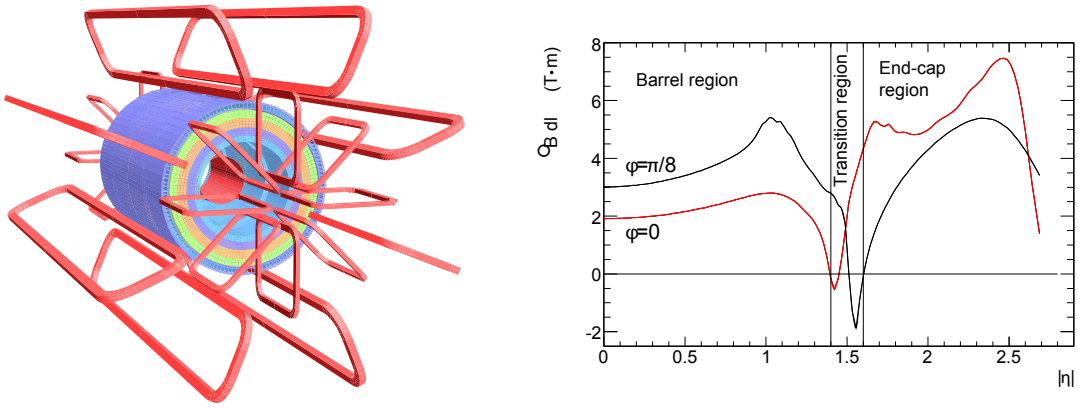
4.1 Magnetic Field

Magnetic fields can be used to measure the momentum of a charged particle via the relationship between the Lorenz force and the particle speed $\boldsymbol{F} = q\boldsymbol{v} \times \boldsymbol{B}$. ATLAS exploits this to measure the particle momentum in the inner detector and the muon spectrometer with two independent magnet systems.

The inner detector is surrounded by a solenoid providing a 2 T axial magnetic field which bends particle tracks in the transverse plane to allow for particle momentum measurement. The magnetic field in the muon spectrometer is provided by a system of three large air-core toroid magnets. These magnets provide 1.5 to 5.5 $\mathrm{T \cdot m}$ of bending power at $0 < |\eta| < 1.4$ and approximately 1 to 7.5 $\mathrm{T \cdot m}$ in the endcap region of $1.6 < |\eta| < 2.7$. Figure 4.3 shows the predicted field integral as a function of $|\eta|$ [3].

A simulation of the magnetic field is necessary to study particle reconstruction and generate the expected detector signatures of various physics processes in simulation. The magnetic field is modeled using the geometry and electric current in the toroid and solenoid systems in conjunction with perturbations from the calorimeter iron. The precise location and deformation of each toroid under the field is determined by

fitting the simulated magnetic field to magnetic field readings from sensors in barrel and endcaps.



(a) (b)

Figure 4.3: (Left) Geometry of magnet windings and tile calorimeter steel, showing the eight barrel toroid coils interleaved with the endcap coils [3]. (Right)Predicted field integral as a function of $|\eta|$ for the ATLAS magnet system [3].

4.2 Inner detector

The inner detector is the closest detector system to the beamline, and is the first system traversed by particles created in a proton–proton collision. The inner detector provides precise and efficient tracking for charged particles using pixel and silicon microstrip (SCT) trackers in conjunction with the straw tubes of the Transition Radiation Tracker (TRT). Figure 4.4 shows the layout of each of these components. Specific parameter values are given in Table 4.1.

Proton–proton collisions in the ATLAS detector are not singular. Up to twenty or more proton–proton collisions can occur in each event, as shown in Figure 4.5. The inner detector has enough fidelity to assign particles and jets to different primary vertices and correct the measurement of missing transverse energy for contributions from low-energy particles. Information about track vertices is also used to distinguish and measure secondary vertices to identify tracks consistent with the decay of long-lived particles such as τ leptons, kaons, lambda baryons, and B-hadrons. Additionally, inner detector tracks are used to identify electrons and measure their position, identify photon conversions, and measure the momentum of muons in combination with the muon spectrometer.

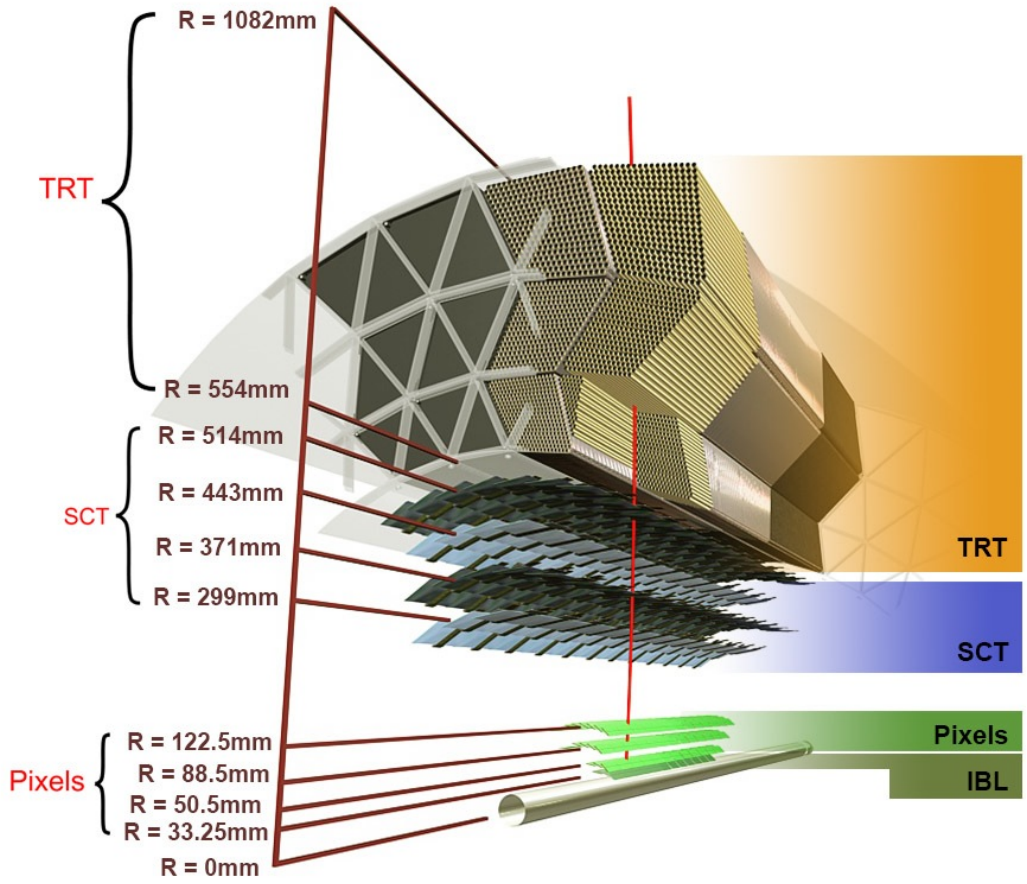


Figure 4.4: Layout of the ATLAS Inner Detector system [53]. A 10 GeV charged particle at $\eta = 0.3$ will successively traverse the beryllium beam-pipe, the four cylindrical silicon-pixel layers, the four cylindrical double layers of silicon-microstrip sensors, and approximately 36 axial straws modules in the barrel transition-radiation tracker [3].

4.2.1 Silicon Detectors

Parameter	Pixels	SCT	TRT
η coverage	2.5	2.5	2.0
Number of hits on track	4	8	36
Radius of innermost layer (cm)	5.0	30	56
Total number of channels	8×10^7	8×10^6	3.5×10^5
Cell size ($R\phi \times z/R$)	50μm $\times$ 400μm	80μm $\times$ 12cm	4mm $\times$ 70cm
Resolution in $R\phi$ (μm)	10	16	170
Resolution in Z/R (μm)	80	580	

Table 4.1: ATLAS inner detector parameters [3].

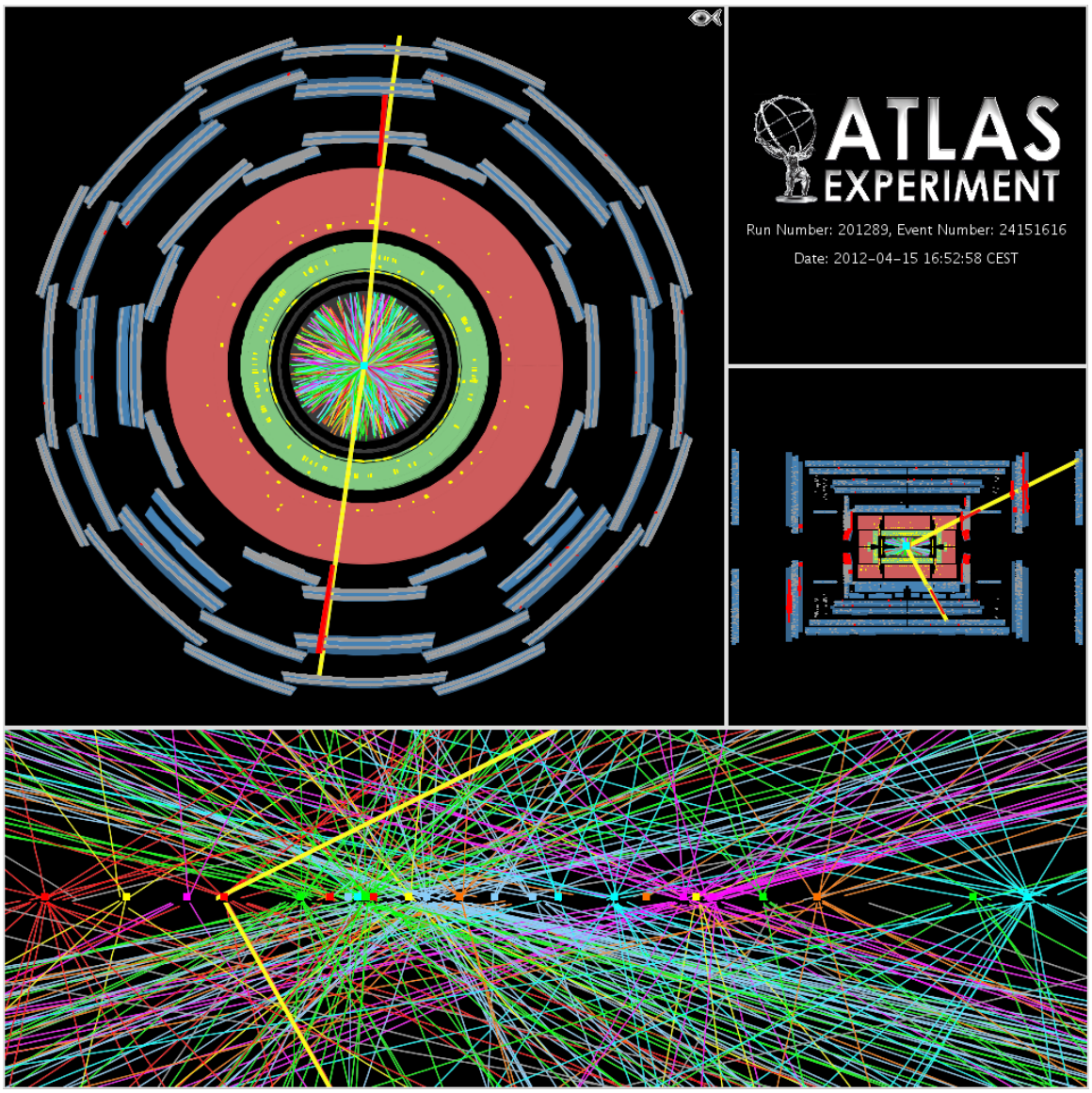


Figure 4.5: A candidate Z boson event in the dimuon decay with 25 reconstructed vertices [54]. The upper left image shows tracks and energy deposits in the transverse plane, the right-center image shows the same features in the R-z plane, and the bottom image is a magnified view of the interaction point. Muons created by the Z boson decay are highlighted in yellow. This event was recorded on April 15th 2012.

The innermost three to four layers of the inner detector are the pixel detectors, followed by four layers of SCT detectors. Both of these systems are silicon detectors. This type of detector consists of a bulk material that is made of a n-type Si semiconductor wafer. The passage of a charged particle creates electron-hole pairs that are separated by the electric field. These detectors allow for a huge resolution improvement over previous detectors such as spark, cloud, bubble, or wire chambers. However, the systems are much more

expensive, require complex cooling, and are more susceptible to radiation damage.

The pixel detectors are optimized for high resolution position measurements close to the beam line and consist of three layers in the endcap and four in the barrel. The high granularity of this system is crucial for precision tracking and vertex reconstruction. The intrinsic accuracies of the sensors are $10\ \mu\mathrm{m}$ in R-ϕ and $115\ \mu\mathrm{m}$ in z (or R for the endcap).

The semiconductor tracker (SCT) consists of 6.4 cm long sensors that are connected into strips with a strip width of $80\ \mu\mathrm{m}$ [3]. Each SCT layer has two semiconductor planes with strips placed at a 40 mrad angle to allow the measurement of the second coordinate. There are four layers of detector pair for a total of eight position measurements in $R\phi$ and four in z for a particle passing through the system. The intrinsic accuracies are $17\ \mu\mathrm{m}$ in R-ϕ and $580\ \mu\mathrm{m}$ in z (or R in the endcap).

Both the pixel and SCT detectors have readout times faster than the 25 ns LHC bunch interval, allowing for the differentiation of hits from different bunch crossings.

4.2.2 Transition radiation tracker

The transition radiation tracker (TRT) is the outermost layer of the inner detector. The TRT is a gaseous detector that consists of multiple straw tubes arranged parallel to the beam line in the barrel and radially in the endcap. The $4\ \mathrm{mm}$ diameter straw tubes are filled with a $70/27/3\%$ gas mixture of xenon, carbon dioxide, and oxygen to provide tracking of charged particles. Although the spatial resolution of $170\ \mu\mathrm{m}$ is less precise than the silicon detector systems, the longer lever arm allows TRT hits to contribute more to the track momentum measurement.

The TRT makes use of the transition radiation that is emitted when a charged particle passes through the boundary of two regions with different dielectric constants. This radiation creates ionization in the gas volume and the resulting cascade produces a signal that is proportional to the amount of energy lost in the transition radiation, which in turn is proportional to the Lorentz factor of the particle passing through the detector. The transition radiation measurement is primarily used for discrimination between electrons and pions or other charged hadrons.

4.3 Calorimeters

The calorimeter systems surround the inner detector. The ATLAS calorimeters measure the energy and position for of electrons, photons, mesons, and hadronic jets, and are used to calculate the missing transverse momentum in each event.

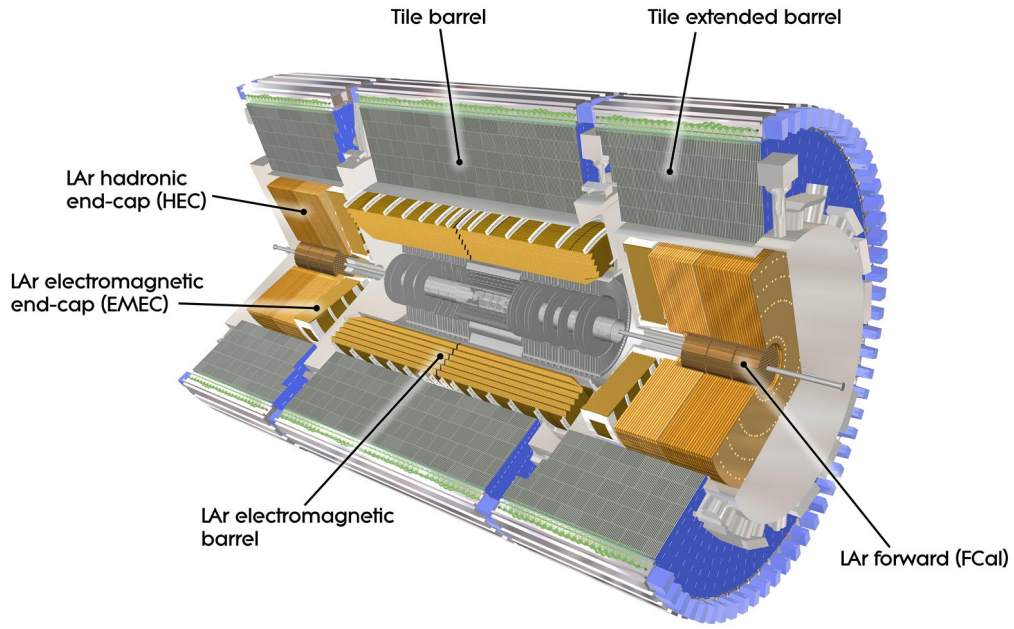


Figure 4.6: Layout of the ATLAS calorimeter system [3].

4.3.1 Electromagnetic Calorimeters

The ATLAS electromagnetic (EM calorimeter) calorimeter measures the energy of electrons and photons. When a high-energy photon or electron is incident on a thick absorber, photon pair production and electron bremsstrahlung will generate more electrons and photons with lower energy than the original particle. The number of particles in this electromagnetic shower is proportional to the energy of the original particle. The longitudinal intensity of the shower attenuates exponentially with distance [55]:

$$I(x) = I_0 e^{-x/X_0} \tag{4.1}$$

where I is the intensity, x is the distance traveled, and X_0 is the radiation length. The ATLAS EM calorimeter is designed to have more than 22 radiation lengths in the barrel and 24 in the endcap [3] to ensure that the shower is contained.

The EM calorimeter is a sampling calorimeter with alternating layers of lead and liquid argon (LAr) constructed using an accordion geometry. The calorimeter is segmented into four segments, three of which are shown in Figure 4.7. A thin LAr presampler layer corrects for energy lost before a particle reaches the calorimeter. Next, the preshower detector provides a precise measurement of particle η to enhance photon–pion discrimination and contribute to the measurement of shower direction. The third and thickest section is designed to absorb the majority of the shower energy, and the final section is used to correct the energy measurement for leakage outside the calorimeter. The EM calorimeter is divided into a barrel portion that extends to $|\eta| < 1.475$ and an endcap portion going from $1.375 < |\eta| < 3.2$. The region where these two units overlap is called the "transition region". The calorimeter is segmented by η and ϕ into "cells." Sequential longitudinal cells are called "towers."

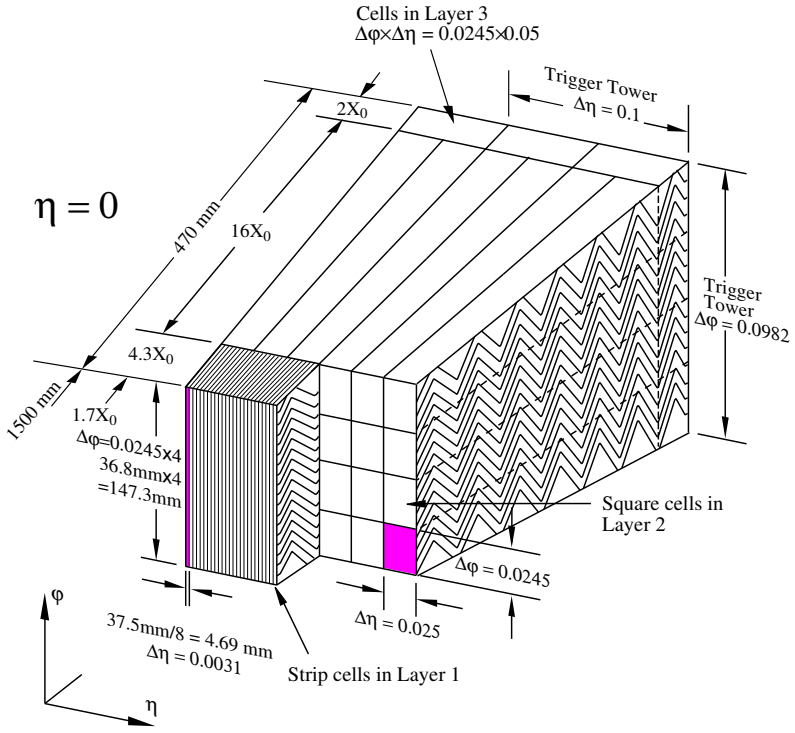


Figure 4.7: Diagram of the EM calorimeter in the barrel with visible calorimeter segmentation. [3].

4.3.2 Hadronic Calorimeters

The hadronic calorimeters are the second calorimeter system shown in Figure 4.6 and are designed to measure the energy of hadrons. Three different calorimeter technologies are used for the hadronic calorimeters:

1. The TileCal is a scintillating tile calorimeter that uses steel as the absorber and plastic scintillator tiles as the active material.

2. The hadronic endcap (HEC) uses LAr as the active material and copper as the absorber.

3. The forward calorimeter (FCal) is another LAr calorimeter that uses an inner module with copper absorbers and an outer module with tungsten.

The hadronic calorimetry in the range $|\eta| < 1.7$ is provided by a scintillator-tile calorimeter (Tile), which is separated into a central barrel and two smaller extended barrel cylinders, one on either side of the central barrel. The HEC covers $|\eta| > 1.5$ and the FCal extends the coverage to $|\eta| = 4.9$. Hadronic shower attenuation is measured with the hadronic interaction length λ. The hadronic calorimeter depth is approximately 9.7λ in the barrel and 10λ in the endcap. The outer calorimeter supports contribute an additional 1.3λ. Together this is sufficient to limit punch-through of showers to the muon system [3]. As in the EM calorimeter, the hadronic and forward calorimeters are segmented into four and three layers, respectively [56].

4.3.3 Liquid Argon Detectors

LAr calorimeters are used in both the EM and hadronic calorimeter systems. Although the detector systems have different geometries and absorber materials, the readout, calibration, and monitoring systems are designed to be uniform across the LAr systems [56].

When charged particles traverse the detector they ionize the liquid argon located in the gap between electrodes and absorbers. The ionization electrons are subject to an electric field which draws them towards the electrode, inducing a current proportional to the energy deposited in the liquid argon, shown

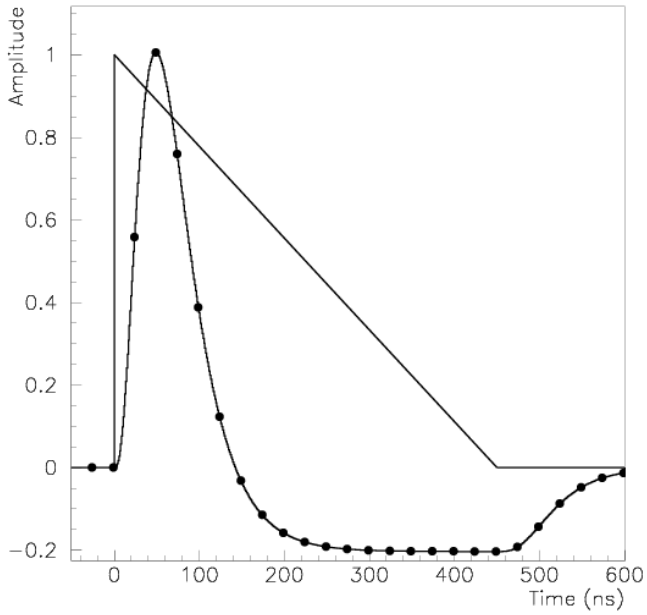


Figure 4.8: The LAr detector signal shape produced in the electromagnetic barrel (triangle) and after shaping (dotted line) [56].

in Figure 4.8. The calorimeter signal s_j is used to compute the cell signal amplitude A [57]:

$$A = \sum_{j=1}^{N_{\text{samples}}} a_j(s_j - p) \tag{4.2}$$

where p is the ADC pedestal and a_j are the Optimal Filtering Coefficients (OFC) computed per cell. The signal peak time t_{cell} is obtained with [57]:

$$t_{\text{cell}} = \frac{1}{A} \sum_{j=1}^{N_{\text{samples}}} b_j(s_j - p) \tag{4.3}$$

where b_j are time-OFCs. In a perfectly timed detector all signals produced in-time particles t_{cell} must be close to zero. The measured pulse in a given LAr calorimeter cell is compared to the expected pulse shape from simulation of the electronics response, a useful metric for discriminating between noise and real energy deposits The quadratic difference $Q_{\text{cell}}^{\text{LAr}}$ between the measured and expected pulse shapes is

defined as [57]:

$$Q_{\text{cell}}^{\text{LAr}} = \sum_{j=1}^{N_{\text{samples}}} (s_j - A \cdot (g_j - \tau g_j'))^2, \tag{4.4}$$

where A is the measured amplitude of the signal, τ is the measured time of the signal, s_j is the amplitude of each sample, j, in ADC counts, g_j is the normalized predicted ionization shape and $g_j^{'}$ is its derivative. The number of samples used to calculate this variable is $N_{\text{samples}} = 4$. $Q_{\text{cell}}^{\text{LAr}}$ is stored as a 16-bit unsigned integer and any values above 2^{16}-1 are set to the maximum value.

4.4 Muon spectrometer

The outermost detector system is the muon spectrometer, which measures the momentum and position of muons. Four different technologies are used in this system. Muon Drift Tubes (MDT) and Cathode Strip Chambers (CSC) are used for precision tracking. Resistive Plate Chambers (RPC) and Thin Gap Chambers (TGC) are used for for triggering (described in Section 4.5) in the barrel and endcap respectively. The entire muon system covers the range $0 < |\eta| < 2.7$ and is shown in Figure 4.9.

The MDTs are gaseous detectors filled with a $93/7$ % mixture of argon and CO_2 with trace amounts of water. A charged particle traversing the tube will ionize the gas, creating electrons that drift towards the wire at the center of the tube. The drift time of the electron cascade can be used to reconstruct the trajectory of the particle through the tube with an an average resolution of 80 μm per tube. The maximum drift time is approximately 700 ns. The tubes are oriented so that they give precision measurement in η and run along ϕ.

MDTs provide muon tracking up to $|\eta| < 2.7$, but in the innermost layer of the endcap only spans up to $|\eta| < 2.0$ [3] because individual MDT tubes can only sustain a hit rate of 150 Hz /cm^2, which is exceeded in this region.

Muon tracking in the innermost endcap region of $2.0 < |\eta| < 2.7$ is performed with the CSCs. This system is composed of multiwire proportional chambers filled with an an $80/20$% gas mixture of argon and CO_2 [3]. Charged particles passing through the chambers ionize the gas, and electrons are drawn to two sets of cathode readout strips one for precision measurement and the other perpendicular to the first

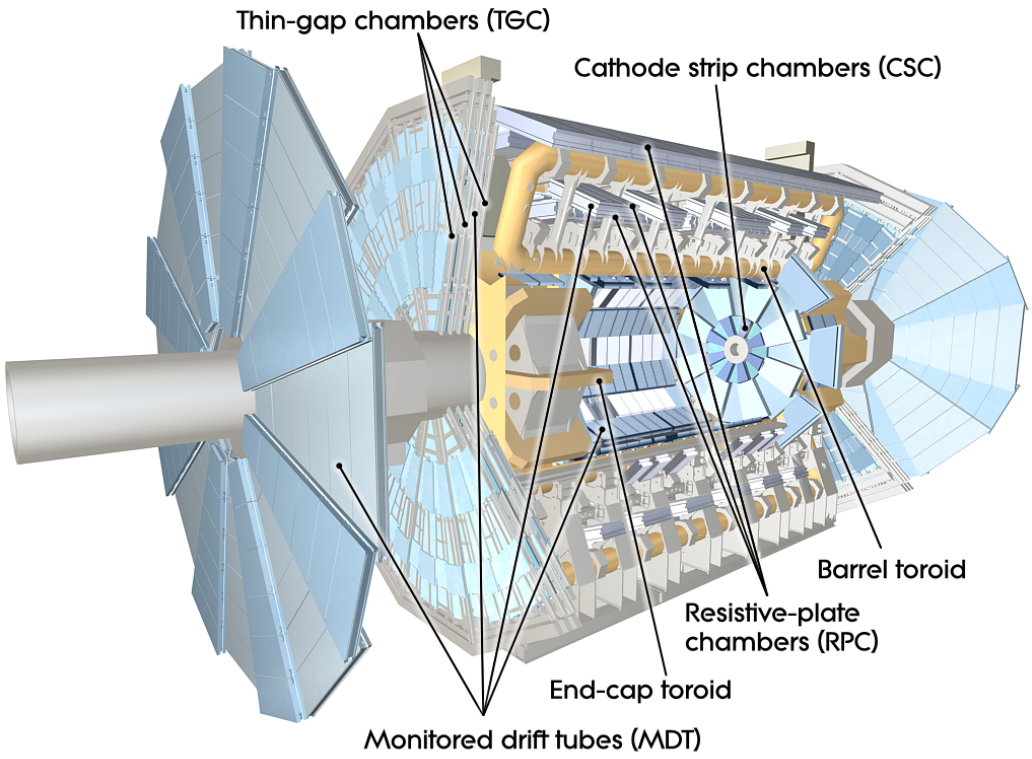


Figure 4.9: The ATLAS muon system [3].

to provide the transverse coordinate. The drift time is approximately 40 ns.

As the two precision tracking technologies have particle drift times greater than the 25 ns LHC bunch interval time, systems with more precise timing measurement are needed to assign muons to specific proton–proton collisions. In the barrel region ($|\eta| < 1.05$) RPCs are used for triggering. These gaseous electrode-plate detectors consist of two resistive plates separated by a distance of 2 mm and filled with a gas mixture used is a $94.7/5/0.3\%$ mixture of $C_2H_2F_4$, Iso-C_4H_10, and SF_6. The thin gas gap results in a quick signal response time of approximately 5 ns.

In the endcap, TGCs serve as the trigger chambers and provide azimuthal coordinate measurement. The TGCs are multiwire proportional chambers that contain a gas mixture of CO_2 and n-pentane. They have finer spatial resolution as compared to the RPCs to maintain the muon trigger transverse momentum threshold at high η and distinguish muon hits from signals arising from neutron and photon background in the endcap.

4.5 Trigger system

The LHC provides ATLAS with $\mathcal{O}(10^9)$ proton–proton collisions per second. However, limited bandwidth, processing power, and storage capacity limits the recorded events to $\mathcal{O}(10^2)$ per second. Fortunately only a subset of all proton–proton collisions are useful for physics measurements and searches. These interesting events are selected by the ATLAS trigger system. The trigger system saves events with signatures of physics objects such as muons, electrons, missing transverse momentum, or jets.

The trigger consists of two levels. A fast, hardware-based system called the Level-1 (L1) trigger consists of independent dedicated detector sub-components that can seed regions of interest (RoIs) for further analysis downstream. The RPCs and TGCs in the muon system and coarsely grained sections of calorimeter cells called towers are used to construct RoIs. Once regions of interest are seeded, a software-based system called the High Level Trigger (HLT) reconstructs objects and integrates information from different parts of the detector. At each stage, all information in an event passing a trigger is sent to the next level of processing.

The maximum trigger rate that the L1 trigger can handle is 75 kHz. In the HLT, the rate of events written to disk is approximately 400 Hz. Figure 4.10 shows the trigger rates for different L1 triggers in 2015 for ATLAS [58].

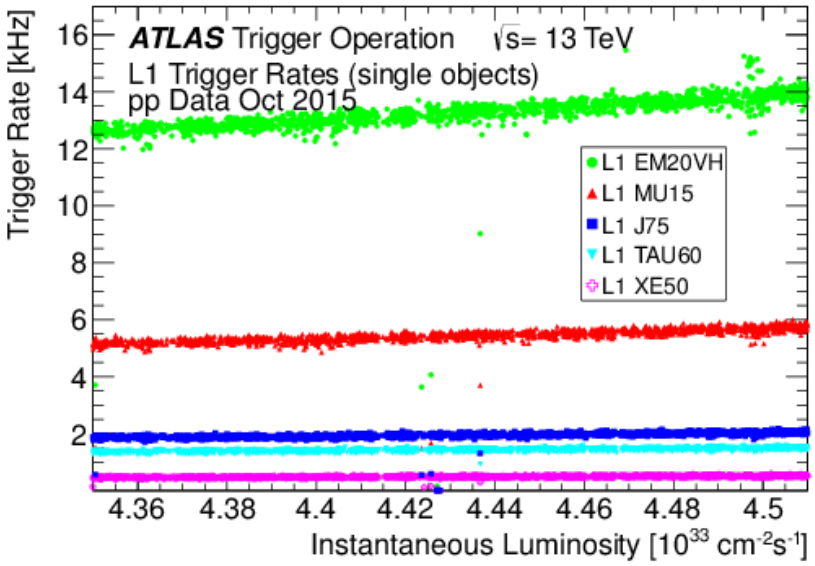


Figure 4.10: ATLAS trigger rates for Level-1 triggers as a function of instantaneous luminosity in 2015 operation. These are single object triggers for electromagnetic clusters (EM), muons (MU), jets (J), missing energy (XE), and τ leptons (TAU). The threshold of the trigger is given in the legend entry in GeV [58].

5

Object Reconstruction in ATLAS

The characteristic event topology of dark matter production in the ATLAS detector is a jet with large transverse momentum (p_T) recoiling against missing transverse momentum (E_T^{miss}). As such, a detailed understanding of how hadronic objects interact with the detector is needed to constrain background arising from non–collision processes. Additionally, Standard Model background processes are studied in a similar event topology with additional electrons or muons. The following chapter covers the reconstruction of jets, leptons, and missing energy in the ATLAS Detector. An illustration of various particles interacting with the ATLAS Detector is shown in Figure 5.1.

5.1 Inner Detector Tracks

Any long-lived charged particle produced in a proton–proton collision will interact with the inner detector and create hits in the different systems described in Section 4.2. These tracks are used to identify electrons and muons traversing the inner detector and are used to characterize the charged particle content of jets.

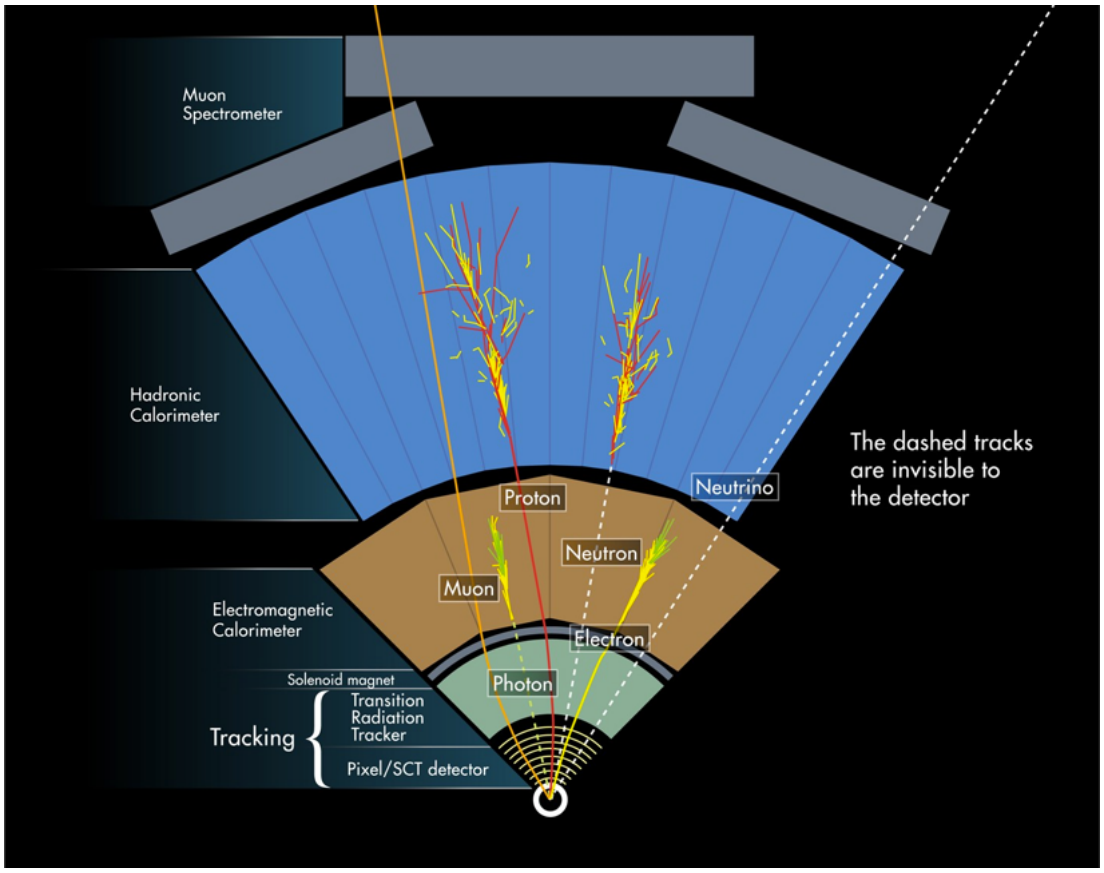


Figure 5.1: Illustration of particle interactions in ATLAS [59]. Charged particles leave tracks in the inner detector, photons and electrons leave energy deposits in the EM calorimeter, hadrons leave energy deposits in the hadronic calorimeter, and muons will pass through all systems and leave tracks in the muon spectrometer.

The inside-out algorithm is used to identify tracks created by particles originating directly from the proton–proton collision or from the decay of a particle with lifetime shorter than 3×10^{-11}s [60]. First, three dimensional space points are constructed from hits in the Pixel and SCT detectors. Triples of points are used to construct track seeds, which are then extended by adding additional points using a combinatorial Kalman filter [60]. After ambiguities in the silicon detector track candidates are resolved, the tracks are extended to include the TRT hits. The efficiency of track extension at different stages of the algorithm is shown in Figure 5.2.

Tracks are reconstructed within the full acceptance of the ID $|\eta| < 2.5$ from individual hits of charged particles in the ID sub-detectors. Tracks are required to have transverse momentum of at least 400 MeV, in addition satisfying the following quality criteria [61]:

1. Number of silicon hits ≥ 7

2. Number of hits shared with other tracks ≤ 1

3. Number of silicon holes[1] ≤ 2

4. Number of pixel holes ≤ 1

Reconstructed tracks are used to identify primary vertices with an iterative vertex finding algorithm [62]. First, a seed vertex is taken at global maximum in the distribution of track z coordinates at the closest approach to the beamspot. Then, an adaptive vertex fitting algorithm is used to assign tracks to the seed vertex. Any tracks incompatible with the seed vertex are used to construct new seed vertices, and this procedure is repeated until no unassociated tracks are left in the event or no additional vertex can be found.

Two variables are used to characterize a track's distance from the interaction point. The distance at the closest approach to the $z-$axis is d_0. The z-coordinate at the point of closest approach to the $z-$axis is z_0. An illustration of these two track impact parameters is shown in Figure 5.3.

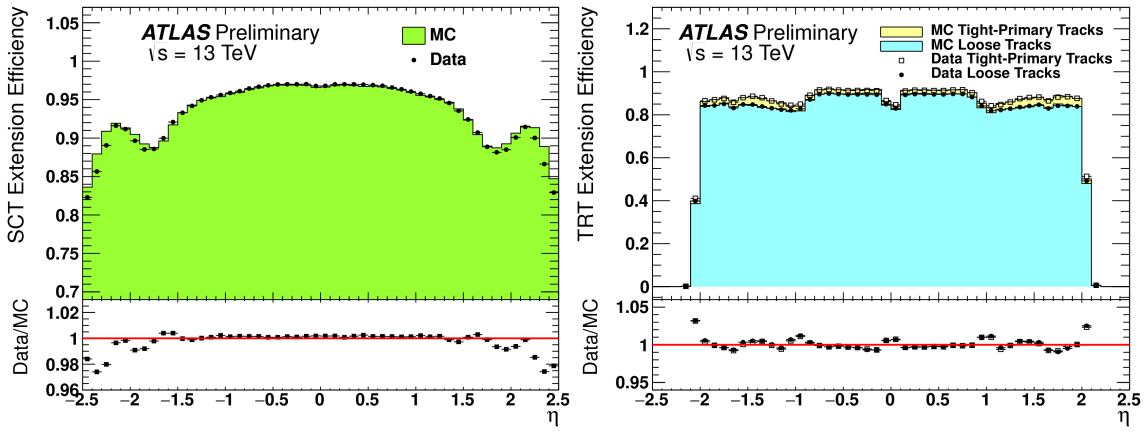


Figure 5.2: Efficiency to extend a track reconstructed in the pixel detector to the SCT (left) and efficiency to extend a silicon detector track to the TRT (right) [61]. The Tight track criteria require more hits in the ID systems compared to the Loose criteria. Both of the efficiencies are affected by the amount of material between the respective detector volumes.

[1] Missing track points, also called "holes", are defined as intersections of the reconstructed track trajectory with a sensitive detector element that do not result in a hit.

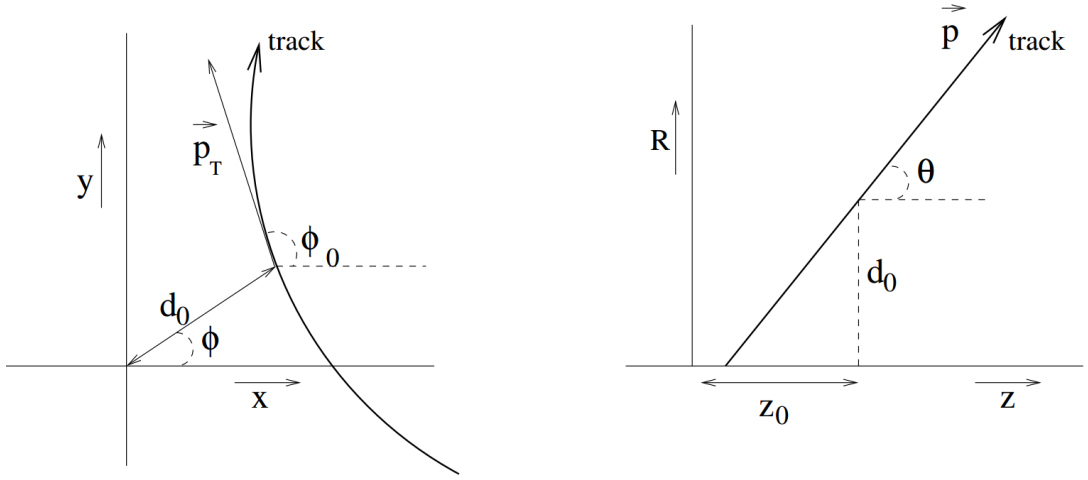


Figure 5.3: Illustration of the track impact parameters in the x–y and z–R planes. d_0 is the shortest distance from a track to the z–axis. z_0 is the z-coordinate of the track point closest to the z–axis.

5.2 Jet Reconstruction and Calibration

A quark or gluon produced in proton–proton collisions cannot be measured directly in ATLAS. Instead, a parton will produce a collimated spray of hadrons known as a jet. A jet leaves energy deposits in the EM and hadronic calorimeters, and charged particles will create tracks in the inner detector.

Jets are reconstructed in ATLAS by constructing "topological clusters" from the energy deposits in the calorimeters [63, 64]. Seed cells are chosen with energy measurements exceeding four times the amount of expected noise σ. Adjacent cells with at least 2σ energy measurements are added to the cluster, and then a final layer of clusters with positive energy above 0σ are included. The clusters are further grouped into jets using the anti-k_T jet clustering algorithm [65] with a distance parameter of $R = 0.4$ [2].

The energy response of the calorimeter must be properly characterized in order to reconstruct the true jet energy. The details of the jet energy calibration are presented in reference [66]. First, jets are built from cells calibrated with the EM calibration, which correctly measures the energy deposited by electromagnetic showers in the calorimeter. The jet energy is corrected for pile–up effects, then correction factors dependent on energy, η, and other qualities are applied. These stages of ATLAS jet calibration are shown in

[2] R appears in the denominator of the clustering distance metric and determines the radial size of the jet in η-ϕ space.

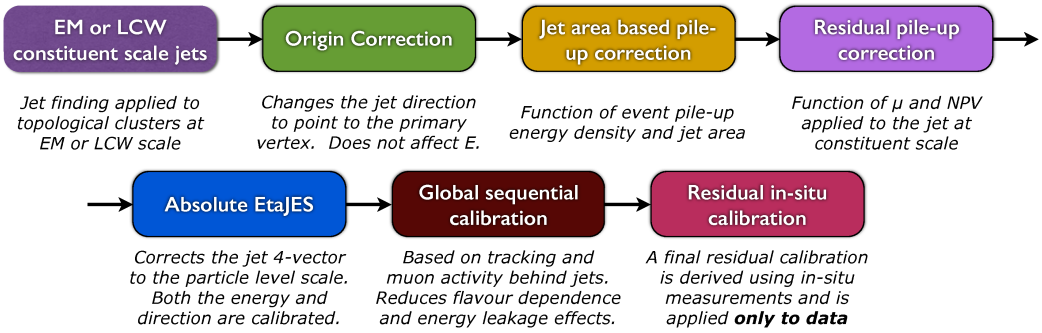


Figure 5.4: The stages of EM jet calibration [66].

Figure 5.4. The energy calibration of a jet needs to account for several different effects:

1. *Calorimeter non-compensation*: the different calorimeter responses to electromangetic and hadronic showers. Corrections are derived from the jet energy response (JES) in Monte Carlo and in data with balanced γ–jet events. In principle, the energy of the photon and the jet should be equivalent, and any discrepancy is due to non-compensation.

2. *Dead material* and *leakage*: energy lost in inactive areas of the detector or not contained in the calorimeter, respectively. These effects are mitigated with correction factors that depend on the topology of energy deposits in the calorimeter. For example, a shower with most of its energy in the outermost layer of the calorimeter was likely not fully contained, resulting in a smaller measured energy compared to the true energy.

3. *Out–of–calorimeter jet*: energy of particles which are not included in the reconstructed jet. This effect is compensated for with by studying the JES, the difference between the true particle energy and the reconstructed energy in simulation.

4. *Energy deposits below noise thresholds*: clusters are only formed by energy deposits which are much larger than the background noise. To determine the true energy of a jet, jet calibration must account for particles that do not form clusters and particles that fall outside the region of the topological clustering algorithm.

5. *Pile-up*: multiple proton–proton collisions in the same bunch crossing and residual signals from other bunch crossings will affect the energy deposition of jets. This effect is reduced using an area-

based subtraction method to remove the pile-up energy density and a residual pile-up correction to adjust the measured jet momentum as a function of the total amount of event pile-up.

The EM jet energy scale response as a function of jet η is shown in Figure 5.5.

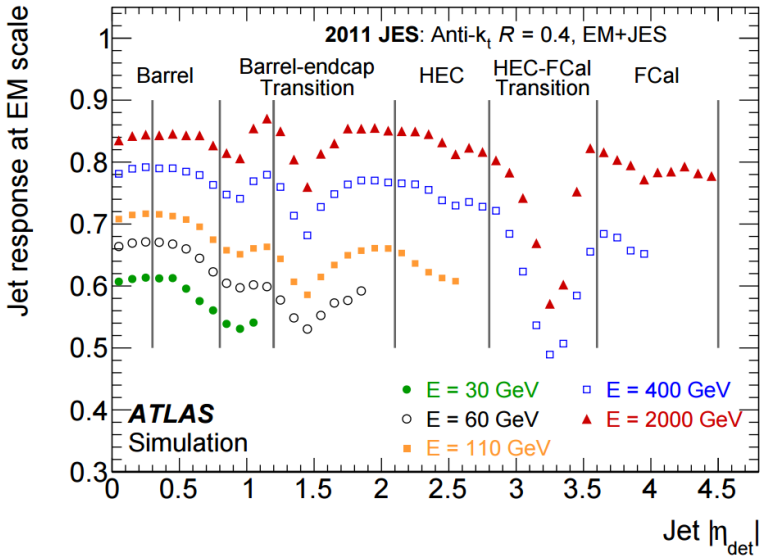


Figure 5.5: Jet response $p_T^{\text{reco}}/p_T^{\text{true}}$ of EM-scale jets after calibration as a function of true jet η in simulation [67]. Jet response is affected by detector geometry. The response is lower in transition regions where a jet will deposit energy in multiple calorimeter systems.

5.2.1 Track Association

Tracks in the inner detector are assigned to to jets through ghost association [68] that treats them as 4-vectors of infinitesimal magnitude during jet reconstruction. In addition to the baseline track requirements, jet tracks are required to have transverse momentum of at least 500 MeV and are either used in the fit to the selected primary vertex or have the longitudinal impact parameter with respect to the primary vertex satisfying $|z_0 \sin\theta| < 3.0$ mm.

5.3 Jet Identification and Cleaning

Jets produced in proton-proton collisions must be distinguished from misidentified jets of non-collision origin. The main backgrounds for jets coming from collision events are the following:

1. Beam induced background (BIB) due to proton losses upstream of the interaction point. These proton losses induce secondary cascades leading to muons that can reach the ATLAS detector and become a source of background for physics analyses [69]. The energy depositions created by these muons can be reconstructed as fake jets with energy as high as the beam energy. The rate of BIB is proportional to the beam current and depends on the operational conditions of the LHC, such as machine optics, collimator settings, residual gas densities, and filling scheme.

2. Cosmic-ray showers produced in the atmosphere overlapping with collision events. Since ATLAS is deep underground, the particles reaching the ATLAS detector are predominantly muons.

3. Calorimeter noise from large scale coherent noise or isolated pathological cells. Calorimeter cells which are permanently or sporadically very noisy are masked[3] prior to the jet and missing transverse momentum reconstruction. The former is always masked in the event reconstruction, while the sporadically very noisy cells are masked on an event-by-event basis. Events are discarded if they are identified as having a large amount of coherent noise. Most of the noise is already identified and rejected by the data quality inspection [70] performed shortly after the data taking based on standardised quality criteria. A small fraction of calorimeter noise remains undetected and needs to be rejected by additional criteria.

The two first sources of background are referred to as non-collision backgrounds.

Jet quality variables

Several variables were introduced to discriminate fake and good jets (defined in Appendix A) in References [69, 71] and can be divided into three categories: variables based on signal pulse shape in the LAr calorimeters, energy ratio variables, and track-based variables. Pulse shape variables provide good discrimination against noise in the LAr calorimeters. The energy ratio variable and track-based variables are effective at rejecting calorimeter noise in the LAr and Tile calorimeters, in addition to rejecting beam-induced background and cosmic muon showers.

[3] The fraction of cells permanently masked is smaller than one per mil and the fraction of cells that are conditionally masked is smaller than one per mil.

In order to reject fake jets due to significant coherent or sporadic noise in the LAr calorimeters, the characteristic ionisation signal shape can be used to discriminate between real and fake energy deposits. The cell-level quantity ($Q_{\text{cell}}^{\text{LAr}}$) introduced in Section 4.3.3 is used to define several jet-level quantities:

- $\langle \text{Q} \rangle$: The average jet quality is defined as the energy–squared weighted average of the pulse quality of the calorimeter cells ($Q_{\text{cell}}^{\text{LAr}}$) in the jet. This quantity is normalized such that $0 < \langle \text{Q} \rangle < 1$.

- $\text{f}_{\text{Q}}^{\text{LAr}}$: Fraction of the energy in the LAr calorimeter cells of a jet with poor signal shape quality defined as $Q_{\text{cell}}^{\text{LAr}} > 4000$.

- $\text{f}_{\text{Q}}^{\text{HEC}}$: Fraction of the energy in the HEC calorimeter cells of a jet with poor signal shape quality defined as $Q_{\text{cell}}^{\text{LAr}} > 4000$.

Finally, since sporadically noisy cells in the calorimeter can generate large fake energy deposits as well as large fake negative energy deposits, a variable, E_{neg}, summing the energy of all cells with negative energy is introduced. The presence of negative energy in a good jet is due to the electronic and pile-up noise. The distributions of these four variables can be found in Figure 5.6 in the good and fake jets enriched samples.

In the good jet enriched sample, the variables $\langle \text{Q} \rangle$, $\text{f}_{\text{Q}}^{\text{LAr}}$ and $\text{f}_{\text{Q}}^{\text{HEC}}$ have a high population of jets at zero. Values different from zero are due to electronic and pile-up noise which can distort the measured pulse shape. Non-zero values are also caused by differences in the pulse shape between data and the expectation used in the calculation of $Q_{\text{cell}}^{\text{LAr}}$. Since the simulation uses a consistent pulse shape, it predicts values closer to zero generated only by the electronic and pile-up noise. Simulated distributions are therefore not shown for these three variables. In the fake jets enriched sample, the variables $\langle \text{Q} \rangle$, $\text{f}_{\text{Q}}^{\text{LAr}}$ and $\text{f}_{\text{Q}}^{\text{HEC}}$ contain a higher proportion of jets with larger values. Values close to one are mainly due to large coherent noise or sporadically very noisy cells in the calorimeters and intermediate values are mainly due to beam-induced background.

Most of the jets have a low value of $|\text{E}_{\text{neg}}| < 50$ GeV, except a population of fake jets with $|\text{E}_{\text{neg}}| > 60$ GeV which also has large values of $\text{f}_{\text{Q}}^{\text{HEC}}$. Those jets are mainly due to sporadic noise bursts in the HEC [71]. Good agreement is observed between data and the simulation in the good jets enriched sample at low values but discrepancies in the tails are observed where the simulation over–predicts the data.

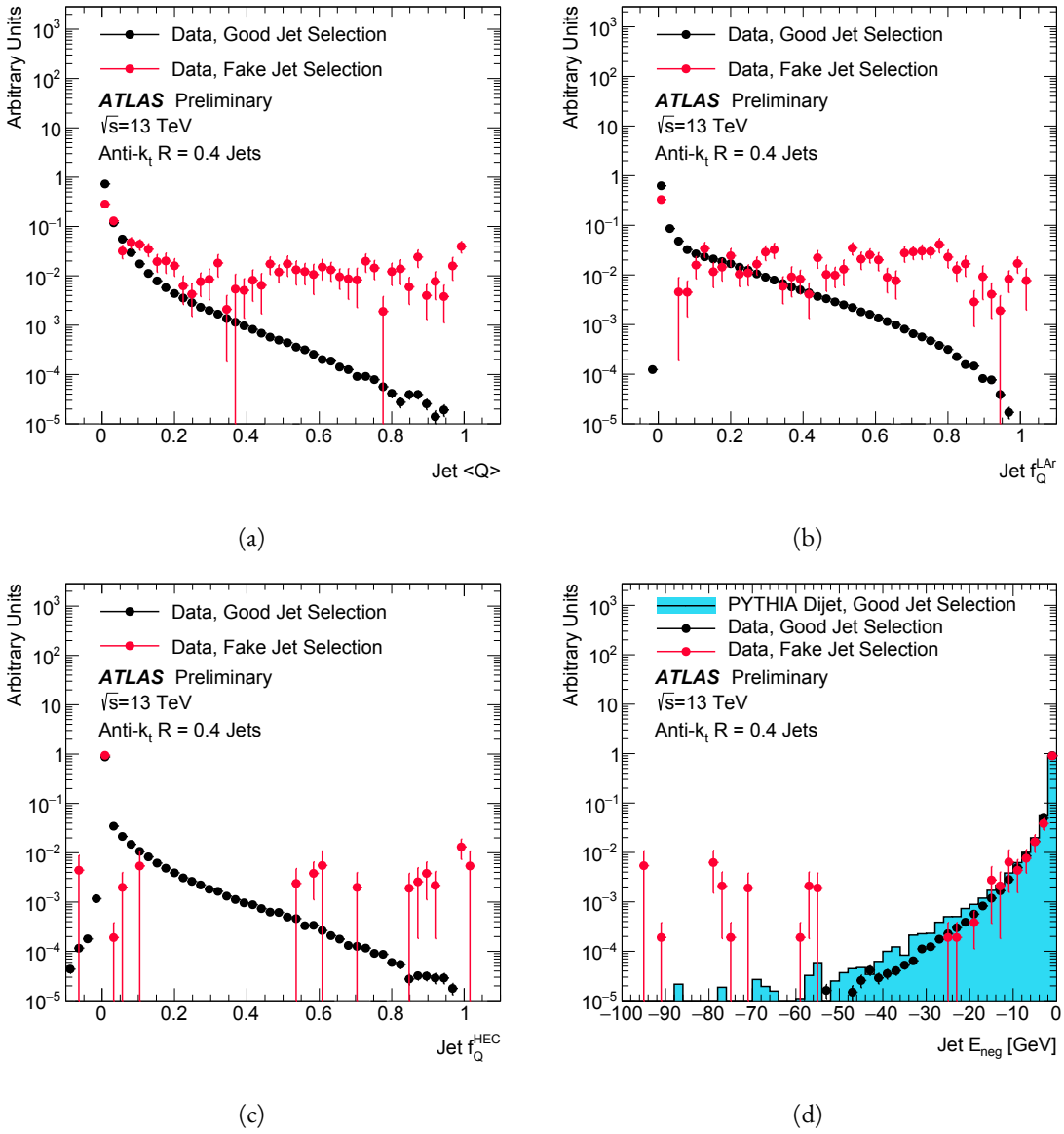


Figure 5.6: Distributions of f_Q^{LAr} (a), f_Q^{HEC} (b), $\langle Q \rangle$ (c) and E_{neg} (d) in the good jets enriched sample for data (black points). Monte Carlo (blue histogram) is not expected to model the jet pulse quality variables and thus is only shown for (d). Distributions from the fake jets enriched samples are superimposed (red points). Good jets tend to have $\langle Q \rangle$, f_Q^{LAr} and f_Q^{HEC} at zero. Deviations from zero are due to electronic noise and differences between the measured and expected pulse shape, which is exacerbated for fake jets. The population of fake jets at $|E_{neg}| > 60$ GeV is due to sporadic noise bursts in the HEC [71].

Energy ratio variables

Jets originating from beam-induced background or calorimeter noise tend to be more localised longitudinally in the calorimeters than jets from proton-proton collisions. Therefore, the jet energy deposits along

the expected direction of the shower development can be employed to discriminate between good jets and jets arising from non-collision backgrounds. The electromagnetic fraction (f_{EM}) is defined as the ratio of the energy deposited in the electromagnetic calorimeter to the total energy of the jet. Similarly, the HEC energy fraction (f_{HEC}) is defined as the ratio of the energy deposited in the HEC calorimeter to the total energy. The ATLAS calorimeters are segmented in depth and the maximum energy fraction in any single calorimeter layer (f_{max}) can be used as a discriminating variable between fake and good jets. All of these ratio variables are computed at the electromagnetic energy scale. The distributions of three variables can be found in Figure 5.7. Figure 5.8 shows f_Q^{LAr} as a function of the electromagnetic fraction for the fake and good jets enriched samples.

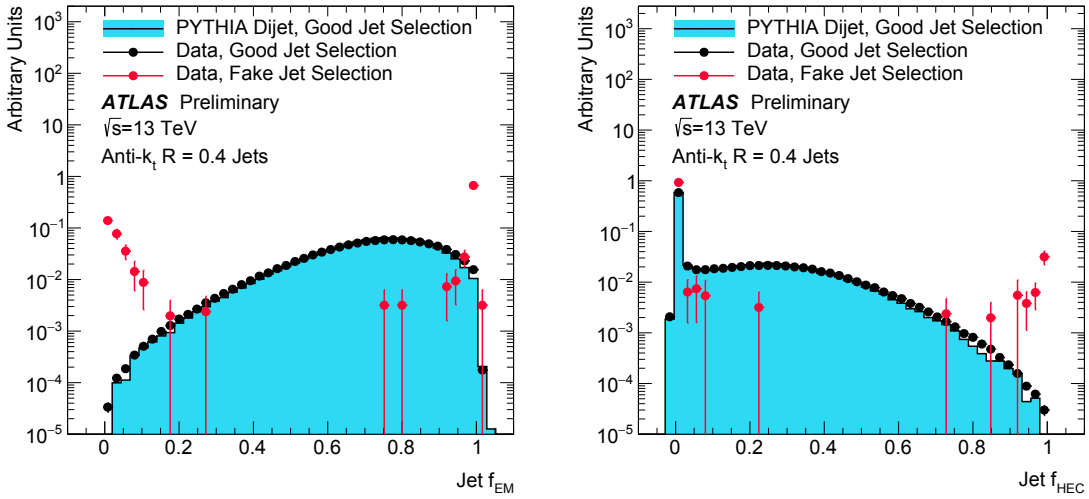
Good jets have a smooth distribution for these three variables. Jets that fall outside of the HEC acceptance exhibit a peak at $f_{HEC} = 0$. The fake jets distribution has very high or very low values for both f_{EM} and f_{HEC}, and high values for f_{max}. Good agreement is observed between data and the simulation for good jets.

Track based variables

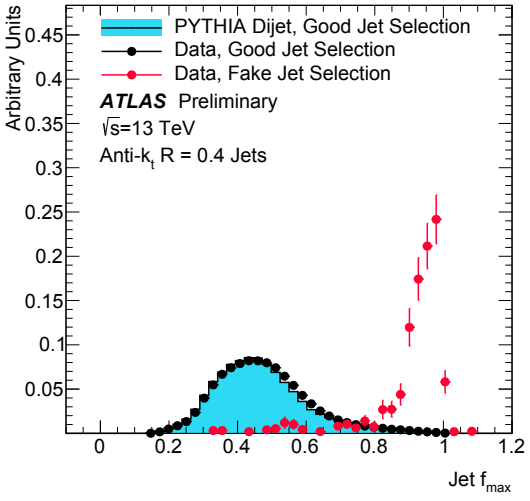
Most real jets contain charged hadrons which can be reconstructed by the ID tracking system for jets in the tracker acceptance. The jet charged fraction (f_{ch}) is defined as the ratio of the scalar sum of the p_T of the tracks coming from the primary vertex (see Section 5.1) associated to the jet divided by the jet p_T . This variable is used to discriminate between jets produced in collision events from fake jets, for jets within the tracking acceptance.

The ratio between the jet charged particle fraction and the jet energy fraction in the layer with maximum energy deposit (f_{ch}/f_{max}) was also found to discriminate between good and fake jets.

The distributions of these variables are given in Figure 5.9 for jets with $|\eta| < 2.4$ and Figure 5.10 shows the jet charged fraction as a function of the electromagnetic fraction for the fake and good jets enriched samples. The fake jets have low values for f_{ch} and f_{ch}/f_{max} while only a small fraction of good jets have low values. Good agreement is observed between data and the simulation for good jets.

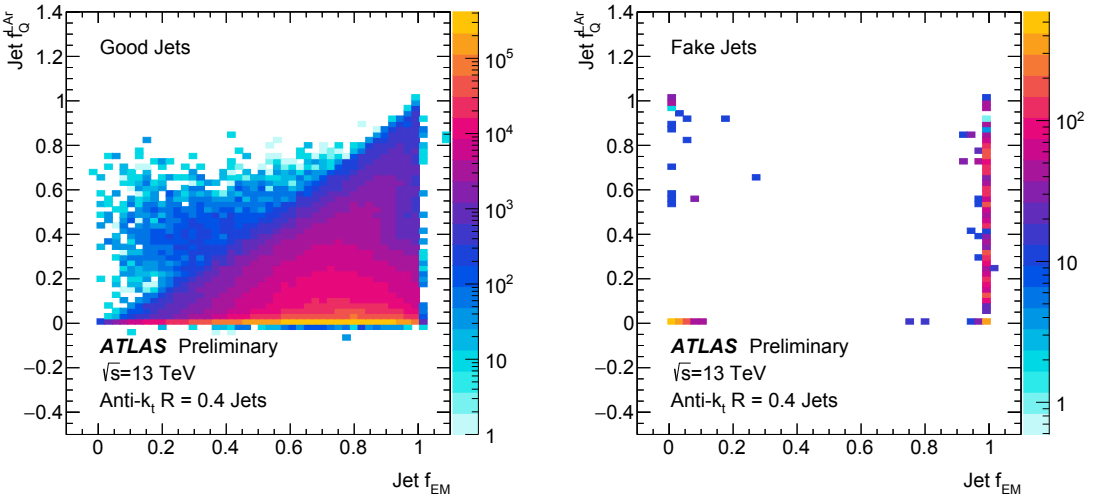


(a) (b)



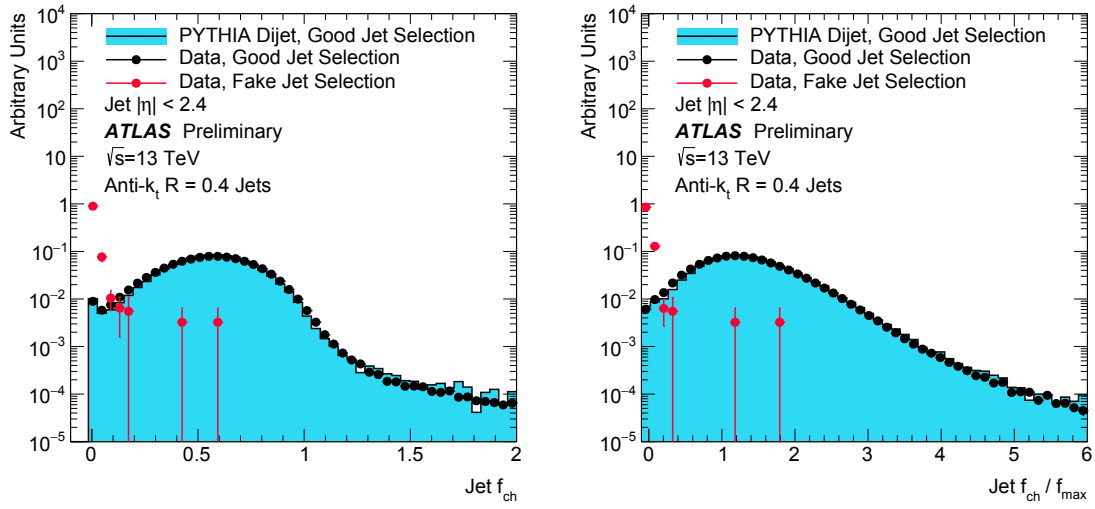
(c)

Figure 5.7: Distributions of f_{EM} (a), f_{HEC} (b), and f_{max} (c) in the good jets enriched sample for both data (black points) and the simulation (blue histograms). Distributions from the fake jets enriched samples are also superimposed (red points). Good jets have a smooth distribution for these three variables. Jets that fall outside of the HEC acceptance exhibit a peak at $f_{HEC} = 0$. The fake jets distribution has very high or very low values for both f_{EM} and f_{HEC}, and high values for f_{max}.



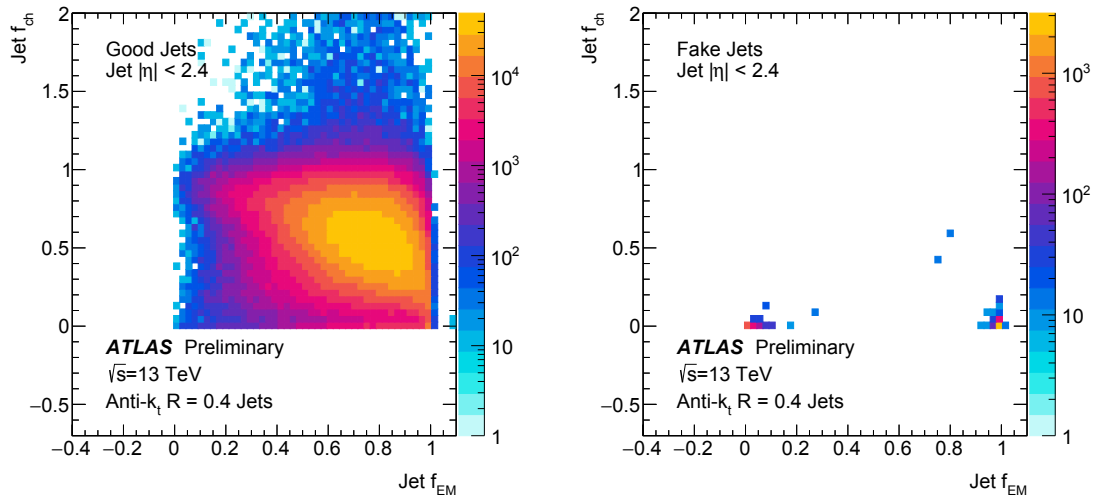
(a) (b)

Figure 5.8: Distribution of f_Q^{LAr} as a function of the electromagnetic fraction for the good (a) and fake (b) jets enriched samples in data. Since the EM calorimeter is a LAr system, good jets with high f_{EM} are more likely to have high f_Q^{LAr}. Fake jets with high f_Q^{LAr} and low f_{EM} are due to noise.



(a) (b)

Figure 5.9: Distributions of f_{ch} (a) and f_{ch}/f_{max} (b) for $|\eta| < 2.4$ in the good jets enriched sample for both data (black points) and the simulation (blue histograms). Distributions from the fake jets enriched samples are also superimposed (red points). The fake jets have low values for f_{ch} and f_{ch}/f_{max} while only a small fraction of good jets have low values.



(a) Good jets

(b) Fake jets

Figure 5.10: Distribution of f_{ch} as a function of the electromagnetic fraction for the good (a) and fake (b) jets enriched samples in data. Good jets are most likely to have central values of f_{ch} and f_{EM}, whereas for fake jets these two variables are largely uncorrelated.

Jet quality selection

Two selections to identify fake jets are defined: BadLoose and BadTight. The BadLoose selection, initially introduced in References [69, 71][4], is designed for high good jet efficiency, while maintining as high fake jet rejection as possible. A jet is identified as a BadLoose jet if it satisfies at least one of following criteria:

1. $f_{HEC} > 0.5$ and $|\, f_Q^{HEC} \,| > 0.5$ and $\langle Q \rangle > 0.8$
2. $|\, E_{neg} \,| > 60$ GeV
3. $f_{EM} > 0.95$ and $LArQuality > 0.8$ and $\langle Q \rangle > 0.8$ and $|\, \eta \,| < 2.8$
4. $f_{max} > 0.99$ and $|\, \eta \,| < 2$
5. $f_{EM} < 0.05$ and $f_{ch} < 0.05$ and $|\, \eta \,| < 2$
6. $f_{EM} < 0.05$ and $|\, \eta \,| \geq 2$

[4] This working point was called Looser in these references.

The first two criteria are introduced to identify jets mainly due to sporadic noise bursts in the HEC. The third selection has the purpose to identify jets due to large coherent noise or isolated pathological cells in the electromagnetic calorimeter. The last three requirements are more general and are used to identify hardware issues, beam-induced background and cosmic muon showers.

The BadTight selection is designed to provide a much higher fake jet rejection with an inefficiency for good jets of up to a few percent. It adds a single criterion which is based on the ratio between the f_{ch} and f_{max}. This ratio is very efficient at discriminating fake jets (which have preferentially f_{ch} close to 0 and f_{max} close to 1) and jets from proton-proton collisions which have preferencially $f_{ch} > 0$ and $f_{max} < 1$ as shown in Figure 5.9. A jet is identified as a BadTight jet if it is a BadLoose jet or if it satisfies: $f_{ch}/f_{max} < 0.1$ for $|\eta| < 2.4$.

These criteria were initially introduced in the ATLAS search for new phenomena in final states with an energetic jet and large missing transverse momentum [72]. This analysis is one of the those which needs the most restrictive jet selection due to the similar event topology of non-collision backgrounds and the final states analysed. Usage of BadTight criteria in this search reduced the non-collision backgrounds to a negligible level compared to the Standard Model backgrounds from proton-proton collisions for this analysis that is highly sensitive to calorimeter noise, beam-induced background, and cosmic muon showers.

A jet is identified as a Loose jet if it is not identified as a BadLoose jet, and a jet is identified as a Tight jet if it is not identified as a BadTight jet. Figure 5.11 show kinematic distributions for the fake jets enriched sample before the jet quality selection and after applying the Loose and Tight jet selections. The Tight selection provides very good rejection of the fake jets enriched sample, in particular at high jet transverse momentum. The peaks at $\phi = 0$ and $\pm\pi$, which are characteristic of beam background [69], are eliminated by the Tight selection. It should also be noted that the beam-induced background peaks at low $|\eta|$ values due to the requirements on the jet transverse momentum and the jet timing [69].

Jet selection efficiency measurement

The efficiencies of the jet quality selections are measured using a "tag-and-probe" method. Good dijet events, as described in Appendix A, are selected by modifying the jet transverse momentum criterion to be

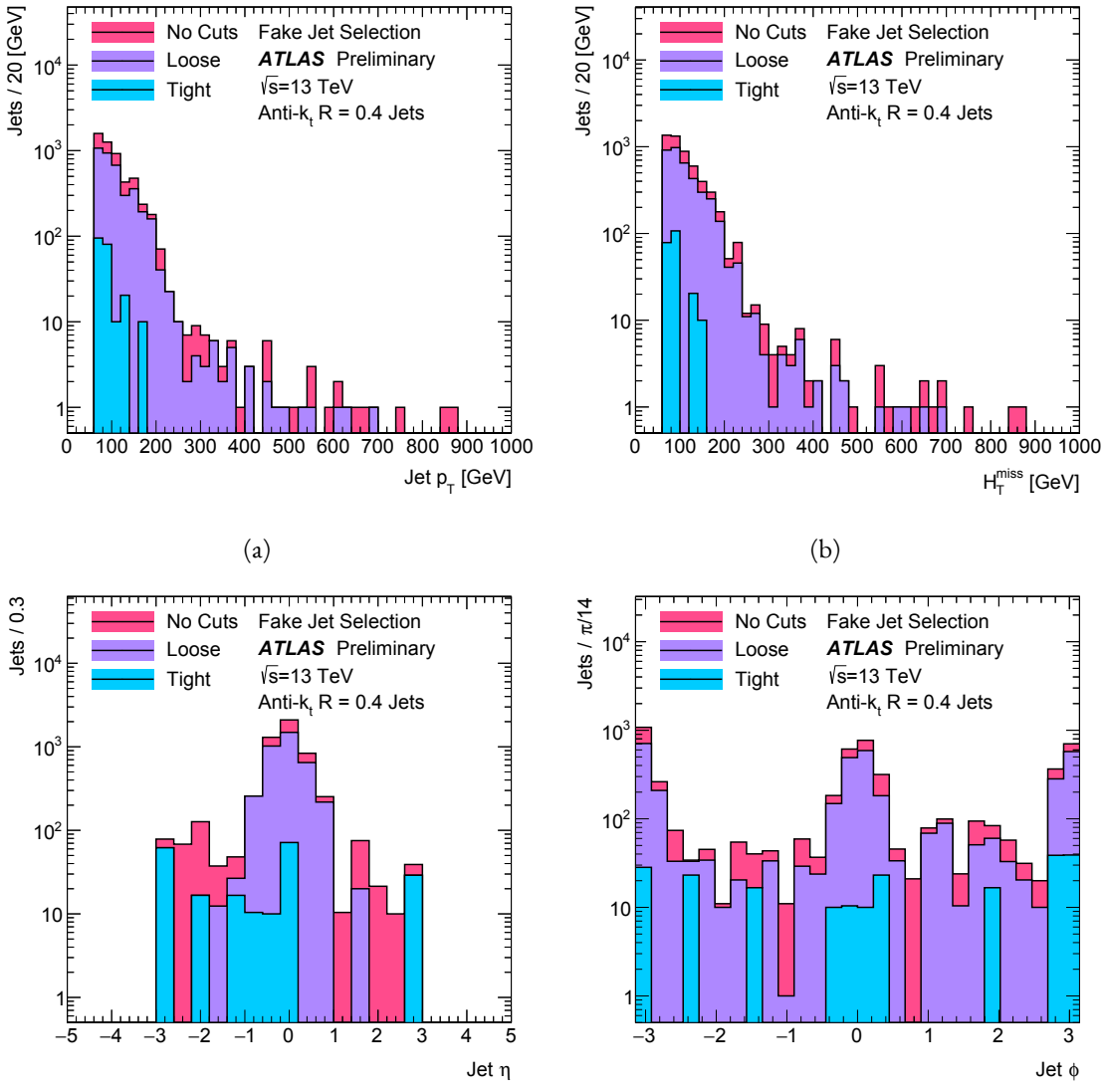


Figure 5.11: Jet transverse momentum (a), $H_{\mathrm{T}}^{\mathrm{miss}}$ (b), η (c), and ϕ (d) distributions for the fake jets enriched sample before and after the jet quality selection. The Loose criteria does not have strong rejection power, but the Tight criteria rejects $\mathcal{O}(10^3)$ of the fake jets. Surviving events have low jet p_T and $H_{\mathrm{T}}^{\mathrm{miss}}$.

greater than 20 GeV instead of 70 GeV.

The tag jet is required to pass the Tight version of the jet quality selections, and to be back-to-back in the transverse plane with the probe jet. Among the two leading jets, each jet can play the role of the probe jet as long as the other jet satisfies the tag criteria. The sample of probe jets is used to measure the jet quality selection efficiency defined as the fraction of probe jets that are not rejected by the jet quality selection criteria as a function of η and p_T of the probe jets.

The resulting efficiencies for anti-k_T jets with $R = 0.4$ for the two selection criteria are shown as a function of η for $p_T > 100$ GeV in Figure 5.12. The jet quality selection efficiency of the Loose selection is greater than 99.9% over all η bins except in one bin at very high η. The Tight selection efficiency is lower in the central-η region due to the cut on f_{ch}/f_{max}. Otherwise, the Tight selection has $> 99.5\%$ efficiency over all η bins except in one bin at very high η.

Similarly, Figure 5.13 shows the jet quality selection efficiencies[5] as a function of p_T for various η ranges. The jet quality selection efficiency of the Loose selection is greater than 99.5% over all p_T bins. The Tight selection efficiency is lower in the central-η region due to the cut on f_{ch}/f_{max}. Otherwise, the Tight selection has an efficiency greater than 95% over all p_T bins. Jet quality selection efficiencies in data are compared to the simulation and very good agreement is observed.

[5]It should be noted that for jets with $p_T < 50$ GeV and within the tracker acceptance, additional criteria were designed to select jets from the hard-scatter and to reject pile-up jets using the jet-vertex-tagger described in Reference [73]. When this tagger is employed, an inefficiency at selecting signal jets is introduced which is of the order of 10% for p_T =20 GeV. The jets rejected by this tagger have a large overlap with those rejected by the f_{ch}/f_{max} requirement of the tight selection, making the efficiency of the tight cut close to 100% at 20 GeV for jets selected using the jet-vertex-tagger.

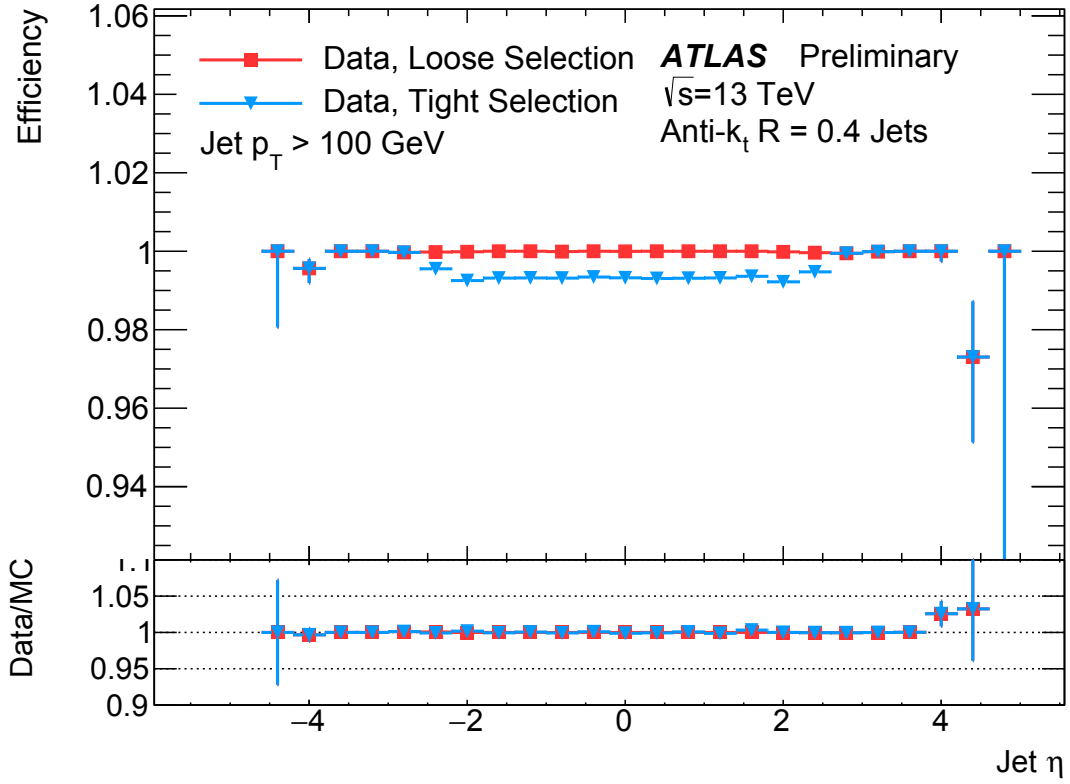
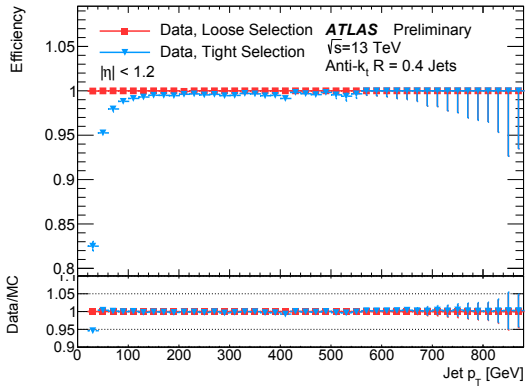
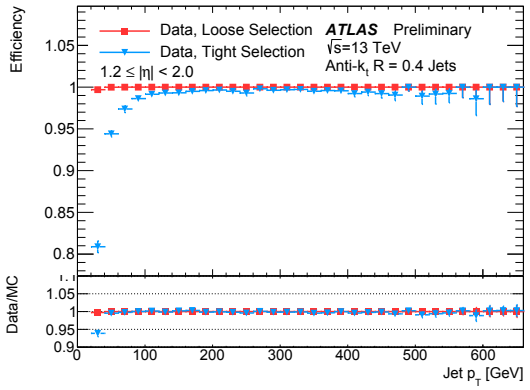


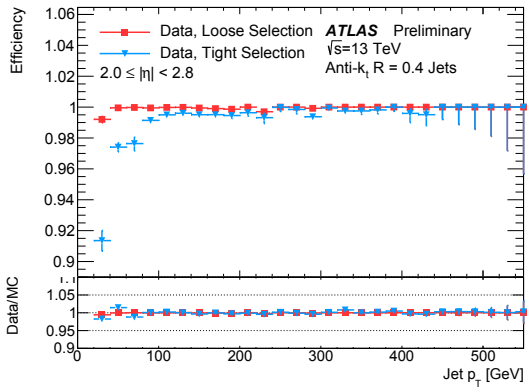
Figure 5.12: Jet quality selection efficiency for anti-k_T jets with $R = 0.4$ measured with a tag-and-probe technique as a function of η for p_T >100 GeV, for the Loose and Tight selection criteria. Only statistical uncertainties are shown. The lower portion of the figure shows ratios of efficiencies measured in data and Monte Carlo simulation (PYTHIA). The Tight criteria is only defined within $|\eta| < 2.4$.



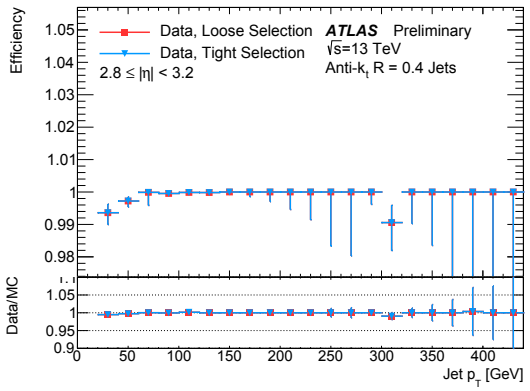
(a) $|\eta| < 1.2$



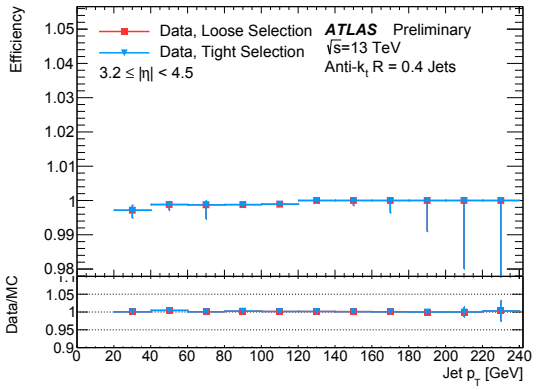
(b) $1.2 \leq |\eta| < 2$



(c) $2 \leq |\eta| < 2.8$



(d) $2.8 \leq |\eta| < 3.2$



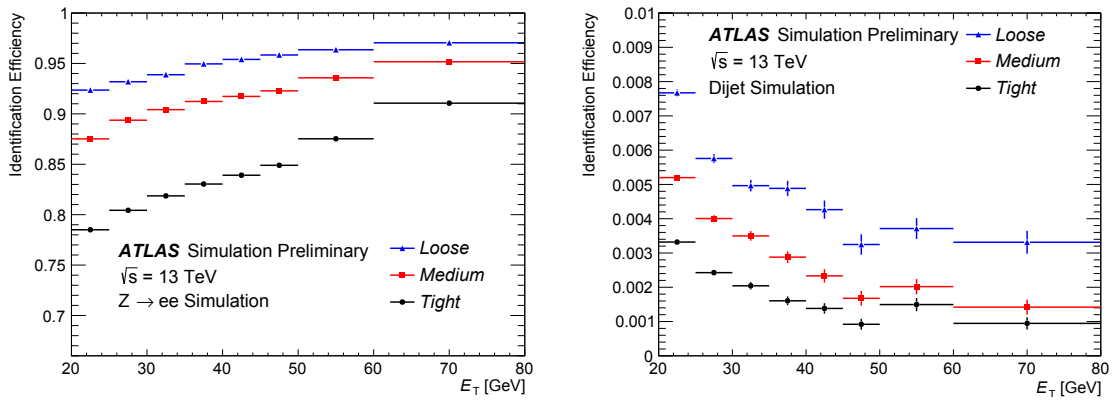
(e) $4.2 \leq |\eta| < 4.5$

Figure 5.13: Jet quality selection efficiency for anti-k_T jets with $R = 0.4$ measured with a tag-and-probe technique as a function of p_T in η ranges, for the Loose and Tight selection criteria. Only statistical uncertainties are shown. The lower portion of the figure shows ratios of efficiencies measured in data and Monte Carlo simulation.

5.4 Electrons and Muons

Electrons traversing the ATLAS detector are recorded as tracks in the inner detector and energy deposits in the electromagnetic calorimeter. Electrons with $p_T > 7$ GeV and $|\eta| < 2.47$ are reconstructed. In the EM calorimeter, seed clusters are constructed with a sliding window algorithm [6] that searches for towers with transverse energy larger than 2.5 GeV. Cluster kinematics are reconstructed using an extended window. In the ID, seed tracks are selected that are incompatible with pions and have $p_{\mathrm{T}} > 1$ GeV. These tracks are re-fit to ID hits using a Gaussian Sum Filter (GSF) algorithm to estimate electron parameters [74]. Electron candidates are built by matching seed tracks to seed clusters [75]. The energy is taken from the calibrated cluster, and the η and ϕ directions are taken from the matched track.

Electron candidates must be distinguished from hadronic jets or converted photons. Calorimeter shower shapes, transition radiation, track-cluster matching quantities, track properties, and variables measuring bremsstrahlung effects are used to construct a set of electron identification criteria. A likelihood-based multivariate analysis technique evaluates several properties of the electron candidates and calculates an overall probability for the object to be signal or background [75]. Figure 5.14 shows the algorithm's reconstruction efficiency for true and fake electrons for three different identification criteria.



(a) (b)

Figure 5.14: Reconstruction efficiency as a function of electron E_T for both true electrons (left) and hadrons (right) for three different identification criteria [75]. Tighter quality requirements result in decreased efficiency but increased rejection.

[6] The sliding window has a size of 3×5 in units of 0.025×0.025 in $\eta \times \phi$, corresponding to the granularity of the EM calorimeter middle layer

Muons pass through all layers of the ATLAS detector, leaving tracks in the ID and muon spectrometer. Muon reconstruction begins by building local straight line tracks, called segments, in each muon chamber. These segments are fit to larger tracks traversing the entire muon spectrometer, called "standalone" muon tracks. The standalone tracks are matched to ID tracks construct "combined" muons with both tracks determining the momentum and direction of the muon [76]. Combined muons are reconstructed with $|\eta| < 2.5$ and $p_T > 10$ GeV. Muon identification criteria are constructed using the χ^2 match between the ID and MS tracks, the number of hits in the ID, overall ID and MS track fit quality, and additional variables. Figure 5.15 shows the muon reconstruction efficiency.

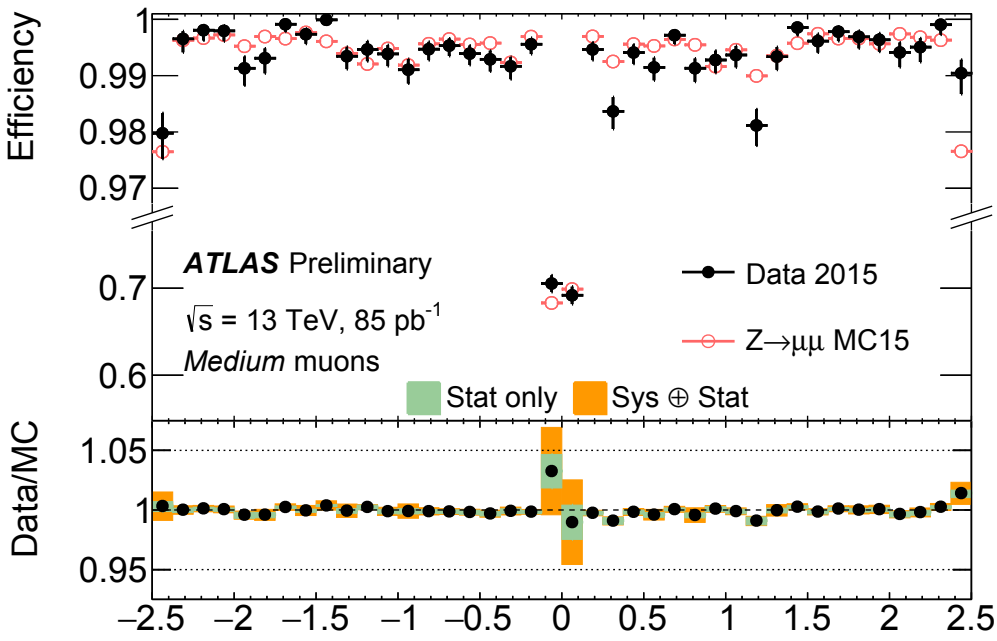


Figure 5.15: Muon reconstruction efficiency as a function of muon η [76]. At $|\eta| < 0.1$ the ATLAS muon spectrometer is only partially instrumented to allow for cabling and services to the calorimeters and inner detector.

5.5 Missing Transverse Energy

Long-lived particles that do not interact via the strong or electromagnetic forces will pass through ATLAS without interacting with any of the detector systems. Although the net longitudinal momentum of the

incoming partons that collide is not known [7], protons have no net momentum in the plane transverse to the beam line. Therefore, if all particles in the final state can be reconstructed in the ATLAS detector, by conservation of momentum the total transverse momentum should be zero. Similarly, if the final state contains one or more invisible particles the reconstructed topology will have nonzero total transverse momentum. The magnitude of the momentum vector that restores transverse momentum conservation is called missing transverse momentum ($E_{\mathrm{T}}^{\mathrm{miss}}$).

$E_{\mathrm{T}}^{\mathrm{miss}}$ is reconstructed using calibrated objects, and is calculated as [77, 78]:

$$\begin{aligned} E_x^{\mathrm{miss}} &= E_x^{\mathrm{miss},\,e} + E_x^{\mathrm{miss},\,\gamma} + E_x^{\mathrm{miss},\,\tau} + E_x^{\mathrm{miss,\,jets}} + E_x^{\mathrm{miss},\,\mu} + E_x^{\mathrm{miss,\,soft}} \\ E_y^{\mathrm{miss}} &= E_y^{\mathrm{miss},\,e} + E_y^{\mathrm{miss},\,\gamma} + E_y^{\mathrm{miss},\,\tau} + E_y^{\mathrm{miss,\,jets}} + E_y^{\mathrm{miss},\,\mu} + E_y^{\mathrm{miss,\,soft}} \end{aligned} \tag{5.1}$$

The terms for jets, charged leptons, and photons are the negative sum of the momenta for the respective objects. Double-counting of objects in the detector is avoided by keeping track of calorimeter deposits, which are associated to objects in the following order: electrons (e), photons (γ), hadronically decaying tau-leptons (τ), jets, and muons (μ). The soft term is calculated from ID tracks not associated with any of the jets, electrons, or muons entering the $E_{\mathrm{T}}^{\mathrm{miss}}$ calculation.

[7] Each colliding parton carries an fraction of the proton's momentum

Part III

Searching for Evidence of Dark Matter in Mono–Jet Events

6

Event Selection

The mono–jet topology must be defined by a specific set of cuts applied to the events collected by the ATLAS Detector. This is the "signal region": a part of event phase space in which dark matter production may be evident. Background processes will also produce events that enter this signal region. W and Z bosons produced in association with jets, top quark processes, and diboson events are all backgrounds to Dark Matter production.

Any excess of observed events above the number expected from known physics may be evidence of dark matter. The contribution of background processes must be well understood in order to determine if a signal is arising from true new physics or poor background modeling. This chapter describes the Monte Carlo simulation, data sample, and signal region event selection.

6.1 Data Sample and Trigger

The data sample considered in this thesis was collected with tracking detectors, calorimeters, muon chambers, and magnets fully operational, and corresponds to a total integrated luminosity of 3.2 fb^{-1}. The data were selected online using a trigger logic that selects events with E_T^{miss} above 70 GeV, as computed at the final stage of the two-level trigger system of ATLAS. With the final analysis requirements, the trigger selection is fully efficient for $E_T^{\text{miss}} > 250$ GeV, as determined using a data sample with muons in the final state, as shown in Table 6.1.

Sample	SR	CR1μ	CR1μ + muon trigger
$Z \to \nu\nu$ MC	0.998 ± 0.001		
$W \to \mu\nu$ MC	1.000 ± 0.003	0.998 ± 0.001	0.998 ± 0.001
$m_\chi = 50$ GeV, $m_A = 10$ TeV	1.000 ± 0.001		
Data		1.000 ± 0.001	1.000 ± 0.002

Table 6.1: Trigger efficiency for the E_T^{miss} trigger requirement for different samples in different regions with jet p_T > 250 GeV. The turn-on point for $Z \to \nu\nu$ in SR is around $E_T^{\text{miss}} = 150$ GeV, while the plateau is reached around $E_T^{\text{miss}} = 210$ GeV.

6.2 Background and Signal Simulation

The kinematics of all Standard Model background processes are estimated using Monte Carlo simulation. The estimation of yields from these processes is described in Chapter 7. The kinematics and cross sections of WIMP signal models is also determined from Monte Carlo. This section describes the generators and settings used to simulate these background and signal processes.

Events containing W or Z bosons with associated jets are simulated using the SHERPA-2.1.1 [79] generator. Matrix elements (ME) are calculated for up to two partons at next-to-leading order (NLO) and four partons at leading order (LO) using the Comix [80] and OpenLoops [81] matrix element generators and merged with the SHERPA parton shower (PS) [82] using the ME+PS@NLO prescription [83]. The CT10 [84] parton distribution function (PDF) set is used in conjunction with a dedicated parton shower tuning developed by the authors of SHERPA. The MC predictions are initially normalized to next-to-next-to-leading-order (NNLO) perturbative QCD (pQCD) predictions according to DYNNLO [85, 86]

using MSTW2008 90% CL NNLO PDF sets [87].

For the generation of $t\bar{t}$ and single top-quarks in the Wt-channel and s-channel the POWHEG-BOX v2 [88] generator with the CT10 PDF sets in the matrix element calculations is used. Electroweak t-channel single top-quark events are generated using the POWHEG-BOX v1 generator. This generator uses the four-flavor scheme for the calculations of NLO matrix elements with the fixed four-flavor PDF set CT10. The parton shower, fragmentation, and underlying event are simulated using PYTHIA-6.428 [89] with the CTEQ6L1 [90] PDF sets and the corresponding Perugia 2012 set of tuned parameters (P2012 tune) [91]. The top-quark mass is set to 172.5 GeV. The EvtGen v1.2.0 program [92] is used to model the decays of the bottom and charm hadrons. Finally, diboson samples (WW, WZ, and ZZ production) are generated using SHERPA-2.1.1 with CT10 PDFs and are normalized to NLO pQCD predictions [93]. The diboson samples are also generated using POWHEG interfaced to PYTHIA-8.186 and using CT10 PDFs for studies of systematic uncertainties.

WIMP signals are simulated in POWHEG-BOX v2 [94–96] using revision 3049 of the DMV model implementation of WIMP pair production with s-channel spin-1 mediator exchange at NLO precision including parton showering effects, introduced in Ref. [97]. Renormalization and factorization scales are set to $H_{\mathrm{T}}/2$ on an event-by-event basis, where $H_{\mathrm{T}} = \sqrt{m_{\chi\chi}^2 + p_{\mathrm{T},j1}^2} + p_{\mathrm{T},j1}$ is defined by the invariant mass of the WIMP pair ($m_{\chi\chi}$) and the transverse momentum of the hardest jet ($p_{\mathrm{T},j1}$). A Breit–Wigner distribution is chosen to describe the mediator propagator. Events are generated using the NNPDF30NLO [98] parton distribution functions and interfaced to PYTHIA-8.205 with the ATLAS A14 tune for parton showering. Couplings of the mediator to WIMPs and quarks are set to $g_\chi = 1$ and $g_q = 0.25$, leading to narrow-width mediators with $\Gamma_A/m_A \lesssim 5\%$. A grid of samples is produced for WIMP masses ranging from 1 GeV to 1 TeV and mediator masses between 10 GeV and 2 TeV [1].

Differing pileup conditions as a function of the instantaneous luminosity are taken into account by overlaying simulated minimum-bias events generated with PYTHIA onto the hard-scattering process. The MC-generated samples are processed with a full ATLAS detector simulation [99] based on the GEANT4 program [100]. The simulated events are reconstructed and analyzed with the same analysis chain as for

[1] In the generation of the samples, the *bornktmin* and *bornsuppfact* MC parameters [94] are set to 150 GeV and 1 TeV, respectively, in order to suppress the generation of events at low E_T^{miss}.

the data, using the same trigger and event selection criteria.

6.3 Object Selection

The signal region is defined using the jets, leptons, and missing transverse momentum in each event. The reconstruction of these objects is covered in detail in Chapter 5. Additional cuts and requirements are applied to the objects used in the analysis, described below.

6.3.1 Jets

Jets are reconstructed from energy deposits in the calorimeters using the anti-kt jet algorithm [101] with the radius parameter (in η–ϕ space) set to 0.4. The measured jet transverse momentum is corrected for detector effects, including the noncompensating character of the calorimeter, by weighting energy deposits arising from electromagnetic and hadronic showers differently. In addition, jets are corrected for contributions from pileup, as described in Ref. [102]. Jets with corrected $p_{\mathrm{T}} > 20\,\mathrm{GeV}$ and $|\eta| < 2.8$ are initially considered in the analysis. In order to remove jets originating from pileup collisions, for central jets ($|\eta| < 2.4$) with $p_{\mathrm{T}} < 50\,\mathrm{GeV}$ a significant fraction of the tracks associated with each jet must have an origin compatible with the primary vertex, as defined by the jet-vertex tagger [73].

6.3.2 Leptons

The presence of leptons (electrons or muons) in the final state is used in the analysis to define control samples and to reject background contributions in the signal regions (see Chapter 7). Electron candidates are initially required to have $p_{\mathrm{T}} > 20\,\mathrm{GeV}$ and $|\eta| < 2.47$, and to satisfy the loose electron shower shape and track selection criteria described in Refs. [103, 104]. Overlaps between identified electrons and jets in the final state are resolved by discarding jets if their separation $\Delta R = \sqrt{(\Delta\eta)^2 + (\Delta\phi)^2}$ from an identified electron is less than 0.2. The electrons separated by ΔR between 0.2 and 0.4 from any remaining jet are removed.

Muon candidates are formed by combining information from the muon spectrometer and inner tracking detectors as described in Ref. [103] and are required to have $p_{\mathrm{T}} > 10\,\mathrm{GeV}$ and $|\eta| < 2.5$. Jets with

$p_{\mathrm{T}} > 20\,\mathrm{GeV}$ and less than three tracks with $p_T > 0.4\,\mathrm{GeV}$ associated with them are discarded if their separation ΔR from an identified muon is less than 0.4. The muon is discarded if it is matched to a jet that has at least three tracks associated with it.

6.3.3 Missing Transverse Momentum

The E_T^{miss} is reconstructed using all energy deposits in the calorimeter up to pseudorapidity $|\eta| = 4.9$. Clusters associated with either electrons or photons with $p_T > 20\,\mathrm{GeV}$ and those associated with jets with $p_T > 20\,\mathrm{GeV}$ make use of the corresponding calibrations for these objects. Softer jets and clusters not associated with these objects are calibrated using tracking information [105]. As discussed below, in this analysis the E_T^{miss} is not corrected for the presence of muons in the final state.

6.4 Signal Region Event Selection

The following selection criteria, summarized in Table 6.2, define the signal region.

- Events are required to have a reconstructed primary vertex for the interaction with at least two associated tracks with $p_T > 0.4\,\mathrm{GeV}$ and location consistent with a primary collision. When more than one such vertex is found, the vertex with the largest summed p_T^2 of the associated tracks is chosen.

- Events are required to have $E_T^{\mathrm{miss}} > 250\,\mathrm{GeV}$. The analysis selects events with a leading (highest p_T) jet with $p_T > 250\,\mathrm{GeV}$ and $|\eta| < 2.4$ in the final state. A maximum of four jets with $p_T > 30\,\mathrm{GeV}$ and $|\eta| < 2.8$ are allowed. A separation in the azimuthal plane of $\Delta\phi(\mathrm{jet}, E_T^{\mathrm{miss}}) > 0.4$ between the missing transverse momentum direction and each selected jet is required. This cut reduces the multijet background contribution where the large E_T^{miss} originates mainly from jet energy mismeasurement.

- Events are rejected if they contain any jet consistent with non–collision background. Jet quality selection criteria [106] involve quantities such as the pulse shape of the energy depositions in the cells of the calorimeters, electromagnetic fraction in the calorimeter, calorimeter sampling fraction,

or charged-particle fraction, as described in Section 5.2. The Loose criteria are applied to all jets with $p_T > 20\,\text{GeV}$ and $|\eta| < 2.8$, dealing efficiently with coherent noise and electronic noise bursts in the calorimeter producing anomalous energy depositions [107]. Non-collision backgrounds are further suppressed by applying the Tight selection criteria to the leading jet: the ratio of the jet charged-particle fraction to the calorimeter sampling fraction, $f_{\text{ch}}/f_{\text{max}}$, is required to be larger than 0.1. These requirements have a negligible effect on the signal efficiency, as shown in Table 6.3.

- Events with identified muons with $p_T > 10\,\text{GeV}$ or electrons with $p_T > 20\,\text{GeV}$ in the final state are vetoed.

This monojet signal region is further subdivided into inclusive and exclusive signal regions defined with increasing E_T^{miss} thresholds from 250 GeV to 700 GeV, shown in Table 6.2. The effect of these cuts on the expected yield of a representative WIMP sample is shown in Table 6.3.

Selection criteria							
Primary vertex $E_T^{\text{miss}} > 250\,\text{GeV}$ Leading jet with $p_T > 250\,\text{GeV}$ and $\|\eta\| < 2.4$ At most four jets with $p_T > 30\,\text{GeV}$ and $\|\eta\| < 2.8$ $\Delta\phi(\text{jet}, p_T^{\text{miss}}) > 0.4$ Jet quality requirements No identified muons with $p_T > 10\,\text{GeV}$ or electrons with $p_T > 20\,\text{GeV}$							
Inclusive signal region E_T^{miss} (GeV)	> 250	> 300	> 350	> 400	> 500	> 600	> 700
Exclusive signal region E_T^{miss} (GeV)	250–300	300–350	350–400	400–500	500–600	600–700	700–∞

Table 6.2: Signal region event selection criteria applied.

SR	Cut		DM
Pre-Selection	Total Evts	3719	100%
	Trigger	3529	95%
	Event Cleaning	3529	95%
	Bad jet veto	3517	95%
	Electron veto	3516	95%
	Muon veto	3514	95%
	$N_{\text{jets}} \leq 4$	3390	91%
	$\Delta\phi(\text{jet}, \vec{p}_T^{\text{miss}}) > 0.4$	3220	87%
	Leading jet quality requirements	3168	85%
	Leading jet with $p_{\text{T}} > 250$ GeV and $\lvert\eta\rvert < 2.4$	1039	28%
	missing transverse momentum > 250 GeV	958	26%
Signal Region	250 GeV $< E_T^{\text{miss}} <$ 300 GeV	188	5.0%
	300 GeV $< E_T^{\text{miss}} <$ 350 GeV	194	5.2%
	350 GeV $< E_T^{\text{miss}} <$ 400 GeV	153	4.1%
	400 GeV $< E_T^{\text{miss}} <$ 500 GeV	196	5.3%
	500 GeV $< E_T^{\text{miss}} <$ 600 GeV	106	2.9%
	600 GeV $< E_T^{\text{miss}} <$ 700 GeV	54	1.5%
	$E_T^{\text{miss}} > 700$ GeV	68	1.8%

Table 6.3: Signal region selection cut flow for a simplified axial-vector model ($m_\chi = 150$ GeV, $m_A = 1$ TeV). The number of signal events corresponds to the expectations for a total integrated luminosity of 3.2 fb^{-1}. For each cut level the expected events and acceptance at reconstructed level are given.

7

Background Estimation

Searching for an excess of events in the monojet topology requires a detailed understanding of monojet background processes. The principal background processes are $Z \to \nu\nu$ + jets, which is irreducible, and $W \to \ell\nu$ + jets ($\ell = e, \mu, \tau$), which can manifest as monojet events when the e or μ fail reconstruction or identification, or the τ decays hadronically. Understanding the W and Z boson p_T spectrum is necessary to constrain the E_T^{miss} in monojet events. The W + jets, $Z \to \nu\nu$ + jets, $Z \to \tau\tau$ + jets, and $Z \to \mu\mu$ + jets backgrounds are estimated using MC samples normalized with data in selected control regions. The normalization factors are extracted simultaneously using a global fit that includes systematic uncertainties to properly take into account correlations.

Other standard model background processes include $Z \to ee$ + jets, $t\bar{t}$, single-top, and diboson (WW, WZ, ZZ) processes, and are determined using MC simulated samples. Contributions from top production associated with additional vector bosons ($t\bar{t} + W$, $t\bar{t} + Z$, or $t + Z + q/b$ processes) are negligible.

Multijet events can be reconstructed with fake E_T^{miss} and enter the signal region selection. Additionally,

the topology of non-collision background processes is a jet and E_T^{miss}, and will dominate the signal region in the absence of strict jet quality criteria. The contributions from both of these processes are estimated using data–driven techniques.

The methodology and the samples used for estimating the background are summarized in Table 7.1. In the following subsections, details of the definition of the W/Z + jets control regions and of the data-driven determination of the multijet and beam-induced backgrounds are given. This is followed by a description of the background fit strategy.

Background process	Method	Scale Factor	Control Region
$Z \to \nu\nu$ + jets	MC and control samples in data	k_1	–
$W \to e\nu$ + jets	MC and control samples in data	k_2	1–electron
$W \to \tau\nu$ + jets	MC and control samples in data	k_2	1–electron
$W \to \mu\nu$ + jets	MC and control samples in data	k_1	1–muon
$Z \to \mu\mu$ + jets	MC and control samples in data	k_3	2–muon
$Z \to \tau\tau$ + jets	MC and control samples in data	k_2	1–electron
$Z \to ee$ + jets	MC only		
$t\bar{t}$, single top	MC only		
Diboson	MC only		
Multijets	data-driven		
Non-collision	data-driven		

Table 7.1: Summary of the methods and control samples used to constrain the different background contributions in the signal regions.

7.1 W/Z + jets Background and Control Regions

Three control regions are used to constrain the W/Z + jets background processes. They are constructed to be kinematically similar to the signal region, enriched in background processes, insensitive to any dark matter production, and orthogonal to the signal region selection. This is achieved by inverting the signal region lepton veto to require the presence of one muon, one electron, or two muons respectively for each control region.

In the course of the analysis, an additional 2—electron control region was studied for constraining the

$Z \to ee$+jets and $Z \to \nu\nu$+jets background contributions. This control region provided an insignificant improvement in reducing the total background uncertainty and is not used in the full background estimation scheme.

7.1.1 1–muon Control Region

The 1-muon control region is constructed to be enriched in $W \to \mu\nu$ + jets events. Although the full W mass cannot be reconstructed in $W \to \mu\nu$ events, the transverse mass of the muon and neutrino can be used to select for events containing a W boson:

$$m_T^2 = 2p_T^\mu \cdot p_T^{\text{miss}}\big(1 - \cos\Delta\phi(p_T^\mu, p_T^{\text{miss}})\big) \tag{7.1}$$

where p_T^μ is the muon transverse momentum and p_T^{miss} is the invisible transverse momentum. In a pure sample of perfectly reconstructed $W \to \mu\nu$ events, $p_T^{\text{miss}} = p_T^\nu$. A requirement of $30 < m_T < 100$ GeV is applied to ensure that the muon p_T and p_T^{miss} are consistent with a W boson. The muon is treated as invisible in the calculation of missing transverse momentum so that the E_T^{miss} spectrum shown in Figure 7.1 resembles the W boson p_T.

This control region strongly constrains the scale factor k_1 which normalizes the $W \to \mu\nu$ + jets and $Z \to \nu\nu$ + jets processes. As no control region can be constructed for $Z \to \nu\nu$, the normalization of this background needs to come from other, similar processes. Because $W \to \mu\nu$ events occur at five times the rate of $Z \to \mu\mu$ events, the $W \to \mu\nu$ spectrum is used to normalize $Z \to \nu\nu$ instead of a $Z \to \ell\ell$ sample.

The use of a W–enriched control sample to constrain the normalization of the $Z \to \nu\nu$+jets process translates into a reduced uncertainty in the estimation of the main irreducible background contribution, due to a partial cancellation of systematic uncertainties and the statistical power of the $W \to \mu\nu$+jets control sample in data relative to the $Z \to \mu\mu$+jets control sample. A full discussion of this uncertainty is given in Section 7.4.1.

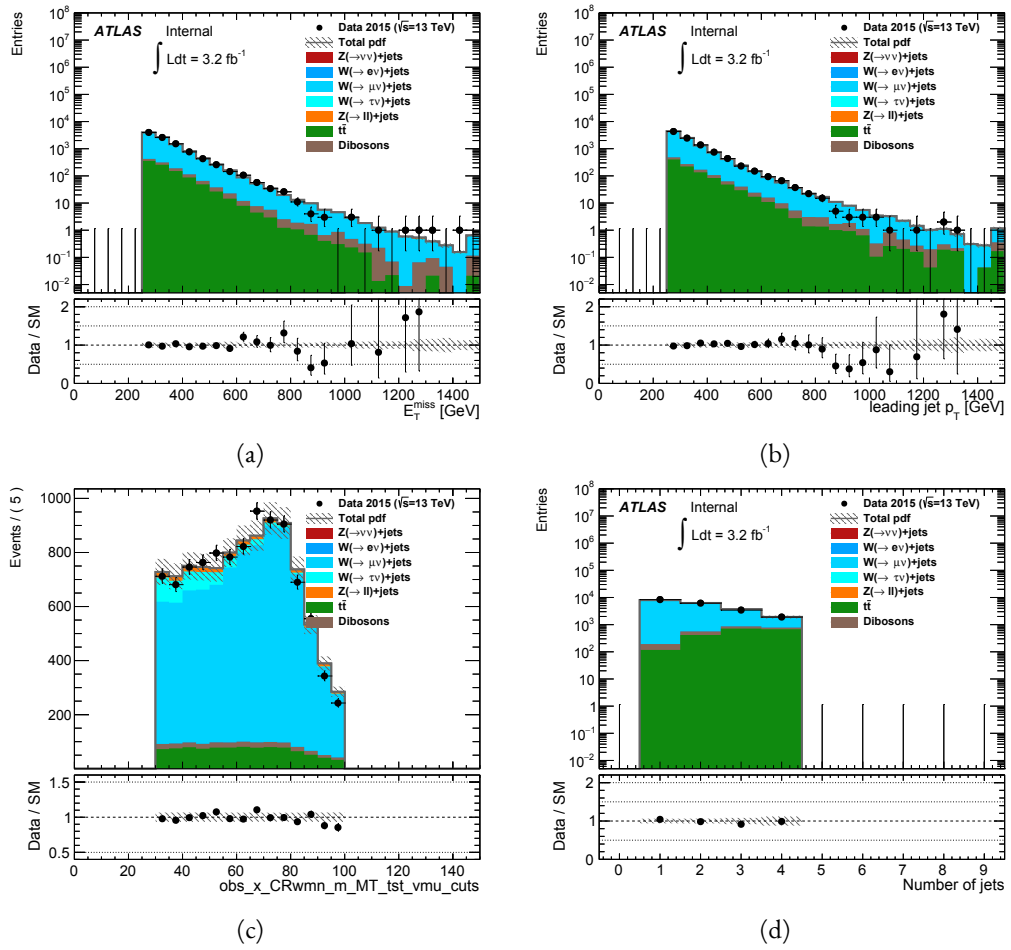


Figure 7.1: Distributions of the measured E_T^{miss} (a), leading-jet p_{T} (b), muon m_T (c), and jet multiplicity (d) in the 1–muon control region for the $E_T^{\text{miss}} > 250$ GeV selection, compared to the background predictions before the global fit. The error bands in the ratios include the statistical and experimental uncertainties in the background predictions. The contributions from multijets and non-collision backgrounds are negligible and are not shown in the figures.

Inclusive Selection	> 250	> 300	> 350	> 400	> 500	> 600	> 700
Observed events (3.2 fb^{-1})	10481	6279	3538	1939	677	261	95
SM prediction (post-fit)	10480 ± 100	6279 ± 79	3538 ± 60	1939 ± 44	677 ± 26	261 ± 16	95 ± 10
SM prediction (pre-fit)	10500 ± 710	6350 ± 460	3560 ± 280	2010 ± 160	700 ± 57	256 ± 23	106 ± 9
Exclusive Selection	[250–300]	[300–350]	[350–400]	[400–500]	[500–600]	[600–700]	
Observed events (3.2 fb^{-1})	4202	2741	1599	1262	416	166	
SM prediction (post-fit)	4202 ± 65	2741 ± 52	1599 ± 40	1262 ± 36	416 ± 20	166 ± 13	
SM prediction (pre-fit)	4140 ± 260	2800 ± 190	1540 ± 120	1310 ± 100	444 ± 35	150 ± 14	

Table 7.2: Data and SM background prediction, before and after the fit, in the 1–muon control region for the different selections. For the SM predictions both the statistical and systematic uncertainties are included.

7.1.2 1–electron Control Region

The 1–electron control region is constructed to be enriched in $W \to e\nu$+jets and $W \to \tau\nu$+jets background processes. The electron is visible in the missing transverse momentum calculation so the E_T^{miss} spectrum in Figure 7.2 resembles the ν p_T rather than the W boson p_T, which gives a better suppression of the multijet background in this control region.

This control region strongly constraining the scale factor k_2 which normalizes the $W \to e\nu$+jets, $W \to \tau\nu$+jets, and $Z \to \tau\tau$+jets background processes. No dedicated $W \to \tau\nu$+jets control region is used because the τ lepton in the $W \to \tau\nu$+jets background process mainly decays hadronically, resembling the signal region event topology. Instead, the normalization is taken from the leptonic tau decay in the 1–electron control region, which is kinematically similar to the $W \to e\nu$+jets sample. A small $Z \to \tau\tau$+jets background contribution is also constrained using the $W \to e\nu$+jets control sample. Uncertainties related to the difference between W+jets and Z+jets final states, leading to potential differences in event kinematics and selection acceptances and efficiencies, are discussed in Section 7.4.1.

Inclusive Selection	> 250	> 300	> 350	> 400	> 500	> 600	> 700
Observed events (3.2 fb^{-1})	3559	1866	992	532	183	72	32
SM prediction (post-fit)	3559 ± 60	1866 ± 43	992 ± 32	532 ± 23	183 ± 14	72 ± 8	32 ± 6
SM prediction (pre-fit)	3990 ± 320	2110 ± 170	1142 ± 94	654 ± 54	216 ± 19	85 ± 8	34 ± 3
Exclusive Selection	**[250–300]**	**[300–350]**	**[350–400]**	**[400–500]**	**[500–600]**	**[600–700]**	
Observed events (3.2 fb^{-1})	1693	874	460	349	111	40	
SM prediction (post-fit)	1693 ± 41	874 ± 30	460 ± 21	349 ± 19	111 ± 11	40 ± 6	
SM prediction (pre-fit)	1880 ± 150	971 ± 79	488 ± 40	439 ± 36	131 ± 12	50 ± 5	

Table 7.3: Data and SM background prediction, before and after the fit, in the 1–electron control region for the different selections. For the SM predictions both the statistical and systematic uncertainties are included.

7.1.3 2-muon Control Region

Finally, the 2–muon control region is used to constrain the $Z \to \mu\mu$+jets background contribution. An additional cut is applied to the dimuon invariant mass $66 < m_{\mu\mu} < 116$ GeV, and both muons are treated as invisible particles so that the E_T^{miss} spectrum shown in Figure 7.3 resembles the Z boson p_T.

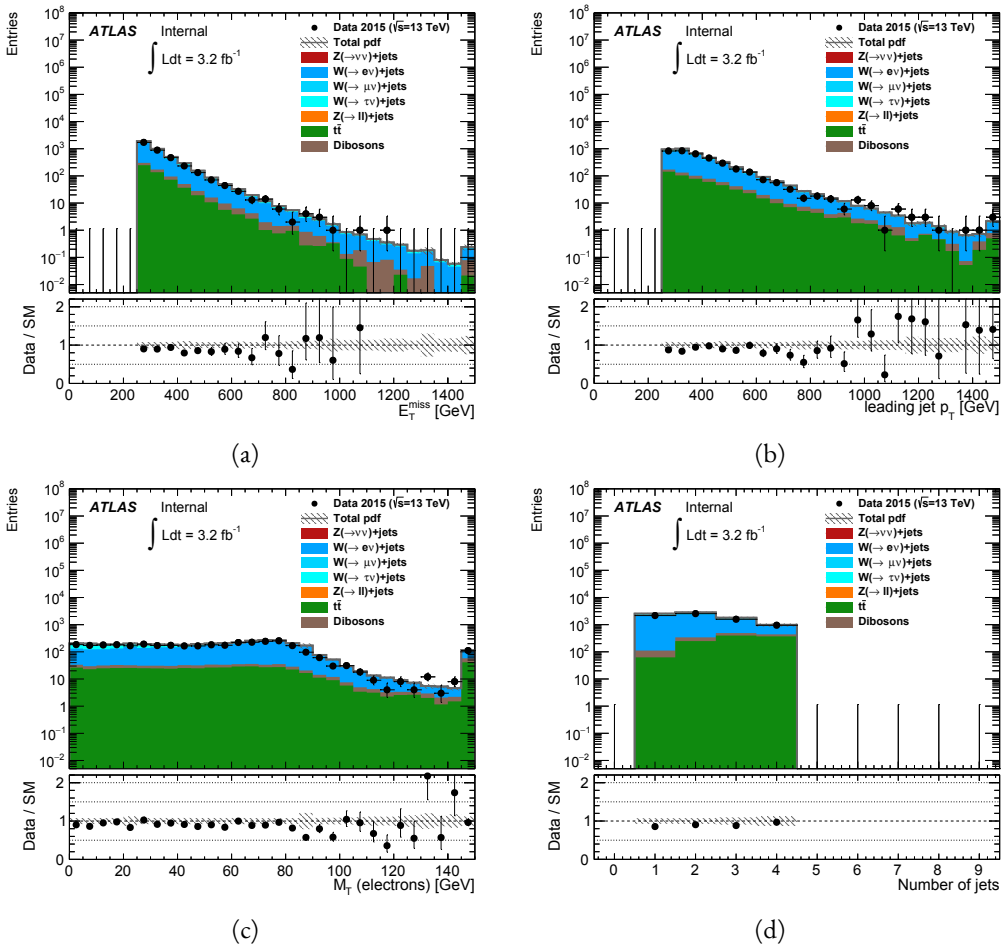


Figure 7.2: Distributions of the measured E_T^{miss} (a), leading-jet p_{T} (b), electron m_T (c), and jet multiplicity (d) in the 1–electron control region for the $E_T^{\text{miss}} > 250$ GeV selection, compared to the background predictions before the global fit. The error bands in the ratios include the statistical and experimental uncertainties in the background predictions. The contributions from multijets and non-collision backgrounds are negligible and are not shown in the figures.

Inclusive Selection	> 250	> 300	> 350	> 400	> 500	> 600	> 700
Observed events (3.2 fb^{-1})	1488	877	505	293	100	33	15
SM prediction (post-fit)	1488 ± 39	877 ± 30	505 ± 22	293 ± 17	100 ± 10	33 ± 6	15 ± 4
SM prediction (pre-fit)	1520 ± 98	910 ± 59	487 ± 34	271 ± 19	89 ± 7	32 ± 3	13 ± 1
Exclusive Selection	[250–300]	[300–350]	[350–400]	[400–500]	[500–600]	[600–700]	
Observed events (3.2 fb^{-1})	611	372	212	193	67	18	
SM prediction (post-fit)	611 ± 25	372 ± 19	212 ± 15	193 ± 14	67 ± 8	18 ± 4	
SM prediction (pre-fit)	610 ± 42	422 ± 36	217 ± 15	182 ± 13	57 ± 4	19 ± 2	

Table 7.4: Data and SM background prediction, before and after the fit, in the 2–muon control region for the different selections. For the SM predictions both the statistical and systematic uncertainties are included.

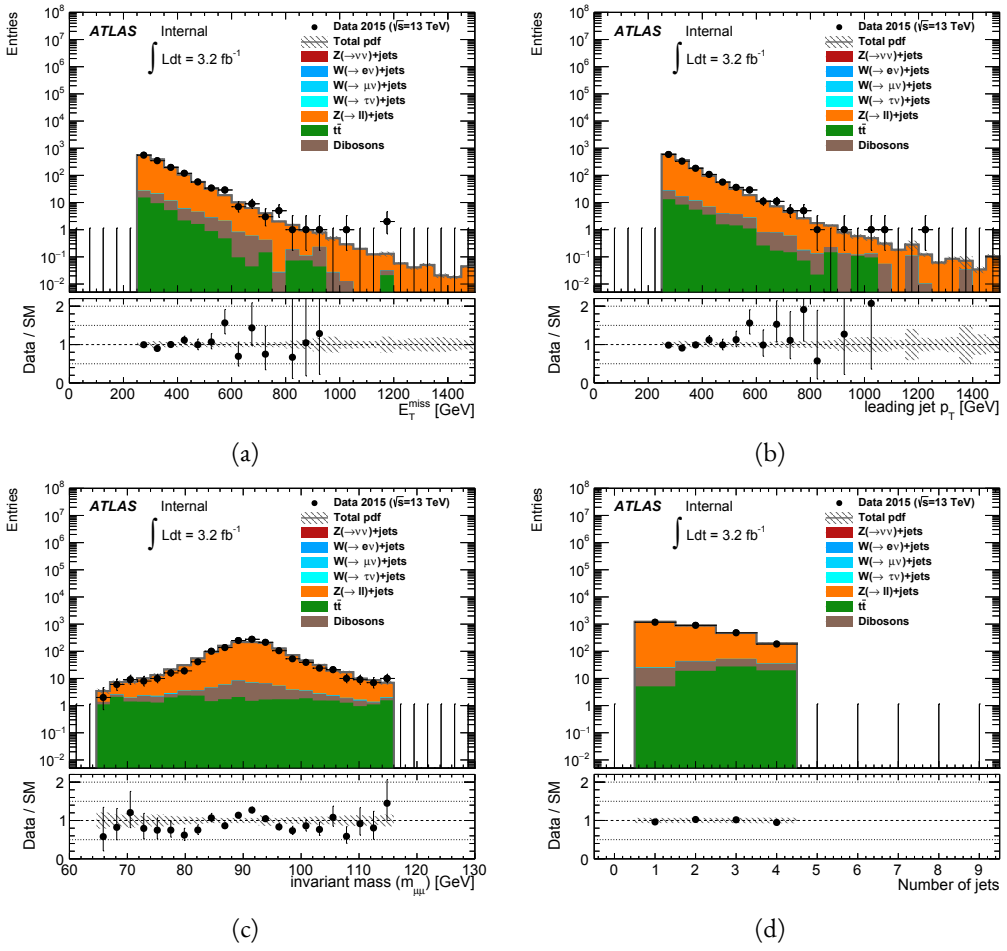


Figure 7.3: Distributions of the measured E_T^{miss} (a), leading-jet p_{T} (b), dimuon mass (c), and jet multiplicity (d) in the 2–muon control region for the $E_T^{\text{miss}} > 250$ GeV selection, compared to the background predictions before the global fit. The error bands in the ratios include the statistical and experimental uncertainties in the background predictions. The contributions from multijets and non-collision backgrounds are negligible and are not shown in the figures. The shape difference observed in the dimuon invariant mass between data and simulation does not have an impact in this analysis.

7.2 Non–Collision Background

A high–p_T jet recoiling against missing transverse momentum is also the event signature of non–collision background (NCB) jets. Without additional jet selection criteria, non-collision background dominates the signal region at $\mathcal{O}(100)$ the rate of Standard Model background processes, as shown in Figure 7.4. Tight jet cleaning criteria have been deployed to efficiently suppress the level of NCB in the monojet signal region, suppressing non-collision rates by $\mathcal{O}(10^3)$.

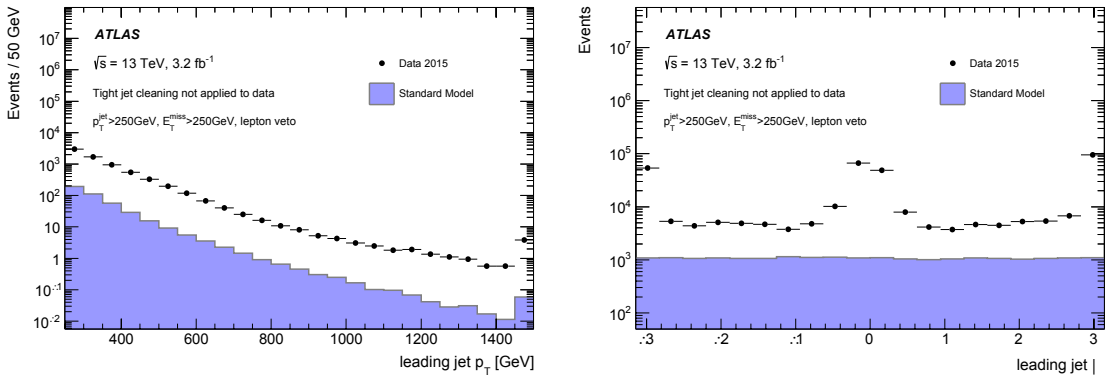


Figure 7.4: The leading jet p_T (left) and ϕ (right) distributions of the data events passing the signal region selection without the tight cleaning criteria applied on the leading jet. The ϕ distribution shows a typical azimuthal structure of beam-induced backgrounds. The Standard Model background indicated in the plots corresponds to the estimates obtained for the analysis signal region, including tight jet quality requirements. The jet selection inefficiency of the cleaning selection is $\mathcal{O}(1\%)$, which is negligible compared to the observed excess in data. This demonstrates the necessity of a strong non-collision background suppression for this analysis.

The residual NCB in the signal region is estimated using a data-driven method. A set of beam–induced–background (BIB) tagging methods have been developed [108] which match[1] calorimeter clusters in the LAr or Tile barrels with $E_T > 10$ GeV to a CSC or MDT segment which is nearly parallel to the beam pipe. The *two–sided no–time method* is used: a match between a calorimeter cluster and a muon segment on both the A and C sides of the detector is required, and no requirement on jet timing is applied. Extensive studies conducted using 8 TeV data showed that the typical efficiency of this BIB tagger was around 15%, with a mistag rate (probability of tagging a good jet as a fake jet) of less than 10^{-5}.

This BIB tagger is used for the evaluation of the residual NCB contribution in the signal region:

[1] Matching happens in terms of the azimuthal angular distance and of the relative radial distance between cluster and segment.

1. A sample enriched in BIB can be constructed by looking at events in the signal region in which the leading jet fails the tight cleaning criteria.

2. The BIB tagging efficiency is then assessed as the ratio between the number of events tagged as BIB and the overall number of events in this BIB–enriched region:

$$\epsilon_{\text{BIB tag}} = \frac{N_{\text{BIB tag}}^{\text{NCB region}}}{N^{\text{NCB region}}};$$

3. The NCB yield in the SR is then estimated as the ratio between the number of SR events which are tagged as BIB and the BIB tagging efficiency:

$$N_{\text{NCB}}^{\text{SR}} = \frac{N_{\text{BIB tag}}^{\text{SR}}}{\epsilon_{\text{BIB tag}}};$$

4. The BIB mistag rate is cross-checked as the fraction of events in the signal region which are flagged as BIB by the tagger but pass the tight cleaning criteria:

$$r_{\text{mistag}} = \frac{N_{\text{BIB tag}}^{\text{SR}}}{N_{\text{BIB tag}}^{\text{SR without tight}}}$$

The BIB tagger information was effectively introduced on September 20, 2015 and available in the last 2.7 fb^{-1} of data collected in 2015. Using this subset of data, one obtains the numbers shown in Table 7.5.

	$E_T^{\text{miss}} > 250$ GeV	$E_T^{\text{miss}} > 600$ GeV
$N_{\text{BIB tag}}^{\text{SR}}$	24	0
$N_{\text{BIB tag}}^{\text{NCB region}}$	69653	2175
$N^{\text{NCB region}}$	275816	8521
$\epsilon_{\text{BIB tag}}$	$25 \pm 0.2\%$	$25 \pm 1\%$
r_{mistag}	$0.03 \pm 0.4\%$	0%

Table 7.5: Evaluation of the BIB tagger efficiency and mistag rate in the last 2.7 fb^{-1} of data collected in 2015. $\epsilon_{\text{BIB tag}}$ is evaluated using the inverted jet cleaning control region defined above. Errors shown are statistical uncertainties.

To extrapolate the total amount of NCB in the signal region for the entire 3.2 fb^{-1} of data, one must determine the amount of fake jets in runs in which the BIB tagger was not available.[2] The total number of events in the BIB–enriched region for the entire dataset is shown in Table 7.6.

	$E_T^{\text{miss}} > 250$ GeV	$E_T^{\text{miss}} > 600$ GeV
$N^{\text{NCB region}}$	324460	9999

Table 7.6: Number of fake jet events in the full 3.2 fb^{-1} of data collected in 2015.

Then, assuming that the BIB tagging efficiency is constant across the data collection period, the total number of events flagged as BIB by the tagger can be determined by rescaling $N^{\text{SR}}_{\text{BIB tag}}$ to match the fake jet rate for the entire dataset. Therefore, the total amount of non–collision background in the signal region can be calculated as:

$$N^{\text{SR}}_{\text{NCB}} = \left(\frac{N^{\text{NCB region}}_{\text{3.2 fb}^{-1}}}{N^{\text{NCB region}}_{\text{2.7 fb}^{-1}}} \right) \frac{N^{\text{SR}}_{\text{BIB tag}}}{\epsilon_{\text{BIB tag}}}$$

The amount of non–collision background is shown in Table 7.7. The BIB tagger efficiency can vary between 22% and 45% when evaluated using different BIB-enriched regions, as discussed in Appendix B. Therefore, a conservative 100% systematic uncertanty is applied to the total amount of non–collision background in the signal region.

7.2.1 Jet Cleaning Performance

The non–collision–background rejection power of the Tight jet cleaning criteria is evaluated on a sample of BIB–tagged events in the signal region for different E_T^{miss} regimes in Table 7.8. Only sub-percent non-collision backgrounds remain in the signal region after applying the cleaning criteria.

[2] This extrapolation will not be necessary when using the reprocessed data since the tagger will be available for the whole 2015 dataset there.

Region	N^{NCB}
$E_T^{\text{miss}} > 250$ GeV	112 ± 23
$250 < E_T^{\text{miss}} < 300$ GeV	61 ± 17
$300 < E_T^{\text{miss}} < 350$ GeV	23 ± 10
$350 < E_T^{\text{miss}} < 400$ GeV	19 ± 9
$400 < E_T^{\text{miss}} < 500$ GeV	9 ± 7
$E_T^{\text{miss}} > 500$ GeV	0

Table 7.7: Total amount of non–collision background in the specified regions. Errors shown are statistical uncertainties.

	$E_T^{\text{miss}} > 250$ GeV	$E_T^{\text{miss}} > 600$ GeV
$N_{\text{BIB tag}}^{\text{SR w/o cleaning}}$ in first 2.7 fb^{-1}of data	69677	2175
Total estimated NCB w/o cleaning	324572 ± 3	9999 ± 3
$N_{\text{BIB tag}}^{\text{SR with cleaning}}$ in first 2.7 fb^{-1}of data	24	0
Total estimated NCB with cleaning	113 ± 2	0
% Remaining NCB	$0.03 \pm 0.3\%$	0

Table 7.8: Amount of NCB in the signal region with and without applying the Tight cleaning criteria to the leading jet. Errors shown are statistical uncertainties.

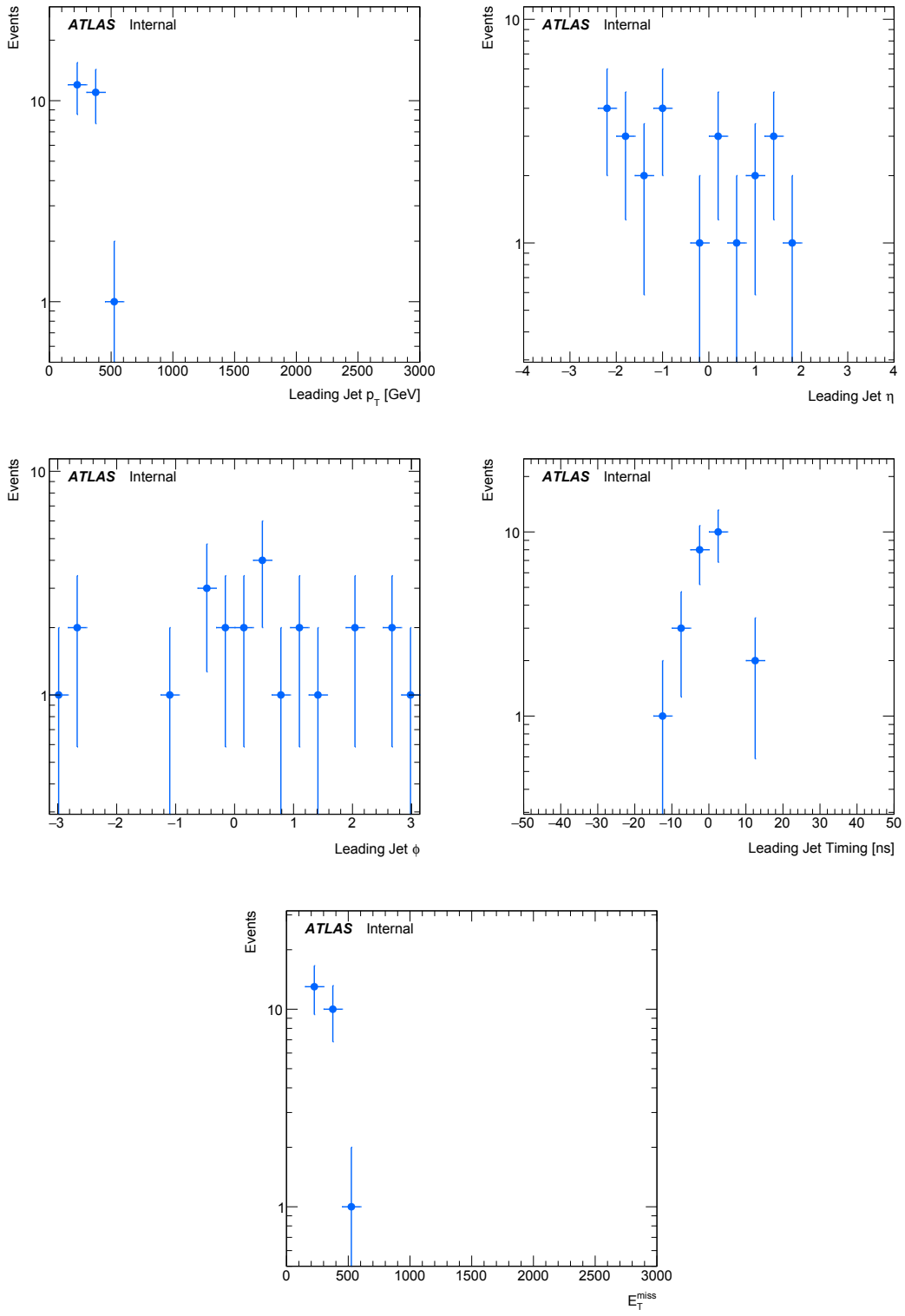
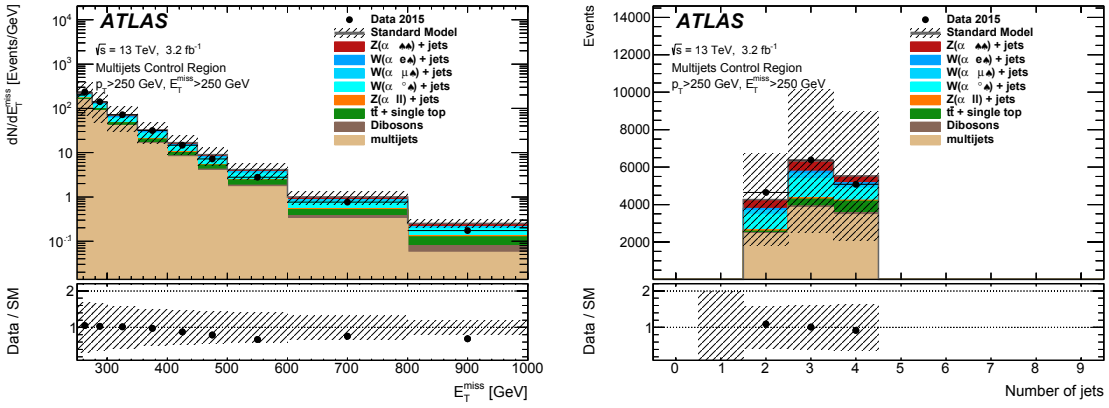


Figure 7.5: Selected distributions for the events in the signal region $E_T^{\text{miss}} > 250$ GeV that are tagged as non–collision background, yet have leading jets that pass the Tight jet cleaning criteria.

7.3 Multijet Background

The multijet background with large E_T^{miss} mainly originates from the misreconstruction of the energy of a jet in the calorimeter and to a lesser extent is due to the presence of neutrinos in the final state from heavy-flavor hadron decays. In this analysis, the multijet background is determined from data, using the jet smearing method as described in Reference [109], which relies on the assumption that the E_T^{miss} of multijet events is dominated by fluctuations in the jet response in the detector which can be measured in the data. The jet smearing method requires the normalization of the smeared data in a multijet-enriched control region. This region is defined with similar E_T^{miss} and leading jet p_T cuts as in the signal region definition, but inverting the $\Delta\phi(\text{jet}, \vec{p}_T^{\text{miss}})$ cut, requiring it to be less than 0.4. Distributions for this selection are shown in Figure 7.6. The multijet background estimation includes both the statistical and a 100% systematic uncertainty. For the $E_T^{\text{miss}} > 250$ GeV and $250 < E_T^{\text{miss}} < 300$ GeV selections, the multijet background constitutes about 0.5% of the total background, and is negligible for the other signal regions.



(a) (b)

Figure 7.6: Measured distribution of the E_T^{miss} (left) and jet multiplicity (right) in the multijet control region for the $E_T^{\text{miss}} > 250$ GeV selection compared to the expected background. The error bands in the ratio shown in the lower panel include both the statistical and systematic uncertainties in the background expectations. The multijets background estimation includes both the statistical and a 100% systematic uncertainty.

7.4 Experimental Systematics

Experimental uncertainties effect expected event yields, ratios, and scale factors in the analysis, and must be accounted for in the final limit calculation. Uncertainties on reconstructed objects such as jets or leptons can arise from the energy/momentum scale or efficiencies of object reconstruction, identification, and selection. Overall uncertainties on the event selection efficiency from the trigger and luminosity measurement are also included. As described in Section 7.6, the following list of nuisance parameters are used to model the impact of experimental systematic uncertainties on expected background and signal event yields in different E_T^{miss} bins:

`Luminosity` A 5% uncertainty has been applied to all MC event yields, to account for the uncertainty on the knowledge of the integrated luminosity measured in data which is used for the MC normalization.

`Trigger Efficiency` No uncertainty related to the trigger efficiency is considered in the signal regions because the efficiency plateau for the `HLT_xe70` trigger is reached at the missing transverse momentum values below 250 GeV already.

`EG_RESOLUTION_ALL` Accounts for the uncertainty on the electron/photon resolution.

`EG_SCALE_ALL` Accounts for the uncertainty on the electron/photon energy scale.

`EL_EFF_ID_TotalCorrUncertainty` Accounts for the uncertainty on the electron identification efficiency scale factors applied to MC.

`EL_EFF_Reco_TotalCorrUncertainty` Accounts for the uncertainty on the electron reconstruction efficiency scale factors applied to MC.

`EL_EFF_Iso_TotalCorrUncertainty` Accounts for the uncertainty on the electron isolation efficiency scale factors applied to MC.

`JET_GroupedNP_i` ($i = 1 \ldots 3$) Accounts for the uncertainty on the jet energy scale (JES) from in–situ analyses.

MET_SoftTrk_ResoPara Accounts for the missing transverse momentum track soft term resolution uncertainty (soft term projection parallel to the hadronic recoil system p_T).

MET_SoftTrk_ResoPerp Accounts for the missing transverse momentum track soft term resolution uncertainty (soft term projection perpendicular to the hadronic recoil system p_T).

MET_SoftTrk_Scale Accounts for the missing transverse momentum track soft term scale uncertainty.

MUONS_ID and **MUONS_MS** Account for the impact of muon identification efficiency scale factor uncertainties.

MUONS_SCALE Accounts for the impact of muon momentum scale uncertainties.

MUON_EFF_STAT Accounts for the statistical component of muon identification efficiency scale factor uncertainties.

MUON_EFF_SYS Accounts for the systematic component of muon identification efficiency scale factor uncertainties.

Uncertainties in the absolute jet and missing transverse momentum energy scales and resolutions [102] translate into an uncertainty in the total background which varies between $\pm 0.5\%$ for the low–E_T^{miss} signal region bin and $\pm 1.6\%$ for the high–E_T^{miss} signal region bin. Uncertainties related to jet quality requirements, pileup dependance, and corrections to the jet p_{T} and E_T^{miss} introduce a $\pm 0.2\%$ to $\pm 0.9\%$ uncertainty in the background predictions. Uncertainties in the simulated lepton identification and reconstruction efficiencies, energy/momentum scale and resolution translate into an uncertainty in the total background which varies between $\pm 0.1\%$ and $\pm 1.4\%$ for the low–E_T^{miss} signal region bin and between $\pm 0.1\%$ and $\pm 2.6\%$ for the high–E_T^{miss} signal region bin, respectively. Uncertainties on the luminosity are strongly constrained by the background fit and are negligible in the signal region.

7.4.1 `WZtransfer` Uncertainty

A `WZtransfer` uncertainty is assigned to the $Z \to \nu\nu$ prediction in the signal region to account for the fact that its normalization is primarily derived from the $W \to \mu\nu$ yield in the 1–muon control region, as

described in Section 7.6.

Monte Carlo modeling differences between the missing transverse momentum in $Z \to \nu\nu$ and $W \to \mu\nu$ are one source of uncertainty. Figure 7.7 shows several observables used to define the analysis are compared between events from $Z \to \nu\nu$ in the signal region ($E_T^{\text{miss}} > 250$ GeV) and events from $W \to \mu\nu$ in the single muon control region (without the invariant mass cut). The MC modeling differences are on the order of 2-3%.

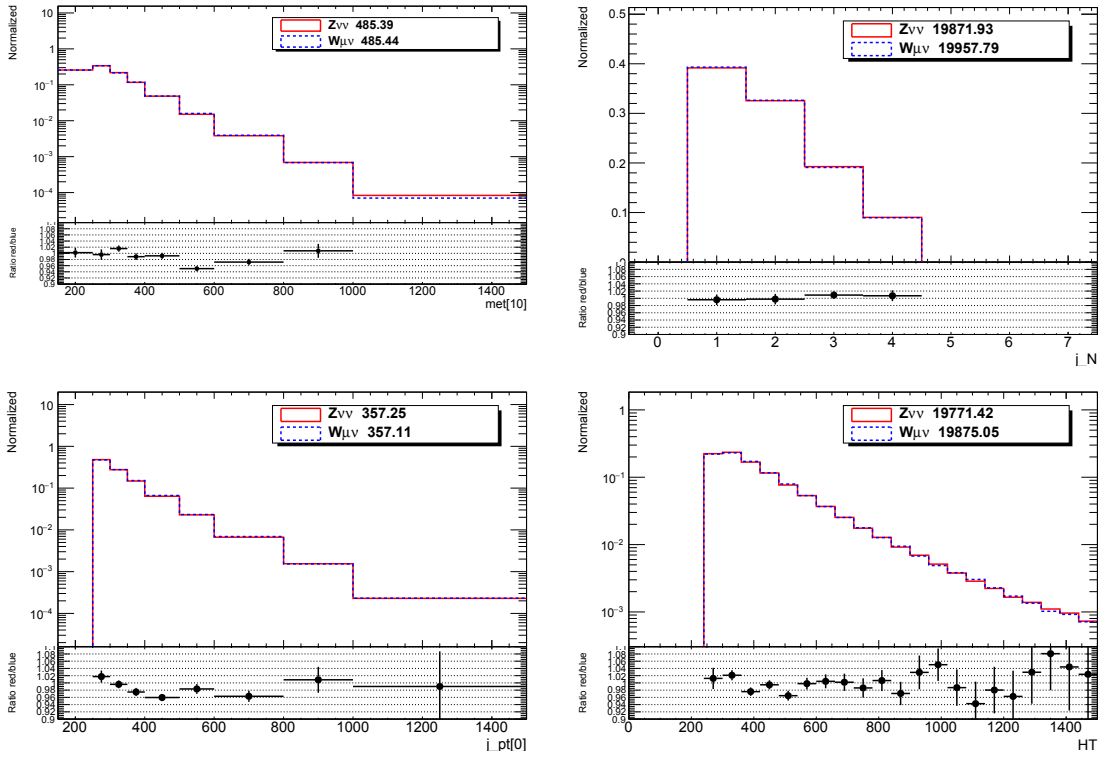


Figure 7.7: Comparison of the truth level quantities E_T^{miss}, jet multiplicity, leading jet p_T and H_{T} in the W and Z Monte Carlo samples.

The effect from NLO electroweak corrections on the W+jets to Z+jets ratio is also included [110–112]. Dedicated parton-level calculations are performed with the same E_T^{miss} and leading-jet-p_T requirements as in the E_T^{miss}–binned signal regions. The studies suggest an effect on the W+jets to Z+jets ratio which varies between about $\pm 1.9\%$ for $E_T^{\text{miss}} > 250$ GeV and $\pm 5.2\%$ for $E_T^{\text{miss}} > 700$ GeV, although the calculations suffer from large uncertainties, mainly due to limited knowledge of the photon PDFs in the

proton. These results are adopted as an additional uncertainty in the $Z \to \nu\nu$+jets and $Z \to \tau\tau$+jets contributions, quoted in Table 7.9.

The final `WZtransfer` uncertainty used for the $Z \to \nu\nu$ prediction in the SR corresponds to the sum in quadrature of the 3% from MC modelling and the corresponding uncertainty from the EW correction. The values used are given in Table 7.9, where numbers are rounded up for brevity and simplicity.

Exclusive bins of E_T^{miss} (GeV)						
[250-300]	[300-350]	[350-400]	[400-500]	[500-600]	[600-700]	[700-∞]
EW correction by theoretical calculations						
$\left(-0.4^{+1.6}_{-0.8}\right)\%$	$\left(0.1^{+1.6}_{-1.0}\right)\%$	$\left(-0.7^{+1.8}_{-1.2}\right)\%$	$\left(0.2^{+1.8}_{-1.4}\right)\%$	$\left(0.4^{+2.1}_{-1.9}\right)\%$	$\left(1.5^{+2.5}_{-2.3}\right)\%$	$\left(1.7^{+2.4}_{-3.5}\right)\%$
Final `WZtransfer` uncertainties						
$\pm 3.5\%$	$\pm 3.5\%$	$\pm 4.0\%$	$\pm 4.0\%$	$\pm 4.0\%$	$\pm 5.0\%$	$\pm 6.0\%$

Table 7.9: LO Z/W electroweak corrections as given by theoretical calculations. The large uncertainties on these estimations are mostly coming from errors in the photon PDFs. Additionally, this table shows final `WZtransfer` uncertainties, combining contributions from the MC modelling and the EW corrections differences in the W+jets and Z+jets production.

7.5 Theoretical Uncertainties

Uncertainties related to the Monte Carlo predicted background yields are estimated for the W/Z+jets, $t\bar{t}$, single-top, and diboson processes.

Uncertainties corresponding to variations of the renormalization, factorization, and parton-shower matching scales and PDFs in the SHERPA W/Z+jets background samples are shown in Table 7.10. These uncertainties translate into a $\pm 1.1\%$ to $\pm 1.3\%$ uncertainty in the total background.

Theoretical uncertainties in the predicted background yields for top-quark-related processes include: uncertainties on the absolute $t\bar{t}$ and single-top production cross sections, variations in the set of parameters that govern the parton showers and the amount of initial- and final-state soft gluon radiation, and

Sample	[250-300]	[300-350]	[350-400]	[400-500]	[500-600]	[600-700]	[700-∞]
$Z \to \nu\nu$	0.51%	0.79%	0.99%	0.39%	0.81%	0.37%	0.61%
$Z \to \ell\ell$	2.73%	3.50%	4.39%	2.42%	3.23%	1.82%	1.08%
$W \to e\nu$	3.72%	1.90%	1.62%	1.21%	2.08%	4.70%	7.22%
$W \to \mu\nu$	0.92%	0.16%	0.33%	0.48%	0.41%	0.33%	1.32%
$W \to \tau\nu$	3.96%	0.95%	1.17%	1.71%	2.38%	4.54%	3.90%

Table 7.10: Final V+jets systematic uncertainties for the different Sherpa samples, as a function of missing transverse momentum [GeV].

uncertainties due to the choice of renormalization and factorization scales and PDFs. This introduces an uncertainty in the total background prediction which varies between $\pm 2.7\%$ and $\pm 3.3\%$.

Uncertainties in the diboson contribution are estimated using different MC generators and translate into an uncertainty in the total background in the range between $\pm 0.05\%$ and $\pm 0.4\%$. A $\pm 100\%$ uncertainty in the multijet and non-collision background estimations is adopted, leading to a $\pm 0.2\%$ uncertainty in the total background for $E_T^{\text{miss}} > 250$ GeV.

Statistical uncertainties related to the data control regions and simulation samples lead to an additional uncertainty in the final background estimates in the signal regions which varies between $\pm 2.5\%$ and $\pm 10\%$.

7.5.1 Signal Sample Uncertainties

The uncertainty on the signal sample yields arises from experimental, theoretical, and Monte Carlo generator-dependent uncertainties. The experimental uncertainties related to the jet and E_T^{miss} scales and resolutions introduce uncertainties in the signal yields which vary between $\pm 1\%$ and $\pm 3\%$. The uncertainty in the integrated luminosity is also included. Aspects of signal sample generation create uncertainties in the signal acceptance. The uncertainty related to the modeling of the initial- and final-state radiation translates into $\pm 20\%$ uncertainty in the acceptance. The choice of different PDF sets results in up to $\pm 20\%$ uncertainty in the acceptance and $\pm 10\%$ uncertainty in the cross section. Varying the renormalization and factorization scales introduces $\pm 5\%$ variations of the cross section and a $\pm 3\%$ change in the acceptance.

7.6 Simultaneous Shape Fit

A simultaneous likelihood fit is performed across the the 1–muon, 1–electron, and 2–muon control regions and signal region in order to normalize and constrain the background estimates. Background-only fits which remain blind to the signal region data yield are performed separately in each of the seven inclusive regions $E_T^{\text{miss}} > 250$ GeV through $E_T^{\text{miss}} > 700$ GeV. This fit is used to set model-independent limits on the total number of events that could be arising from new physics, presented in Section 8.3. In addition, a fit simultaneously using all the exclusive E_T^{miss} regions is performed. In this case, three normalization factors are considered separately in each of the seven exclusive E_T^{miss} regions, for a total of 21 normalization factors. which uses information from the shape of the E_T^{miss} distribution to enhance the sensitivity of the analysis to the presence of new phenomena. This scheme is used to set limits on the cross section for various dark matter simplified models, presented in Section 8.4.

Shape Fit

The simplified shape fit strategy reduces analysis uncertainties arising from discrepancies between data and Monte Carlo predictions of the boson p_T spectrum, while using information about the E_T^{miss} spectrum to improve the analysis sensitivity. For example, in the $\sqrt{s}$ = 8 TeV version of the mono–jet analysis a discrepancy between the expected and observed E_T^{miss} shape was present in the 1–muon control region, as shown in Figure 7.8. Instead of accounting for this discrepancy with an additional systematic uncertainty, the background estimation scheme can be expanded to use multiple normalization factors that each scale a different bin of E_T^{miss}. Additionally, this scheme incorporates shape information into the statistical analysis. Instead of performing a counting experiment for the entire inclusive signal region, in the simplified shape fit a counting experiment in performed in each exclusive bin of the E_T^{miss} spectrum. The seven-bin scheme used in this analysis and shown in Table 6.2 was chosen based on the available luminosity. More bins better exploit shape information, but also suffer from lower statistics.

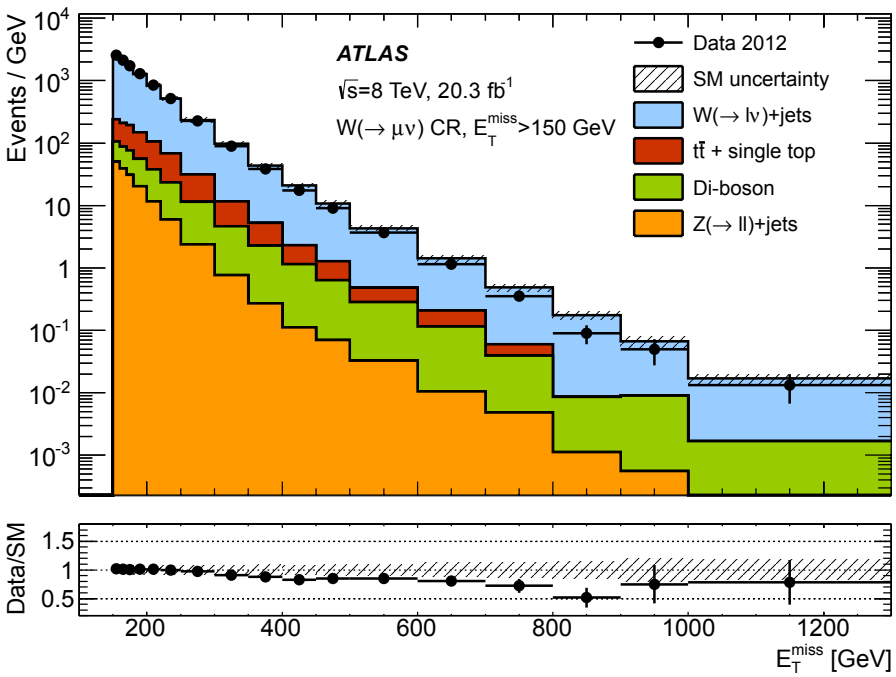


Figure 7.8: Distribution of E_T^{miss} in the 1–muon control region for the 8TeV mono–jet analysis [113], compared with the background expectation. The error bands in the ratios include the statistical and experimental uncertainties on the background expectations. A shape disagreement is observed between the measured and expected distributions. Instead of accounting for this discrepancy with an envelope uncertainty, the background normalization scheme can be expanded to fit to the E_T^{miss} shape.

Analysis Uncertainties

The use of control regions to constrain the normalization of the dominant background contributions from $Z \to \nu\nu$+jets and W+jets significantly reduces the relatively large theoretical and experimental systematic uncertainties, of the order of 20%–40%, associated with purely MC-based background predictions in the signal regions.

To determine the final uncertainty in the total background, the systematic uncertainties described in Section 7.4 are incorporated as nuisance parameters in the fit, as described in Section 7.6.2. This accounts for correlations among systematic variations. The systematic uncertainties are and are assumed to be fully correlated across all the E_T^{miss} bins. The likelihood also takes into account cross-contamination between different background sources in the control regions.

The precise formulation of the statistical treatment is described in the following sections.

7.6.1 Signal Strength

The parameter of interest for discovering or excluding Dark Matter is the production cross section σ, which in this analysis is measured relative to the theoretical prediction for a given WIMP model σ_{theory}. This ratio, μ, is defined as

$$\mu = \frac{\sigma}{\sigma_{\text{theory}}}. \tag{7.2}$$

The statistical analysis of the signal region event yield is a hypothesis test, where the null hypothesis is background-only with no Dark Matter production. All of the likelihoods used in the statistical analysis of the final signal region events are parameterized as a function of μ. μ is a natural variable for hypothesis testing, as $\mu = 0$ corresponds to a background-only hypothesis and $\mu = 1$ corresponds to the predicted cross section for a particular WIMP model.

7.6.2 Likelihood Function

The following section describes the the profile likelihood method [114] used for the statistical analysis of the mono–jet search.

The likelihood function condenses all details of an analysis into a single equation. It is a formula describing the probability of observing the number of events seen in the signal region for some particular value of the signal strength. The observation of events in a signal region is fundamentally a Poisson counting experiment. In a simple single-region counting experiment, the likelihood can be expressed as a Poisson probability of observing N events given a total number of predicted signal and background events:

$$\mathcal{L}(\mu) = P\left(N|\mu S + B\right). \tag{7.3}$$

where P is the Poisson probability density function, N is the total number of observed events, μ is the signal strength scaling the the predicted number of signal events S, and B is the predicted number of background events.

In the mono–jet analysis, the estimated yields for certain background processes entering the signal and control regions are scaled by a normalization factor. This technique allows for more precise background es-

timation by using data as a constraint, reducing the impact of theoretical uncertainties on the background model. The corresponding likelihood is then a function of both the signal strength and background normalization factors:

$$\mathcal{L}(\mu, \theta) = P\left(N|\mu S + \theta B\right) \cdot P\left(N_{\mathrm{CR}}|\theta B_{\mathrm{CR}}\right). \tag{7.4}$$

where θ serves as a "nuisance parameter", or a parameter that is not of primary interest but still enters the likelihood. The second Poisson term enforces that the background normalization be consistent with the number of observed events in data in the control region, N_{CR}.

These two formulations of likelihoods have assumed a single signal region and do not take into account any shape information of potential discriminating variables. However, the mono–jet analysis signal region is subdivided into seven different orthogonal regions based on E_T^{miss}. The counting experiment described above can be performed in each individual region to utilize shape information from the E_T^{miss} distribution. Thus, the total likelihood becomes a product over signal regions and bins of E_T^{miss}. Additionally, more than one background process is normalized in control regions. The following formulation of the likelihood accounts for this by including a product over control regions in the second Poisson term:

$$\mathcal{L}\left(\mu, \boldsymbol{\theta}\right) = \prod_{\text{bins b}} P\left(N_b \middle| \mu S_b + \sum_{\text{bkg k}} \theta_{kb} B_{kb}\right) \prod_{\substack{\text{CRs l} \\ \text{bins b}}} P\left(N_{lb} \middle| \sum_{\text{bkg k}} \theta_{kb} B_{klb}\right) \tag{7.5}$$

where the variable i counts over the different signal regions, b counts over bins of E_T^{miss}, k counts over the backgrounds, and l counts over the control regions, and $\boldsymbol{\theta}$ represents the set of θ_k.

Finally, nuisance parameters for the systematic uncertainties must be included in the likelihood. Each systematic uncertainty ϵ is allowed to affect the expected event yields through an exponential response function of the nuisance parameter $\nu(\theta) = (1 + \epsilon)^{\theta}$. The value of the nuisance parameters for the systematic uncertainty are constrained with a Gaussian term of the form $g(\delta|\theta) = e^{-(\delta-\theta)^2/2}/\sqrt{2\pi}$, where δ is the central value and θ is a nuisance parameter. An additional term is included to account for the statistical uncertainty in the Monte Carlo samples, which adds an additional Poisson term The full

likelihood used in the final statistical analysis then becomes:

$$\mathcal{L}(\mu, \boldsymbol{\theta}) = \prod_{\text{SRs i}} P\left(N_b \middle| \mu S_b \cdot \prod_{\substack{\text{sig.} \\ \text{syst.} \\ r}} \nu_{br}(\theta_r) + \sum_{\text{bkg k}} \theta_{kb} B_{kb} \cdot \prod_{\substack{\text{bkg.} \\ \text{syst.} \\ s}} \nu_{bs}(\theta_s) \right) \cdot \prod_{\substack{\text{CRs l} \\ \text{bins b}}} P\left(N_{lb} \middle| \sum_{\text{bkg k}} \theta_{kb} B_{klb} \right) \cdot \prod_{\substack{\text{syst} \\ t}} g(\delta_t|\theta_t) \cdot \prod_{\text{bkg k}} P(\xi_k|\zeta_k\theta_k) \,. \tag{7.6}$$

Where $\boldsymbol{\theta}$ represents the full set of nuisance parameters, r is an index for signal systematics, s is an index for background systematics, and t is an index for Monte Carlo samples. The fourth term of the equation quantifies the uncertainty due to finite Monte Carlo sample size. Here, ξ represents the central value of the background prediction, θ is the associated nuisance parameter, and $\zeta = (B/\delta B)^2$, where δB is the statistical uncertainty of B.

The best fit value of the signal strength μ is determined by finding the values of μ and $\boldsymbol{\theta}$ that maximize the likelihood.Once the likelihood is defined, a test statistic must be built for use in hypothesis testing, described in Section 8.2.

7.7 Fit Results

The results of a background–only fit in the control regions are presented in detail in Table 7.11 for $E_T^{\text{miss}} >$ 250 GeV. Tables 7.3–7.4 collect the results for the total background predictions in each of the control regions for the inclusive and exclusive E_T^{miss} selections. As the tables indicate, the W/Z+jets background predictions receive multiplicative normalization factors that vary in the range between 0.8 and 1.2, depending on the process and the kinematic selection. Values of the 21 normalization factors determined from the background–only fit are shown in Figure 7.9. The effect of these normalization factors on the E_T^{miss} distributions of each control region is shown in Figure 7.10. Good agreement is observed between the normalization factors obtained by using inclusive or exclusive E_T^{miss} regions.

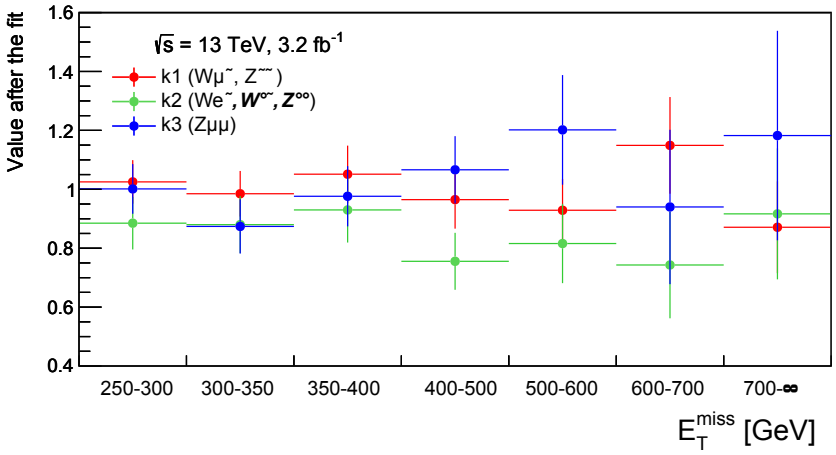


Figure 7.9: Values of the 21 normalization factors determined from the background–only fit.

$E_T^{\text{miss}} > 250$ GeV control regions	1–electron	1–muon	2–muon
Observed events (3.2 fb^{-1})	3559	10481	1488
SM prediction (post-fit)	3559 ± 60	10480 ± 100	1488 ± 39
Fitted $W \to e\nu$	2410 ± 140	0.4 ± 0.1	–
Fitted $W \to \mu\nu$	2.4 ± 0.3	8550 ± 330	1.8 ± 0.3
Fitted $W \to \tau\nu$	462 ± 27	435 ± 28	0.14 ± 0.02
Fitted $Z \to ee$	0.5 ± 0.1	–	–
Fitted $Z \to \mu\mu$	0.02 ± 0.02	143 ± 10	1395 ± 41
Fitted $Z \to \tau\tau$	30 ± 2	22 ± 4	0.5 ± 0.1
Fitted $Z \to \nu\nu$	1.8 ± 0.1	2.3 ± 0.2	–
Expected $t\bar{t}$, single top	500 ± 150	1060 ± 330	42 ± 13
Expected dibosons	150 ± 13	260 ± 25	48 ± 5
MC exp. SM events	3990 ± 320	10500 ± 710	1520 ± 98
Fit input $W \to e\nu$	2770 ± 210	0.4 ± 0.1	–
Fit input $W \to \mu\nu$	2.4 ± 0.3	8500 ± 520	1.8 ± 0.2
Fit input $W \to \tau\nu$	531 ± 39	500 ± 34	0.16 ± 0.03
Fit input $Z \to ee$	0.5 ± 0.1	–	–
Fit input $Z \to \mu\mu$	0.02 ± 0.02	146 ± 13	1427 ± 92
Fit input $Z \to \tau\tau$	34 ± 3	25 ± 4	0.6 ± 0.1
Fit input $Z \to \nu\nu$	1.8 ± 0.1	2.2 ± 0.1	–
Fit input $t\bar{t}$, single top	500 ± 160	1060 ± 340	42 ± 13
Fit input dibosons	150 ± 13	260 ± 25	48 ± 5

Table 7.11: Data and background predictions in the control regions before and after the fit is performed for $E_T^{\text{miss}} > 250$ GeV. The background predictions include both the statistical and systematic uncertainties. Omitted values are negligible. The individual uncertainties are correlated, and do not necessarily add in quadrature to the total background uncertainty.

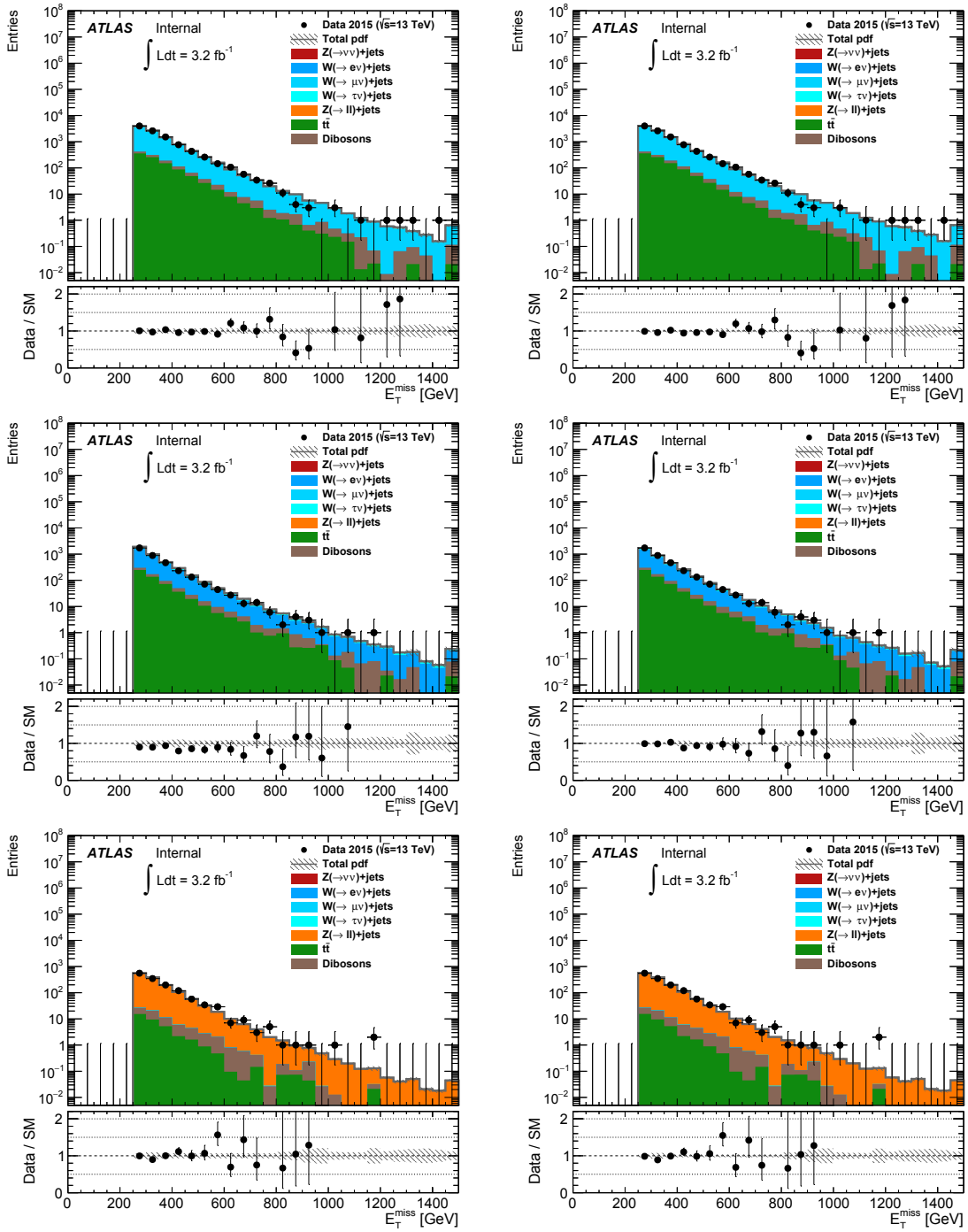


Figure 7.10: Distributions of the measured E_T^{miss} before (left) and after (right) the simultaneous shape fit in the 1–muon control region (top), 1–electron control region (middle), and 2–muon control region (bottom). In the pre–fit plots the error bands in the ratios include the statistical and experimental uncertainties in the background predictions. In the post–fit plots distributions are scaled with global normalization factors extracted from the fit as performed in exclusive missing transverse momentum bins. The error bands in the ratios include the statistical and experimental uncertainties in the background predictions as determined by the global fit to the data in the control regions. The contributions from multijets and non-collision backgrounds are negligible and are not shown in the figures.

8

Results and Interpretation

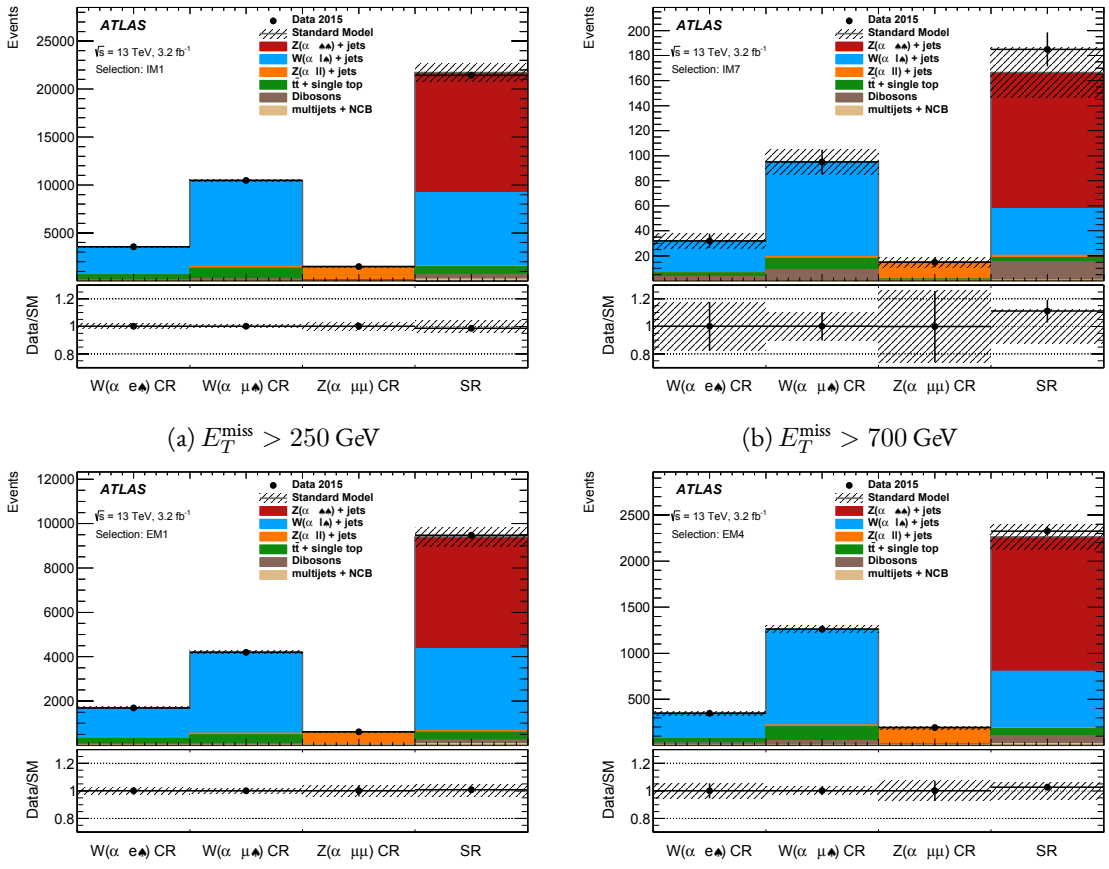
8.1 Signal Region Yields

The results of the background estimation scheme and observed data yields are presented in this section. The observed and expected yields as determined by the fit are presented in Figure 8.1 for selected E_T^{miss} ranges. A detailed breakdown of the number of events in data and expected contributions from individual background processes in the signal region for certain E_T^{miss} ranges is presented in presented in Table 8.1. The total background results for all of the signal regions are summarized in Table 8.2.

Figure 8.2 shows several measured distributions compared to the corrected Standard Model predictions for $E_T^{\text{miss}} > 250\,\text{GeV}$. The the related uncertainties are determined from the global fit carried out in exclusive E_T^{miss} bins. For illustration purposes, the distributions include the E_T^{miss} distributions of several signal models.

Good agreement is observed between the data and the background predictions in each region. The background yield for the inclusive selections is determined with a total uncertainty of $\pm 4.0\%$, $\pm 6.8\%$, and

$\pm 12\%$ for the $[250, \infty]$, $[500, \infty]$, and $[700, \infty]$ signal regions, respectively. This uncertainty includes correlations between uncertainties in the individual background contributions.



(a) $E_T^{\text{miss}} > 250$ GeV

(b) $E_T^{\text{miss}} > 700$ GeV

(c) $250 < E_T^{\text{miss}} < 300$ GeV

(d) $400 < E_T^{\text{miss}} < 500$ GeV

Figure 8.1: Observed and expected events in the signal and control regions for $E_T^{\text{miss}} > 250$ GeV (a), $E_T^{\text{miss}} > 700$ GeV (b), $250 < E_T^{\text{miss}} < 300$ GeV (c), and $400 < E_T^{\text{miss}} < 500$ GeV (d). The expected yields include the global normalization factors extracted from the corresponding fit. The error bands in the ratios include the statistical and experimental uncertainties on the background predictions.

Signal Region [E_T^{miss} bin edges in GeV]	$[250, \infty]$	$[350, 400]$	$[500, 600]$	$[700, \infty]$
Observed events (3.2 fb^{-1})	21447	2939	747	185
SM prediction	21730 ± 940	3210 ± 170	686 ± 50	167 ± 20
$W \to e\nu$	1710 ± 170	228 ± 26	37 ± 7	7 ± 2
$W \to \mu\nu$	1950 ± 170	263 ± 28	44 ± 8	11 ± 2
$W \to \tau\nu$	3980 ± 310	551 ± 47	101 ± 15	19 ± 4
$Z \to ee$	0.01 ± 0.01	–	–	–
$Z \to \mu\mu$	76 ± 30	9 ± 5	5 ± 2	2 ± 1
$Z \to \tau\tau$	48 ± 7	5 ± 1	0.9 ± 0.2	0.2 ± 0.1
$Z \to \nu\nu$	12520 ± 700	1940 ± 130	443 ± 42	109 ± 18
$t\bar{t}$, single top	780 ± 240	108 ± 32	19 ± 7	3 ± 1
Dibosons	506 ± 48	82 ± 8	36 ± 5	15 ± 2
Multijets	51 ± 50	6 ± 6	1 ± 1	0.4 ± 0.4
Non-collision background	110 ± 110	19 ± 19	–	–

Table 8.1: Data and SM background predictions in the signal region for several inclusive and exclusive missing transverse momentum selections. For the SM prediction both the statistical and systematic uncertainties are included. In each signal region, the individual uncertainties for the different background processes can be correlated, and do not necessarily add in quadrature to the total background uncertainty. Negligible yields are omitted.

Signal Region	$[250, \infty]$	$[300, \infty]$	$[350, \infty]$	$[400, \infty]$	$[500, \infty]$	$[600, \infty]$	$[700, \infty]$
Observed events	21447	11975	6433	3494	1170	423	185
SM prediction	21730 ± 940	12340 ± 570	6570 ± 340	3390 ± 200	1125 ± 77	441 ± 39	167 ± 20
Signal Region	$[250, 300]$	$[300, 350]$	$[350, 400]$	$[400, 500]$	$[500, 600]$	$[600, 700]$	
Observed events	9472	5542	2939	2324	747	238	
SM prediction	9400 ± 410	5770 ± 260	3210 ± 170	2260 ± 140	686 ± 50	271 ± 28	

Table 8.2: Data (3.2 fb^{-1}) and SM background predictions in the signal region for the different selections. For the SM predictions both the statistical and systematic uncertainties are included.

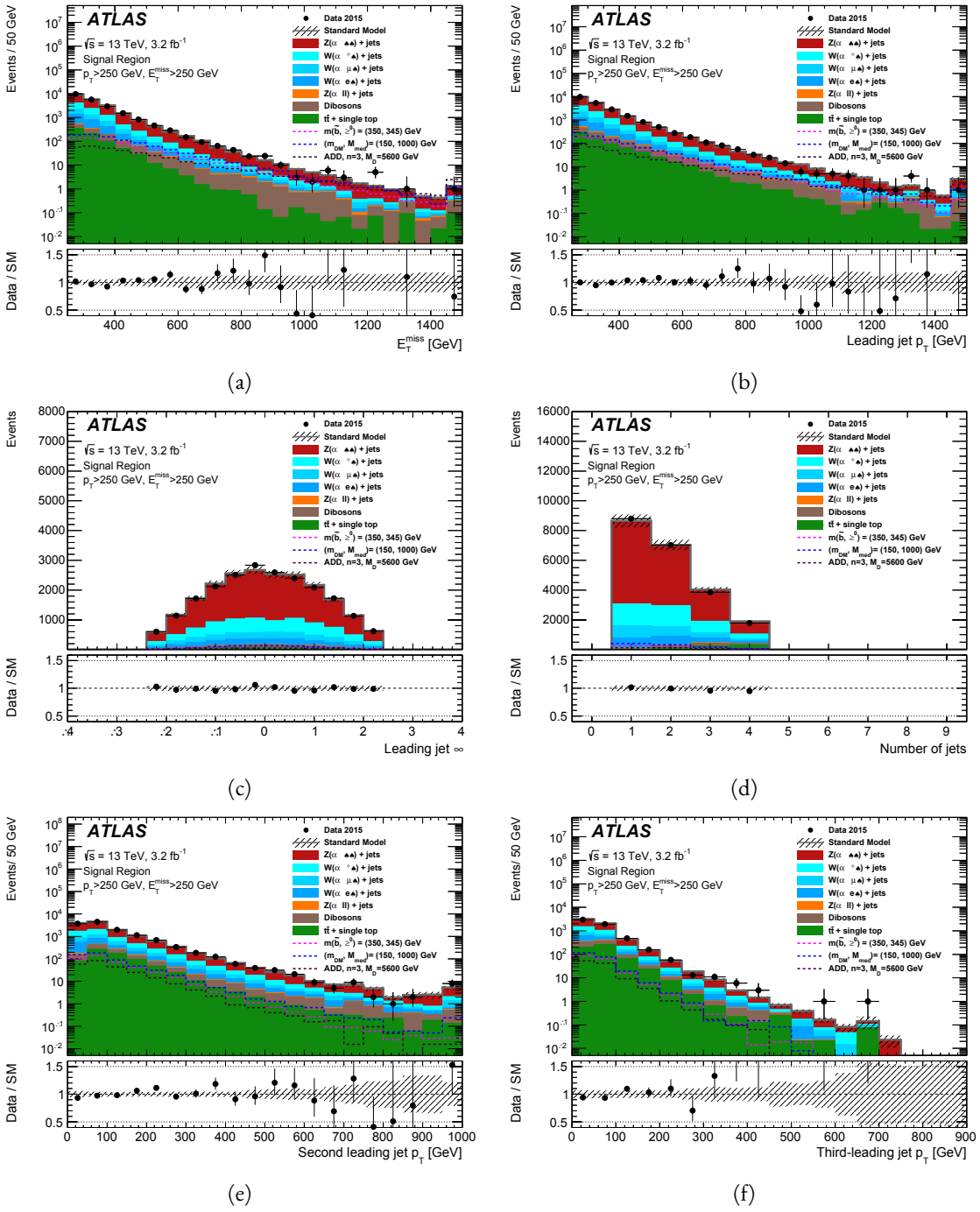


Figure 8.2: Measured distributions of the $E_T^{\text{miss}} > 250$ GeV signal region selection compared to the SM predictions as a function of: E_T^{miss} (a), leading jet p_T (b), leading jet η (c), jet multiplicity (d), second-leading jet p_T (e), and third-leading jet p_T (f). The SM predictions are normalized with normalization factors as determined by the global fit that considers exclusive E_T^{miss} regions. For illustration purposes, the distributions of different ADD, SUSY, and WIMP scenarios are included. The error bands in the ratio shown in the lower panel include both the statistical and systematic uncertainties in the background expectations. The contributions from multijets and non-collision backgrounds are negligible and not shown. No excess is observed.

8.2 Setting Limits

In the absence of any excess, the observed data and predicted background yields are used to set model-independent limits on new phenomena. The CL_s method [115] is used to set exclusion limits in this analysis.

A test statistic is used for setting limits, and measures the degree of agreement between the data and the hypothesized signal with strength $\mu = \sigma/\sigma_{\text{theory}}$. The test statistic is defined as:

$$\widetilde{q_\mu} = \begin{cases} -2\ln\frac{L(\mu,\hat{\hat{\theta}}(\mu))}{L(0,\hat{\hat{\theta}}(0))} & \hat{\mu} < 0 \\ -2\ln\frac{L(\mu,\hat{\hat{\theta}}(\mu))}{L(\hat{\mu},\hat{\theta})} & 0 \leq \hat{\mu} < \mu \\ 0 & \hat{\mu} > \mu \end{cases} \tag{8.1}$$

where μ is the value of the signal strength under test, $\hat{\mu}$ is the best fit μ, $\hat{\theta}$ is the best fit value of the nuisance parameters, $\hat{\hat{\theta}}$ is the best fit value of the nuisance parameters under the fixed μ value, and L is the Poisson likelihood of the data (as described in section 7.6.2).

Higher values of $\widetilde{q_\mu}$ represent greater incompatibility between the data and the hypothesized value of μ. Additionally, $\widetilde{q_\mu}$ is protected against negative, unphysical values of the signal strength μ, and does not count excesses in the data larger than those expected by a signal strength μ as evidence against the μ hypothesis.

Setting a limit on the cross section for new physics processes requires defining the following terms:

- CL_{s+b}: the probability that the signal+background hypothesis produces a value of the test statistic that is less than or equal to the observed value.
- CL_b: the probability that the background–only hypothesis produces a value of the test statistic less than or equal to the observed value.
- CL_s: the ratio CL_{s+b}/CL_b.

A 95% upper limit on the cross section is defined as the value of μ that makes CL_s less than 5%. This is an exclusion interval. A 95%CL_s limit makes the statement that the probability of falsely excluding a

true signal with signal strength μ is less than 5% in the excluded range or region. Models are considered excluded when $\mu \leq 1$ ($\sigma < \sigma_{\text{theory}}$) for $95\%\text{CL}_s$.

8.3 Model Independent Limits

An upper limit is set on the number of events in each signal region that could be produced by new physics. A simultaneous likelihood fit is performed in both the control regions for different E_T^{miss} ranges. Model-independent 95% confidence level (CL) upper limits on the visible cross section, defined as the production cross section σ times acceptance A times efficiency ϵ, are extracted using the CL_s method and considering the systematic uncertainties in the SM backgrounds and the uncertainty in the integrated luminosity.

The results are presented in Table 8.3. Values of $\sigma \times A \times \epsilon$ above 553 fb for $E_T^{\text{miss}} > 250$ GeV and above 19 fb for $E_T^{\text{miss}} > 700$ GeV are excluded at 95% CL. Typical event selection efficiencies ϵ varying from about 100% for $E_T^{\text{miss}} > 250$ GeV to 96% for $E_T^{\text{miss}} > 700$ GeV are found in simulated $Z \to \nu\nu$+jets background processes.

Signal channel	$\langle\sigma\rangle_{\text{obs}}^{95}$ [fb]	S_{obs}^{95}	S_{exp}^{95}
$E_T^{\text{miss}} > 250$ GeV	553	1773	1864^{+829}_{-548}
$E_T^{\text{miss}} > 300$ GeV	308	988	1178^{+541}_{-348}
$E_T^{\text{miss}} > 350$ GeV	196	630	694^{+308}_{-204}
$E_T^{\text{miss}} > 400$ GeV	153	491	401^{+168}_{-113}
$E_T^{\text{miss}} > 500$ GeV	61	196	164^{+63}_{-45}
$E_T^{\text{miss}} > 600$ GeV	23	75	84^{+32}_{-23}
$E_T^{\text{miss}} > 700$ GeV	19	61	48^{+18}_{-13}

Table 8.3: Observed and expected 95% CL upper limits on the number of signal events, S_{obs}^{95} and S_{exp}^{95}, respectively. This table also shows the upper limit on the visible cross section $\langle\sigma\rangle_{\text{obs}}^{95}$ for $E_T^{\text{miss}} > 250$ GeV through $E_T^{\text{miss}} > 700$ GeV.

8.4 Dark Matter Interpretation

The results are translated into exclusion limits on the WIMP pair-production cross section for an axial-vector particle mediating an s-channel exchange. For on-shell WIMP pair-production, where $m_A > 2m_\chi$, typical $A \times \epsilon$ values for signal models with a 1 TeV mediator range from 25% to 2% for $E_T^{\text{miss}} > 250$ GeV and $E_T^{\text{miss}} > 700$ GeV signal region selections, respectively.

Figure 8.3 shows the observed and expected 95% CL exclusion limits in the m_χ–m_A parameter plane for a simplified model with an axial-vector mediator, Dirac WIMPs, and couplings $g_q = 1/4$ and $g_\chi = 1$. A minimal mediator width is assumed. In addition, observed limits are shown using $\pm 1\sigma$ theoretical uncertainties in the signal cross sections. In the region of phase space where the mediator is heavy enough to decay into a pair of WIMPs ($m_A > 2m_\chi$, called the "on-shell regime"), the models with mediator masses up to 1 TeV are excluded. This analysis loses sensitivity to the models in the off-shell regime ($m_A < 2m_\chi$) where the decay into a pair of WIMPs is kinematically suppressed. The perturbative unitarity is violated in the parameter region defined by $m_\chi > \sqrt{\pi/2}\, m_A$ [116].

Comparing the relic density predicted by the benchmark models to the measured relic density provides some insight on the viability of a given choice of model parameters. The freezeout temperature and relic density of dark matter can be calculated for each point of (m_A,m_χ) phase space in Figure 8.3, assuming that all of the DM interactions are encapsulated by the simplified model, as discussed in Section 2.5. This prediction is then compared to the the correct relic density as measured by the Planck and WMAP satellites [117, 118]. The red line in Figure 8.3 (left) indicates where the relic density as calculated with the simplified model agrees with the measured relic density. Below this line are models that result in an overproduction of dark matter. Models above the line predict dark matter underproduction, and require other WIMP production mechanisms in order to explain the observed dark matter relic density. The line indicates relic abundance corresponding to a single spices of Dirac fermion dark matter and a single mediator that couples to all standard model quarks universally. As such, a given model's incompatibility with the observed relic abundance does not imply that the model is excluded. Instead, it implies that additional physics not encapsulated in the simplified model is relevant for determining the dark matter relic density.

The analysis sensitivity to coupling choices in examined in Fig. 8.4. The ratios of the observed and expected 95% CL upper limits on cross section to the predicted signal cross section for the s-channel model with axial-vector couplings and $m_\chi = 150$ GeV, $m_A = 1$ TeV, for different choices of the coupling $g = g_q = g_\chi$. The yellow band indicates the expected $\pm 1\sigma$ ranges of limits in the absence of a signal. Minimal mediator width is assumed. $g > 0.8$ is excluded.

In Figure 8.5 the results are translated into 90% CL exclusion limits on the spin-dependent WIMP–

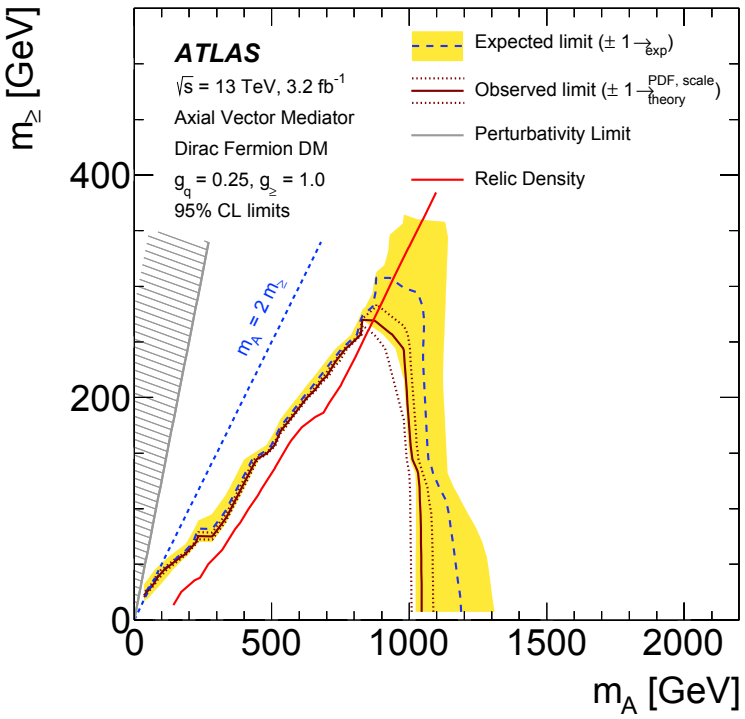


Figure 8.3: 95% CL exclusion contours in the m_χ–m_A parameter plane. The solid (dashed) curve shows the median of the observed (expected) limit, while the bands indicate the $\pm 1\sigma$ theory uncertainties in the observed limit and $\pm 1\sigma$ range of the expected limit in the absence of a signal. The red curve corresponds to combinations of dark matter and mediator mass that are consistent with a dark matter thermal relic density of $\Omega_c h^2 = 0.12$, as computed in MadDM [43]. The region where the model violates perturbative unitarity [116], defined by $m_\chi > \sqrt{\pi/2}\, m_A$, is indicated by the hatched area.

proton and WIMP–neutron scattering cross section as a function of the WIMP mass, following the technique described in Section 2.4.2, and are compared to results from the direct-detection experiments XENON100 [27], LUX [28], and PICO [29, 30]. This comparison is model-dependent and only valid in the context of this particular axial vector mediator model. In this case, stringent limits on the scattering cross section of the order of 10^{-42} cm^2 up to WIMP masses of about 300 GeV are provided by this analysis, and complement the results from direct-detection experiments for $m_\chi < 10$ GeV. The loss of sensitivity in models where WIMPs are produced off-shell is expressed by the turn of the exclusion line, reaching back to low WIMP masses and intercepting the exclusion lines from the direct-detection experiments at around $m_\chi = 80$ GeV.

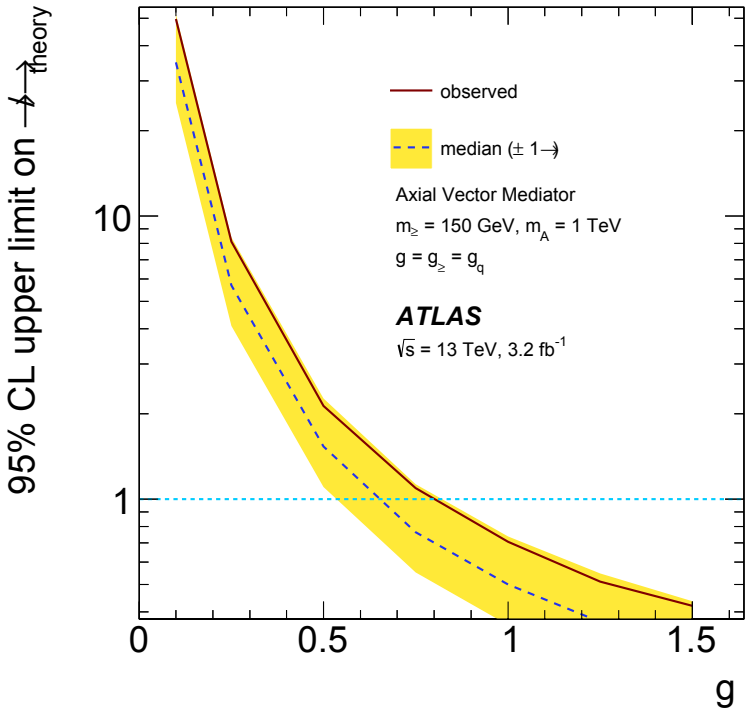


Figure 8.4: 95% CL upper limits on signal strength for different choices of the coupling $g = g_q = g_\chi$. The yellow band indicates the expected $\pm 1\sigma$ ranges of limits in the absence of a signal.

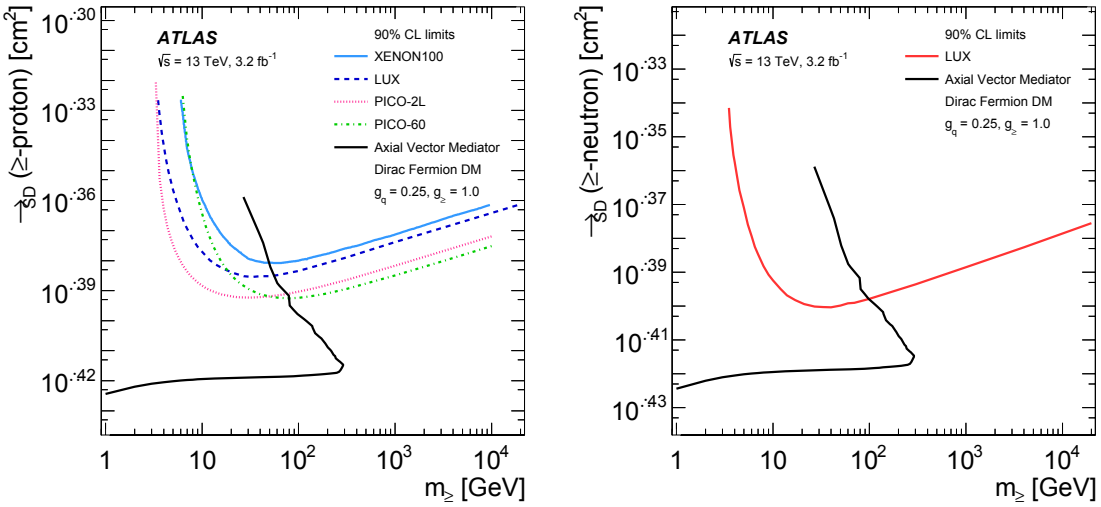


Figure 8.5: A comparison of the production cross section limits to the constraints from direct detection experiments on the spin-dependent WIMP–proton (left) and WIMP–neutron(right) scattering cross section in the context of the Z'-like simplified model with axial-vector couplings. Unlike in the m_χ–m_A parameter plane, the limits are shown at 90% CL. The results from this analysis, excluding the region to the left of the contour, are compared with limits from the XENON100 [27], LUX [28], and PICO [29, 30] experiments. The comparison is model-dependent and solely valid in the context of this model, assuming minimal mediator width and the coupling values $g_q = 0.25$ and $g_\chi = 1$.

8.5 Monojet and Dijet Complementarity

Limits from dijet resonance searches (for a brief overview see Appendix C) can also constrain Dark Matter production at the LHC by putting limits on the production of the mediator itself [119]. Although the monojet search is sensitive to the mediator decay to Dark Matter, the mediator may also decay to quarks. This decay channel would manifest as a resonance in the dijet mass spectrum, shown Figure C.1.

The relative exclusion power of the monojet and dijet channels is a function of the model couplings. The dijet $q\bar{q} \to A \to q\bar{q}$ cross section scales as g_{q}^4, whereas the monojet $q\bar{q} \to A \to \chi\bar{\chi}$ cross section scales as $g_{\mathrm{q}}^2 g_\chi^2$. As such, monojet limits will be more powerful when the mediator A interacts weakly with Standard Model quarks, and vice–versa.

The constraint provided by the dijet channel is important for models in which Dark Matter has a sizeabe interaction with Standard Model particles. In this case, the annihilation cross section for the WIMP dark matter candidate is so high that it can only be a subcomponent of the total dark matter relic density, reducing the exclusion power of direct and indirect detection experiments.

Figure 8.6 shows the monojet and dijet exclusion of dark matter models [120]. The exclusions from the ATLAS dijet searches are derived from limits on Gaussian-shaped resonances [121] in the dijet mass spectrum. The search for new resonances in a dijet system accompanied by a photon or jet Initial-State Radiation (ISR) [122] excludes mediator masses starting at 200 GeV. Results from the Trigger-object Level Analysis [123] and the dijet resonance searches at 8 TeV [121] and 13 TeV [124] constrain the parameter space starting from 425 GeV up to 2.5-2.8 TeV depending on the value of the dark matter mass.

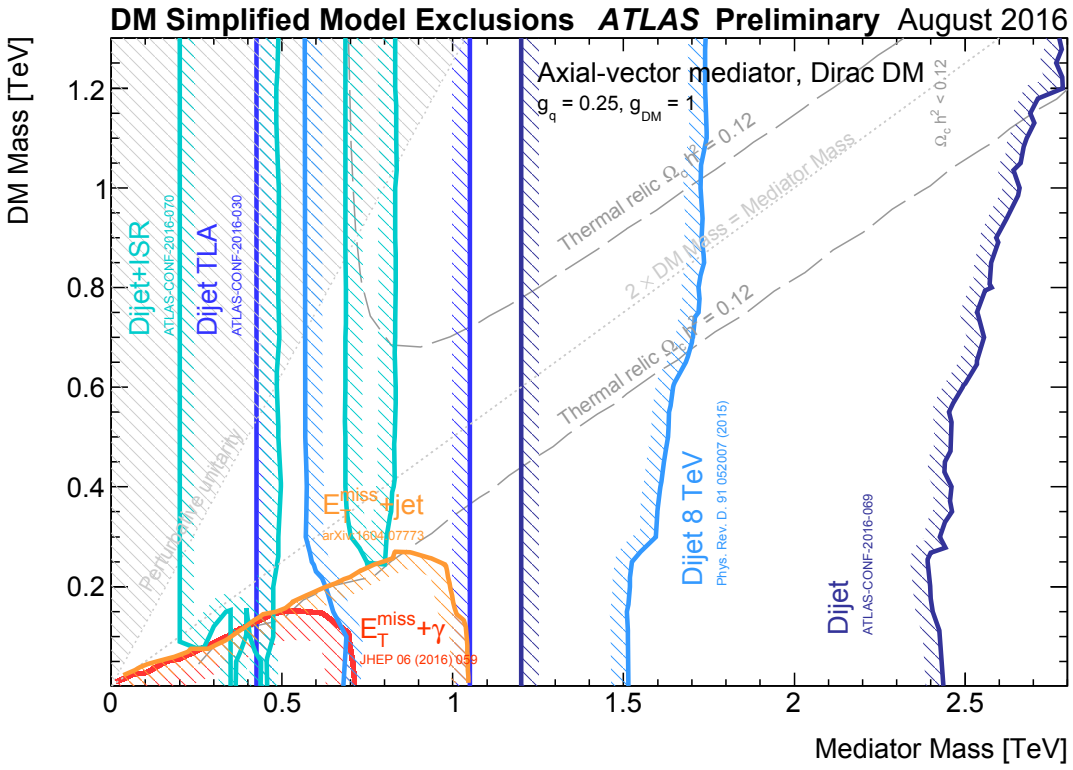


Figure 8.6: Regions of 95% CL exclusion in the m_χ–m_A parameter plane for various ATLAS Dark Matter searches with dark matter coupling $g_{\mathrm{DM}} = 1.0$ and quark coupling $g_{\mathrm{q}} = 0.25$ [120]. The gray dashed curve labeled "thermal relic" corresponds to combinations of dark matter and mediator mass that are consistent with a dark matter thermal relic density of $\Omega_c = 0.12h^2$, as computed in MadDM [43]. Between the two curves, annihilation processes described by the simplified model deplete $\Omega_c h^2$ below 0.12. The dotted curve indicates the kinematic threshold where the mediator can decay on-shell into dark matter. Points in the plane where the model violates perturbative unitary considerations [116] are indicated by the shaded triangle at the upper left. The exclusions from the ATLAS dijet searches are derived from limits on Gaussian-shaped resonances [121] in the dijet mass spectrum. The search for new resonances in a dijet system accompanied by a photon or jet Initial-State Radiation (ISR) [122] excludes mediator masses starting at 200 GeV. Results from the Trigger-object Level Analysis [123] and the dijet resonance searches at 8 TeV [121] and 13 TeV [124] constrain the parameter space starting from 425 GeV up to 2.5-2.8 TeV depending on the value of the dark matter mass.

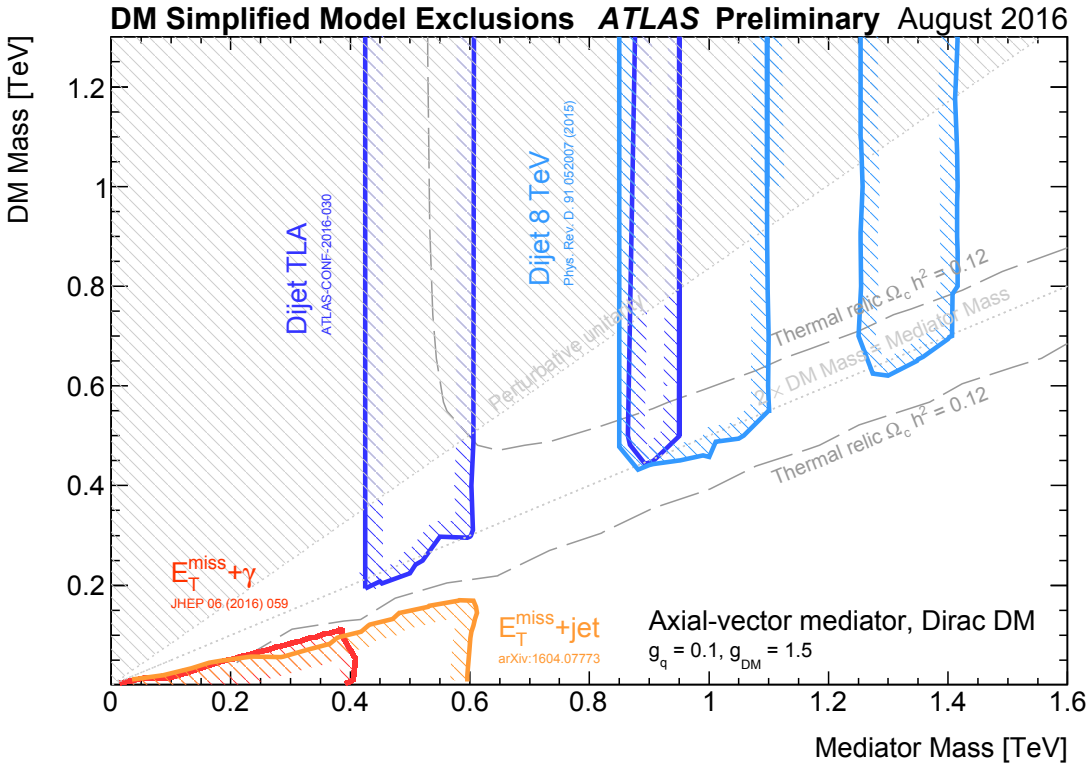


Figure 8.7: An alternate version of Figure 8.6 with exclusions computed for dark matter coupling $g_{\mathrm{DM}} = 1.5$ and quark coupling $g_{\mathrm{q}} = 0.1$ [120]. With this choice of couplings, the mediator decays to quarks are suppressed in favor of a higher branching ratio to dark matter particles, reducing the sensitivity of dijet searches to this scenario. The monojet and monophoton exclusion regions are obtained by rescaling, using acceptance and cross-section information from samples simulated at truth-level, the exclusion contours published in the corresponding papers. The discontinuous regions of dijet exclusion arise from fluctuations in the exclusion contours, shown in Figures C.2 and C.4.

Part IV

Looking Ahead

9

Ongoing Analysis Improvements

Before the end of the 13 TeV data–taking period, the results of mono–jet analysis will be limited by systematic rather than statistical uncertainties [125]. The largest systematic uncertainties in the analysis (described in Section 7.4) are a 2%–4% uncertainty from the $Z \to \nu\nu$ normalization and a 3% uncertainty from the top quark modeling.

Several techniques to reduce the systematic uncertainty are under development. A new photon-jet control region will provide an additional constraint on the Standard Model background in the signal region and reduce the $Z \to \nu\nu$ normalization uncertainty. Additionally, the current profile likelihood fit strategy can be extended to extract signal sensitivity from the additional event variables, which may provide a sensitivity improvement of more than 30% for the next analysis result.

9.1 Photon Control Region

In the $\sqrt{s} = 13$ TeV 3.2 fb^{-1} iteration of the monojet analysis, the $W \to \mu\nu$ process is used to constrain the $Z \to \nu\nu$ contribution in the signal region, and any discrepancy is accounted for with the `WZtransfer` uncertainty described in Section 7.4.1. This scheme is not a unique choice, nor is it necessarily the optimal strategy.

The γ+jets process has a larger cross section than the leptonic decay channels of W+jets or Z+jets. A high–p_T photon also provides a clean event signature with low contamination from multi-jet process. Additionally, at high–p_T the photon momentum strongly resembles the Z momentum, as shown in Figure 9.1. The γ+jet process is a natural candidate to estimate the $Z \to \nu\nu$ background, especially at high values of E_T^{miss}.

A preliminary study of this alternate normalization scheme was performed for a luminosity of 5 fb^{-1} using background Monte Carlo processes. A 1–photon control region was defined. Events in this region were selected using a photon trigger and required to have only one photon balanced with the leading jet: $\Delta\phi(\gamma, \text{jet}_1) > 1.0$ and $p_T^{\text{jet}_1}/p_T^{\gamma} > 0.5$. The other selection cuts are consistent with the signal region selection defined in Chapter 6.4, with the photon treated as an invisible particle in the calculation of E_T^{miss}. In this way, the invisible photon p_T resembles the E_T^{miss} of $Z \to \nu\nu$ events.

Figure 9.1 shows the p_T distributions of photon p_T in the 1–photon control region and the dimuon Z p_T in the 2–muon control region. Good agreement is observed beyond 350 GeV. Figure 9.2 shows the E_T^{miss} distributions in signal region, 1–muon, 2–muon and 1–photon control regions. The 1–photon control region E_T^{miss} distribution agrees best with the $Z \to \nu\nu$ process.

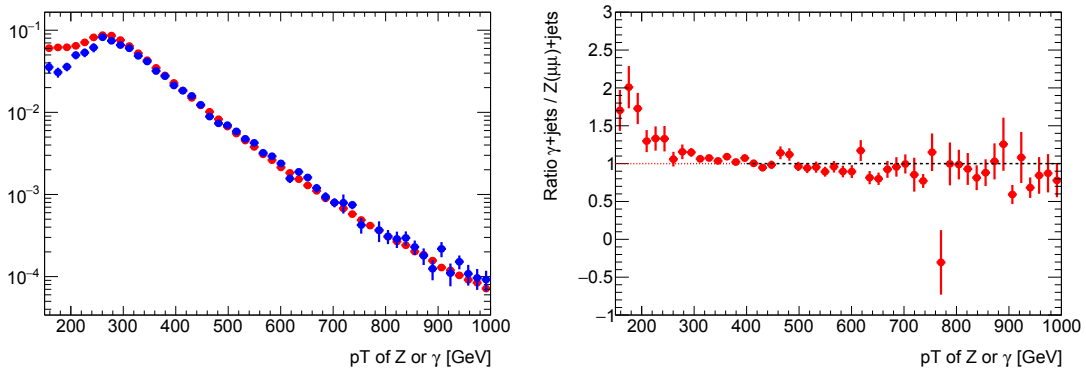


Figure 9.1: The p_{T} distributions (left) and ratio (right) of γ+jets in red and $Z(\mu\mu)$+jets in blue. The area of the histograms is normalized to the same number beyond 400 GeV.

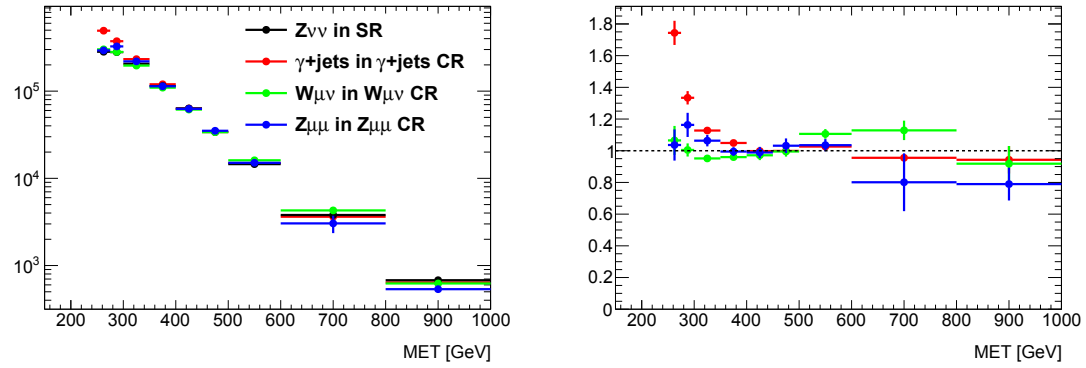


Figure 9.2: The E_T^{miss} distributions (left) and ratio (right) of γ+jets in red and $Z(\mu\mu)$+jets in blue. The area of the histograms is normalized to the same number beyond 400 GeV.

The MC yield with a luminosity of 5 fb^{-1} and purity in different control regions are shown in Table 9.1. The purity is calculated as the primary process event yield divided by the total number of events in the region. The 1–photon control region has both a higher purity and higher event yield compared to the other control regions.

Including 1–photon control region is a promising step towards improving the analysis sensitivity. However, a complete one-to-one comparison with the `WZtransfer` strategy is impossible without the corresponding γ+jet theoretical uncertainties, which are not yet available. A preliminary study not considering the theoretical uncertainties indicates that using a 1–photon control region instead of the 1–muon control region to estimate $Z(\nu\nu)$+jets process in the signal region may improve the model-independent limit on visible cross-section by 26% for $E_T^{\mathrm{miss}} > 400$ GeV and 62% for $E_T^{\mathrm{miss}} > 600$ GeV.

CR	1–electron	1–muon	2–muon	1–photon
		$E_T^{\text{miss}} > 400$ GeV		
MC yield	823.5 ± 12.7	2977.5 ± 51.4	375.5 ± 18.8	5200.5 ± 2.6
purity	77.5%	81.1%	94.1%	99.5%
		$E_T^{\text{miss}} > 600$ GeV		
MC yield	104.5 ± 9.4	403.0 ± 19.0	40.0 ± 6.3	644.0 ± 1.6
purity	77.0%	83.4%	92.5%	98.8%

Table 9.1: MC event yield and purity with 5 fb^{-1} luminosity for $E_T^{\text{miss}} > 400$ GeV and $E_T^{\text{miss}} > 600$ GeV.

9.2 Two-Dimensional Fit

A preliminary study was performed in MC to check if additional sensitivity can be obtained by using bins in jet multiplicity in addition to E_T^{miss} in the profile likelihood fit. This can better limit systematics that depend on jet multiplicity, as a fluctuation in jet modeling will not affect the yields in all bins equally. Additionally, dark matter limits may benefit from an improved signal–background ratio by binning in jet multiplicity. Figure 9.3 shows the jet multiplicity for backgrounds and select dark matter processes in the signal region.

The same E_T^{miss} binning scheme as in the simplified shape fit is used, with one normalization factor per bin of E_T^{miss}. However, the signal and control regions are further subdivided according to jet multiplicity into 1–, 2–, 3–, and 4–jet bins. The relative impact of this subdivision on the systematic uncertainties is shown in Table 9.2.

The two-dimensional fitting strategy better constrains the top, jet, and E_T^{miss} systematics, resulting in improved limits as shown in Table 9.3. Axial vector mediator limits are improved by $\sim 30\%$ and pseudoscalar mediator limits are improved by $> 30\%$ at low m_ϕ. The corresponding changes to the m_χ–m_A and m_χ–m_ϕ limits are shown in Figure 9.4. The limits are improved across all of (m_χ,m_{med}) phase space.

The multivariate fitting scheme will be an excellent analysis extension once enough data is available to populate the twenty–one signal region (E_T^{miss}, N_{jet}) bins.

Experimental Uncertainty	Impact with Nominal Fit	Impact with 2D Fit
lumiSys	(−0.54%,0.55%)	(−0.03%,0.03%)
EG_RESOLUTION_ALL	(0.02%,0.01%)	(0.01%,0.01%)
EG_SCALE_ALL	(0.09%,−0.09%)	(0.12%,−0.12%)
EL_EFF_ID_TotalCorrUncertainty	(−0.62%,0.64%)	(−0.63%,0.65%)
EL_EFF_Iso_TotalCorrUncertainty	(−0.11%,0.12%)	(−0.13%,0.13%)
EL_EFF_Reco_TotalCorrUncertainty	(−0.22%,0.23%)	(−0.25%,0.26%)
JET_GroupedNP_1	(−1.02%,0.78%)	(0.54%,−0.55%)
JET_GroupedNP_2	(−0.87%,0.52%)	(−0.22%,−0.02%)
JET_GroupedNP_3	(−0.25%,0.47%)	(0.04%,0.20%)
JET_JER_SINGLE_NP	(0.65%,−0.69%)	(0.41%,−0.39%)
MET_SoftTrk_ResoPara	(0.20%,−0.19%)	(0.17%,−0.16%)
MET_SoftTrk_ResoPerp	(0.02%,−0.01%)	(0.05%,−0.04%)
MET_SoftTrk_Scale	(0.12%,−0.10%)	(0.06%,−0.02%)
MUONS_ID	(−0.02%,−0.08%)	(−0.05%,−0.09%)
MUONS_MS	(0.42%,−1.00%)	(0.46%,−1.11%)
MUONS_SCALE	(−0.01%,−0.00%)	(−0.02%,−0.00%)
MUON_EFF_STAT	(−0.21%,0.23%)	(−0.23%,0.23%)
MUON_EFF_STAT_LOWPT	(−0.00%,0.00%)	(−0.00%,0.00%)
MUON_EFF_SYS	(−1.42%,1.45%)	(−1.46%,1.49%)
MUON_EFF_SYS_LOWPT	(−0.00%,0.00%)	(−0.00%,0.00%)
top_Sys	(−3.42%,3.44%)	(−0.66%,0.76%)
Total Correlated Error	6.23%	2.02%

Table 9.2: Impact of experimental systematics on signal region yield when constrained with a fit only to the control regions. The systematics are defined in Section 7.4. The 2D fitting scheme strongly constrains the luminosity, jet, and top-background nuisance parameters.

Signal Sample	Nominal μ	2D Fit μ	% change
$m_\chi = 1$ GeV, $m_A = 0.5$ TeV	0.20	0.15	−25%
$m_\chi = 1$ GeV, $m_A = 1$ TeV	0.86	0.63	−27%
$m_\chi = 150$ GeV, $m_A = 1$ TeV	0.88	0.63	−28%
$m_\chi = 1$ GeV, $m_\phi = 0.5$ TeV	13.5	11.1	−18%
$m_\chi = 1$ GeV, $m_\phi = 1$ TeV	155	136	−12%
$m_\chi = 50$ GeV, $m_\phi = 0.3$ TeV	5.04	3.43	−32%

Table 9.3: Upper 95% CL limit on μ for different signal points using both the nominal fit and two-dimensional fit.

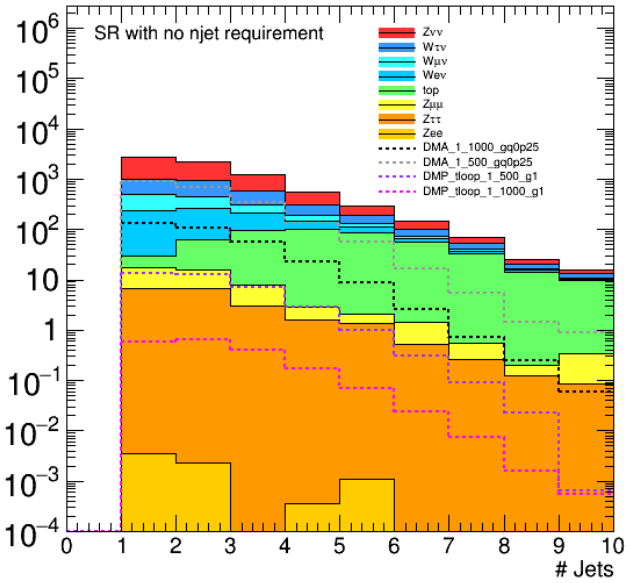


Figure 9.3: Jet multiplicity in the signal region with the N_{jet} cut removed. The jet multiplicity is shown for axial vector mediator models with $m_\chi = 1$ GeV, $m_A = 1$ TeV (black) and $m_\chi = 1$ GeV, $m_A = 0.5$ TeV (gray) as well as pseudoscalar mediator models with with $m_\chi = 1$ GeV, $m_\phi = 1$ TeV (pink) and $m_\chi = 1$ GeV, $m_\phi = 0.5$ TeV (purple).

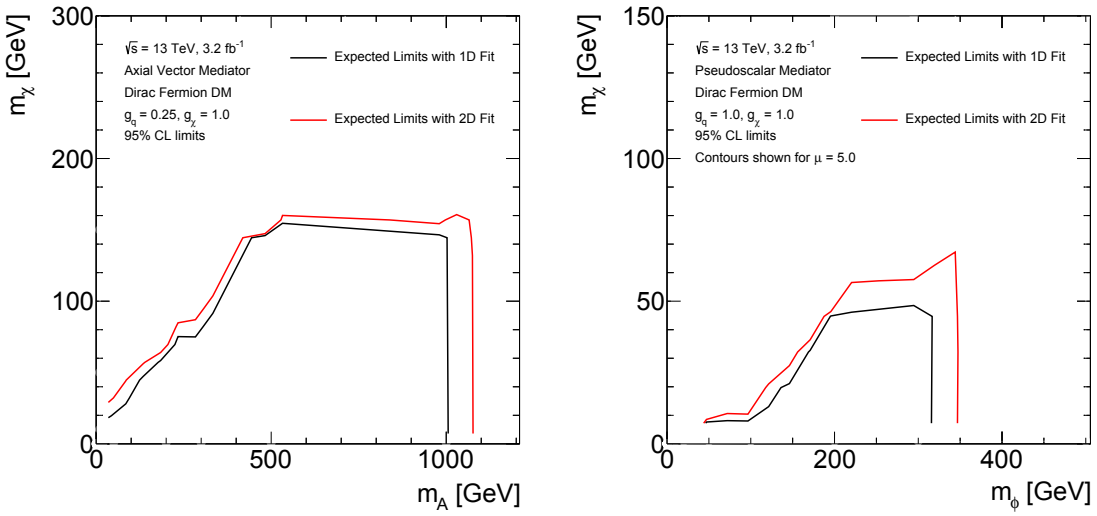


Figure 9.4: Expected excluded (m_χ, m_{med}) phase space for dark matter production via an axial vector mediator (left) or pseudoscalar mediator (right) when constraining the background uncertainties with the nominal (black) and two–dimensional (red) fitting schemes. No pseudoscalar mediator models are excluded, so the contour is shown for $\mu = 5$ instead of $\mu = 1$. This study was performed with a subset of the signal grid points used in Section 8.4.

10

Conclusions

This thesis has presented the results from a search for dark matter production in monojet events obtained from proton–proton collisions at $\sqrt{s} = 13$ TeV at the LHC, based on data corresponding to an integrated luminosity of 3.2 fb^{-1} collected by the ATLAS experiment in 2015. The measurements are in agreement with the Standard Model predictions.

In the absence of any excess, limits are placed on the existence of new physics. These results are translated into 95% CL model independent limits on the visible cross section for new physics. Additionally, the results are interpreted in terms of upper limits on the pair-production cross section of WIMP Dark Matter, using a simplified model with an axial-vector mediator and fermionic couplings $g_\chi = 1$ and $g_q = 0.25$. Mediator masses below 1 TeV are excluded at 95% CL for WIMP masses below 250 GeV. These results are converted into upper limits on spin-dependent contributions to the WIMP–nucleon elastic cross section as a function of the WIMP mass. WIMP–proton cross sections above 10^{-42} cm^2 are excluded at 90% CL for WIMP masses below 10 GeV, complementing results from direct-detection experiments.

These were one of the first limits on Dark Matter production derived from the 13 TeV LHC data–taking period. Sensitivity to these models will improve as the LHC continues to collect data. Together with limits from future direct detection experiments and relic density contraints, most of the relevant model phase space will be excluded in the coming years [119], as shown in Figure 10.1. If the dark sector interacts with quarks, it will be discovered here. If not, constraining this sector will have important ramifications for the future of dark matter detection efforts.

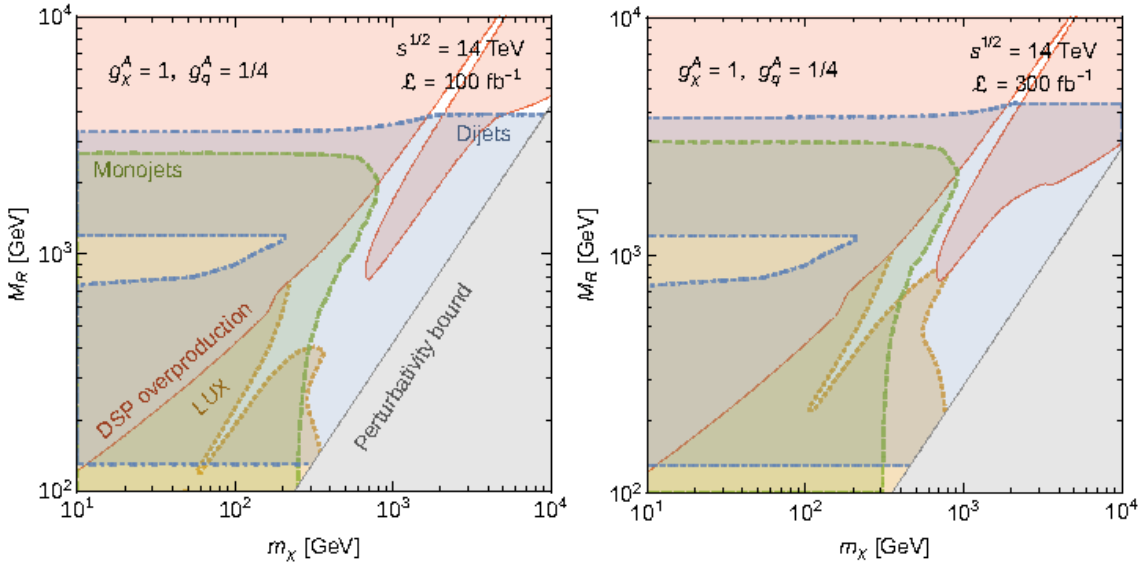


Figure 10.1: Projected three-year (left) and ten-year (right) sensitivities for near-future experiments [119] in the plane of DM mass m_χ and axial vector mediator mass M_R. The limits include monojet analyses (green), dijet resonances (blue), DM direct detection experiments (yellow), and excluding regions of phase space which predict an excess of thermal relic DM (red). The gray area contains models which violate perturbative unitary considerations [116].

A

Jet Quality Variables

This appendix presents a selection of additional plots examining jet quality variables.

A.1 Good and Fake Jet Topologies

The jet selection criteria should efficiently reject jets from background processes while keeping the highest efficiency selection for jets produced in proton-proton collisions. Since the level and composition of background depend on the jet multiplicity and the jet kinematics, two sets of criteria are proposed that each correspond to different levels of fake jet rejection and jet selection efficiency. Jet candidates arising as high energy objects produced in a collision event are called "good jets", while jet candidates coming from background processes are called "fake jets".

The criteria for the jet quality selection are optimized by studying two different event samples, one enriched with good and the other with fake jets:

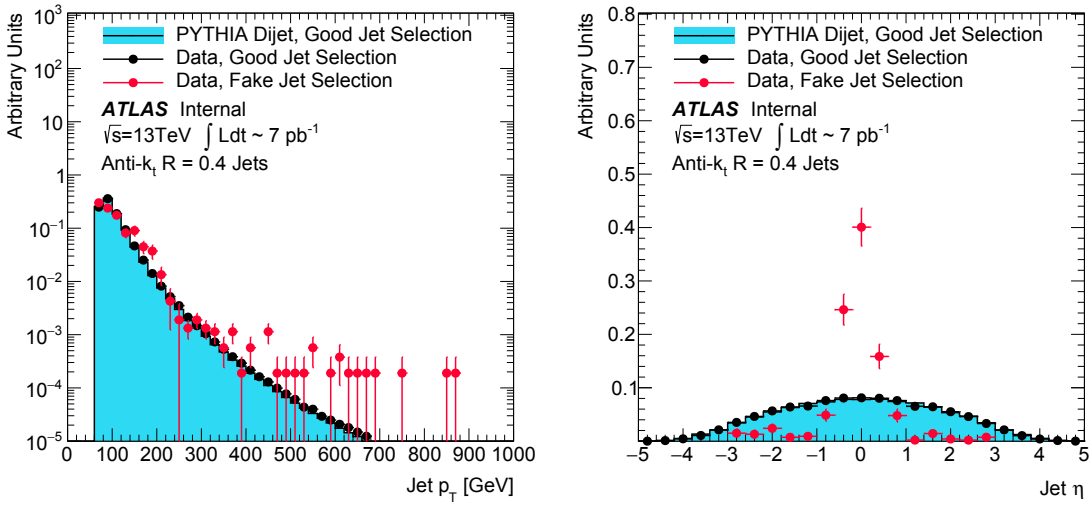
- Good jets are selected by requiring that the two leading jets have $p_T > 70$ GeV and are back-to-

back ($\Delta\phi_{j-j} > 3.0$ radians) in the plane transverse to the beam. The two jets are required to be balanced in transverse momentum ($|p_T^1 - p_T^2|/(p_T^1 + p_T^2) < 0.3$). Events are selected with single jet triggers.[1] For each p_T-bin considered in this analysis, a dedicated trigger chain is chosen that is fully efficient (> 99%) while having a prescale factor as small as possible. This sample is dominated by dijet events produced by strong interactions and will henceforth be referred to as the "good jets enriched sample".

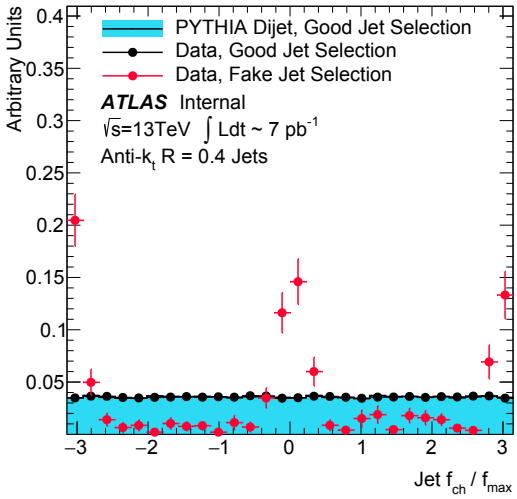
- Fake jets are selected from events with at least one jet with $p_T > 70$ GeV. Since events with fake jets are characterized by jets with unbalanced transverse momentum, only events satisfying $H_{\mathrm{T}}^{\mathrm{miss}} = |\overrightarrow{H}_{\mathrm{T}}^{\mathrm{miss}}| > 70$ GeV are retained. The variable $\overrightarrow{H}_{\mathrm{T}}^{\mathrm{miss}}$ is defined as $\overrightarrow{H}_{\mathrm{T}}^{\mathrm{miss}} = -\sum_{\mathrm{jets}} \overrightarrow{p_{\mathrm{T}}}$ where all jets with p_{T} greater than 20 GeV are considered. In addition, the direction of $\overrightarrow{H}_{\mathrm{T}}^{\mathrm{miss}}$ should be opposite to the transverse component of the jet momentum ($\Delta\phi_{H_{\mathrm{T}}^{\mathrm{miss}}-j} > 3.0$ radians). In order to reduce the contribution from physics processes like $Z(\rightarrow \nu\nu)$+jets, the leading jet is required to be out-of-time ($|t_{\mathrm{jet}}| > 6$ ns), where the jet time (t_{jet}) is defined is defined from the time of the calorimeter cell energy deposits by constructing the weighted average of the cell time t_{cell} in the jet, weighted by the square of the cell energies: $t_{\mathrm{jet}} = \sum E_{\mathrm{cell}}^2 t_{\mathrm{cell}} / \sum E_{\mathrm{cell}}^2$ where the sum runs over the cells belonging to the jet. Jets produced in proton-proton collisions are expected to be reconstructed at $t_{\mathrm{jet}} = 0$. This jet sample is dominated by non-collision backgrounds, and will henceforth be referred to as the "fake jets enriched sample". The jet triggers used for the good jets samples are also used to select these jets.

The kinematics of the good and fake jet selections are shown in Figure A.1.

[1] In order to select jets with $p_T > 70$ GeV, two single jet triggers are considered with different online jet p_T thresholds. The one with the high threshold is fully efficient to select offline jets with $p_{\mathrm{T}} > 270$ GeV while the one with the low threshold is fully efficient to select offline jets with $p_T > 70$ GeV. Due to its high rate, the lowest threshold trigger is prescaled by a factor of about 10. In all distributions presented in this document, the data recorded by this trigger are normalised taking into account the prescale correction.

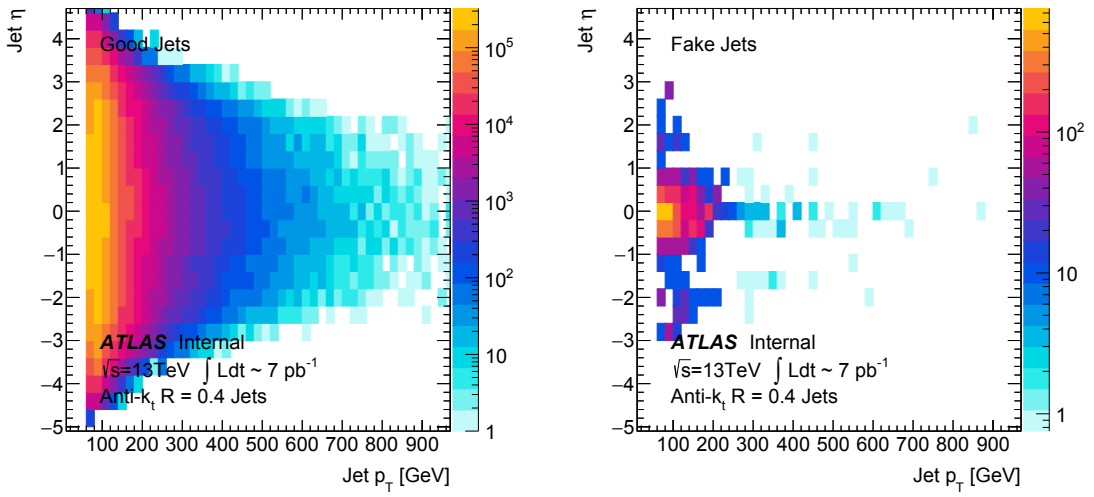


(a) (b)



(c)

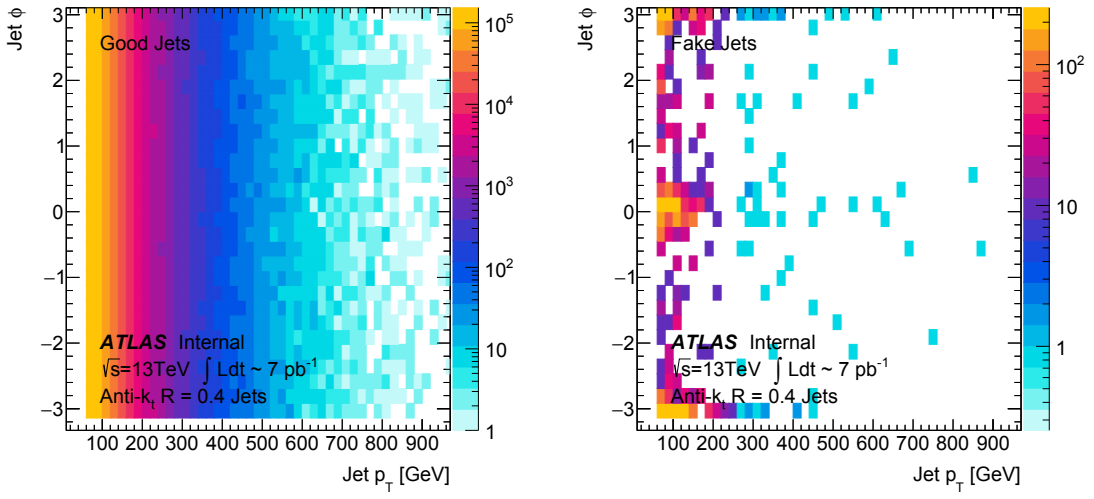
Figure A.1: Distributions of p_T (a), η (b) and ϕ (c) in the good jets enriched sample for both data (black points) and the simulation (blue histograms). Distributions from the fake jets enriched samples are also superimposed (red points). Both selections feature kinematically similar jets. The fake jets selection phi distribution exhibits the typical azimuthal structure of beam-induced backgrounds as in Figure 7.4.



(a) Good jets

(b) Fake jets

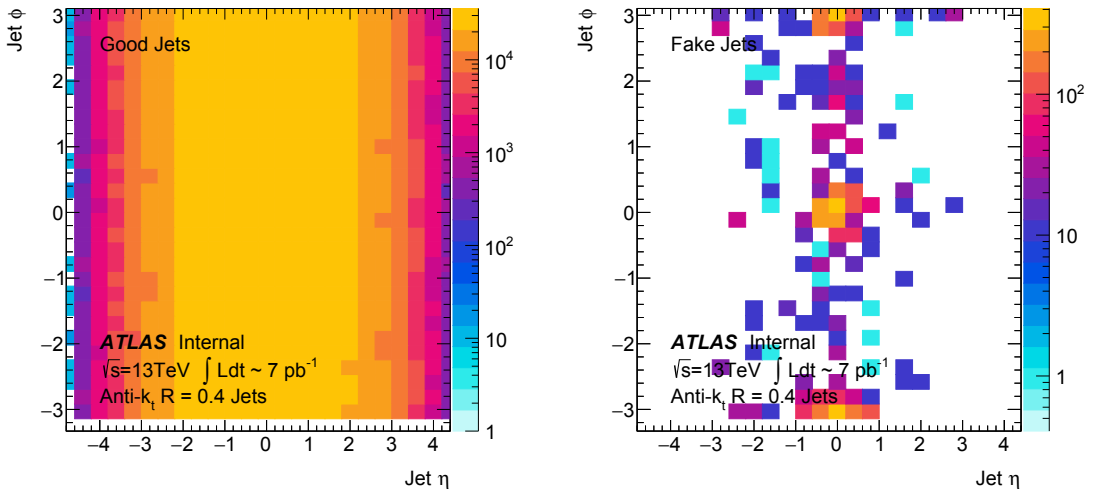
Figure A.2: Distribution of p_T as a function of η for the good (a) and fake (b) jets enriched samples in data.



(a) Good jets

(b) Fake jets

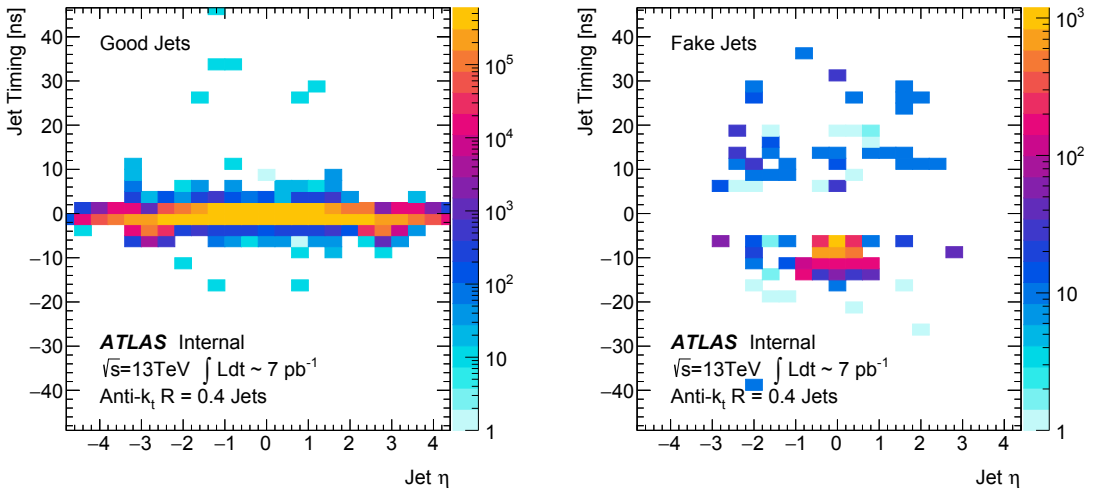
Figure A.3: Distribution of p_T as a function of ϕ for the good (a) and fake (b) jets enriched samples in data.



(a) Good jets

(b) Fake jets

Figure A.4: Distribution of η as a function of ϕ for the good (a) and fake (b) jets enriched samples in data.



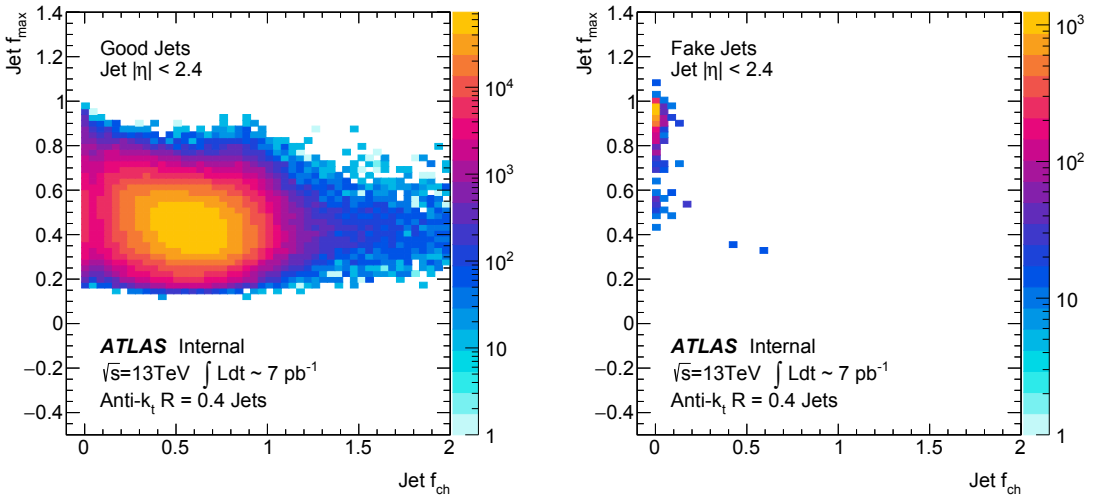
(a) Good jets

(b) Fake jets

Figure A.5: Distribution of η as a function of t_{jet} for the good (a) and fake (b) jets enriched samples in data.

A.2 Correlations between Jet Quality Variables

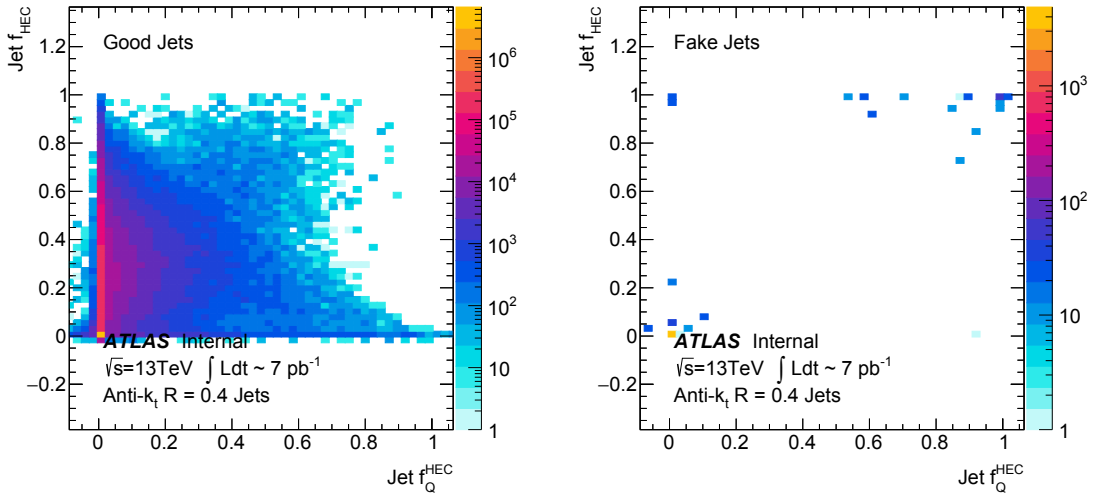
Interesting features of the good and fake jets are revealed when examining correlations between jet quality variables.



(a) Good jets

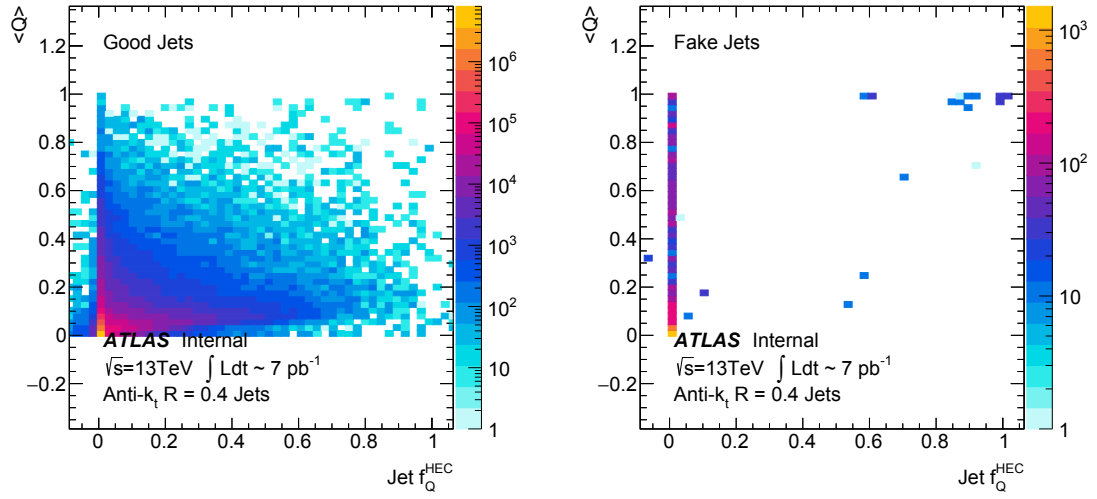
(b) Fake jets

Figure A.6: Distribution of f_{ch} as a function of f_{max} for the good (a) and fake (b) jets enriched samples in data.



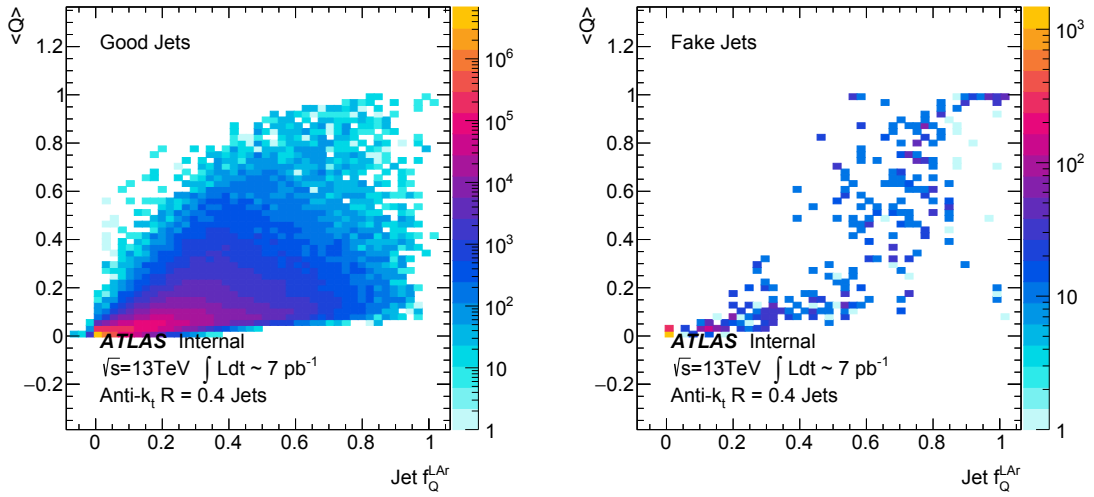
(a) Good jets (b) Fake jets

Figure A.7: Distribution of f_Q^{HEC} as a function of f_{HEC} for the good (a) and fake (b) jets enriched samples in data.



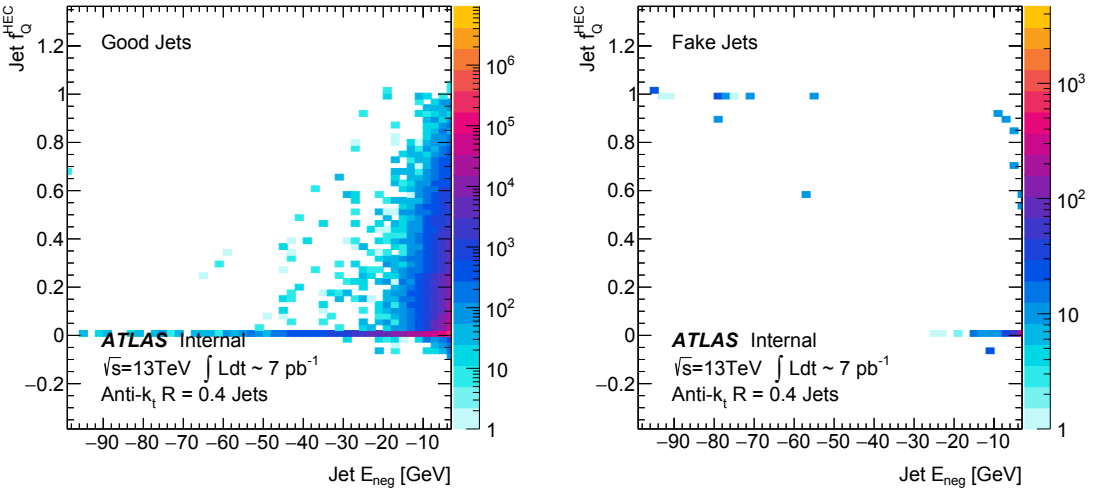
(a) Good jets (b) Fake jets

Figure A.8: Distribution of f_Q^{HEC} as a function of $\langle Q \rangle$ for the good (a) and fake (b) jets enriched samples in data.



(a) Good jets (b) Fake jets

Figure A.9: Distribution of f_Q^{LAr} as a function of $\langle Q \rangle$ for the good (a) and fake (b) jets enriched samples in data.

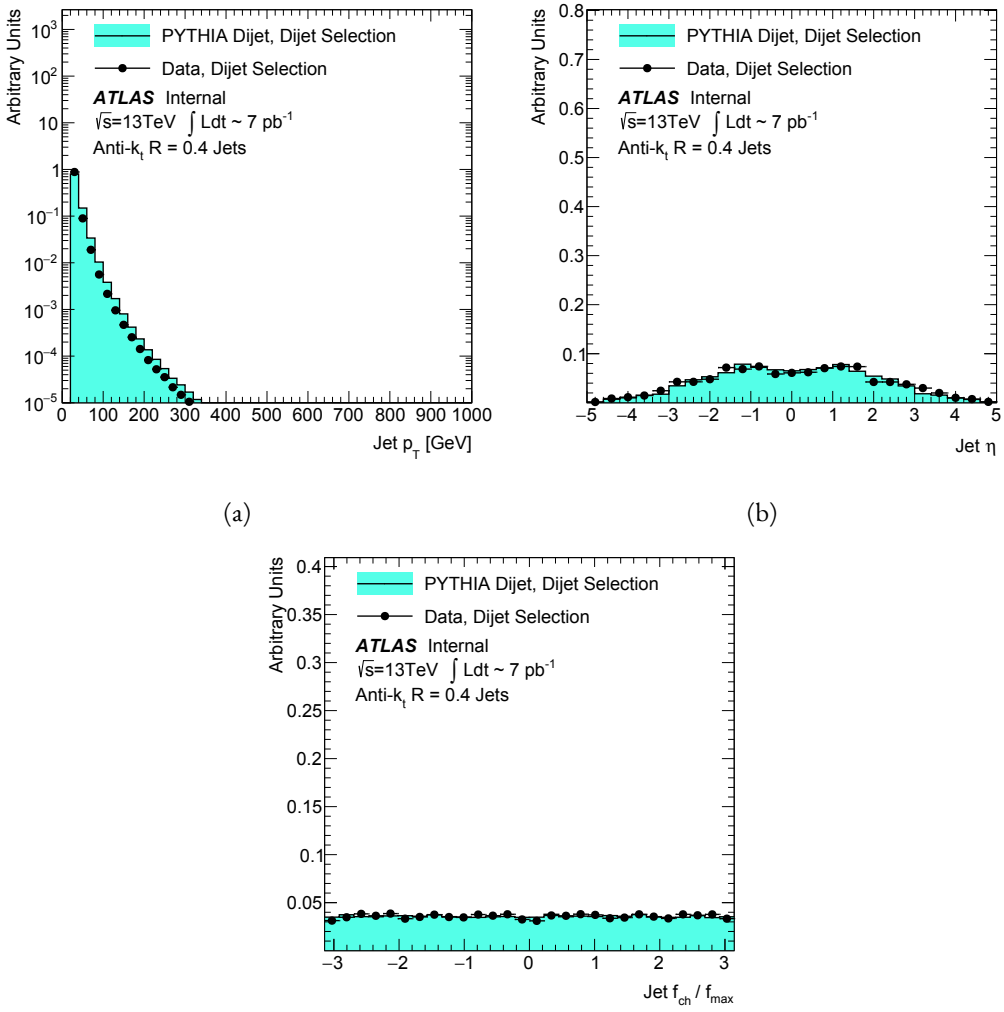


(a) Good jets (b) Fake jets

Figure A.10: Distribution of E_{neg} as a function of f_Q^{HEC} for the good (a) and fake (b) jets enriched samples in data.

A.3 Jet Quality Variables at Low p_T

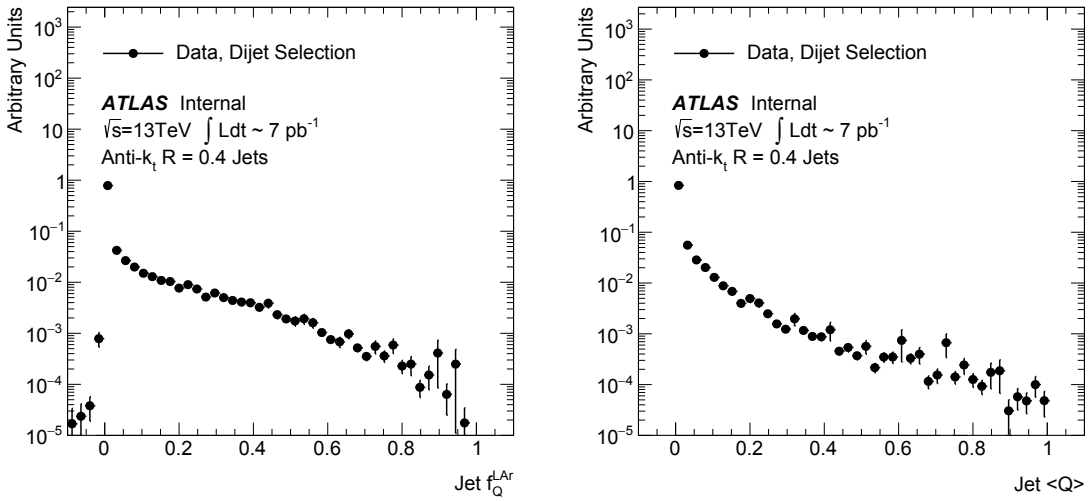
The good jet topology was extended to low-p_T to ensure that the jet quality variables were understood in this regime.



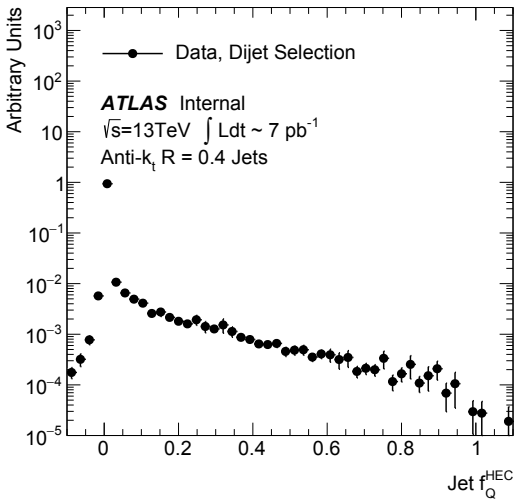
(a) (b)

(c)

Figure A.11: Distributions of p_T (a), η (b), and ϕ (c) in the loose good jets sample (p_T cut relaxed to 20 GeV) for both data (black points) and the simulation (green histograms).

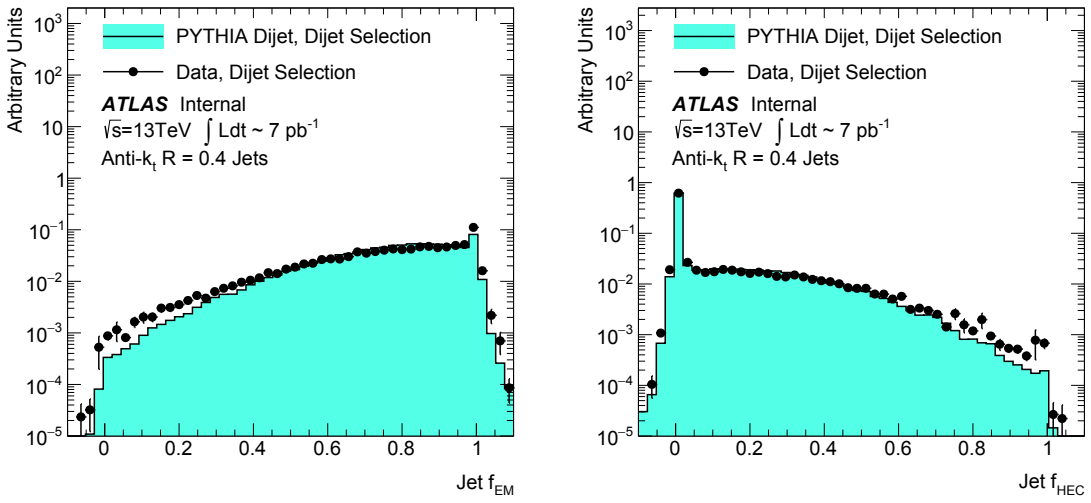


(a) (b)

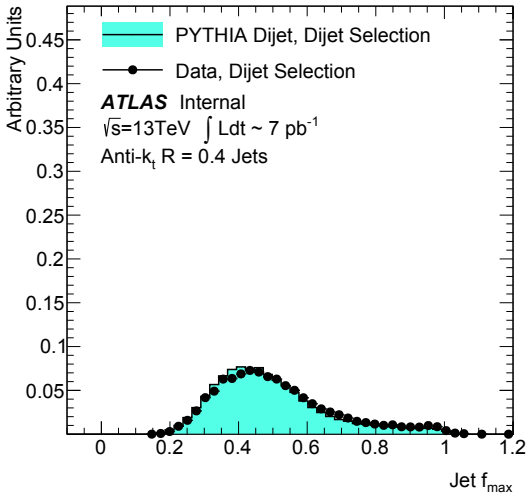


(c)

Figure A.12: Distributions of f_Q^{LAr} (a), $\langle Q \rangle$ (b), and f_Q^{HEC} (c) in the loose good jets sample (p_T cut relaxed to 20 GeV) for data (black points).

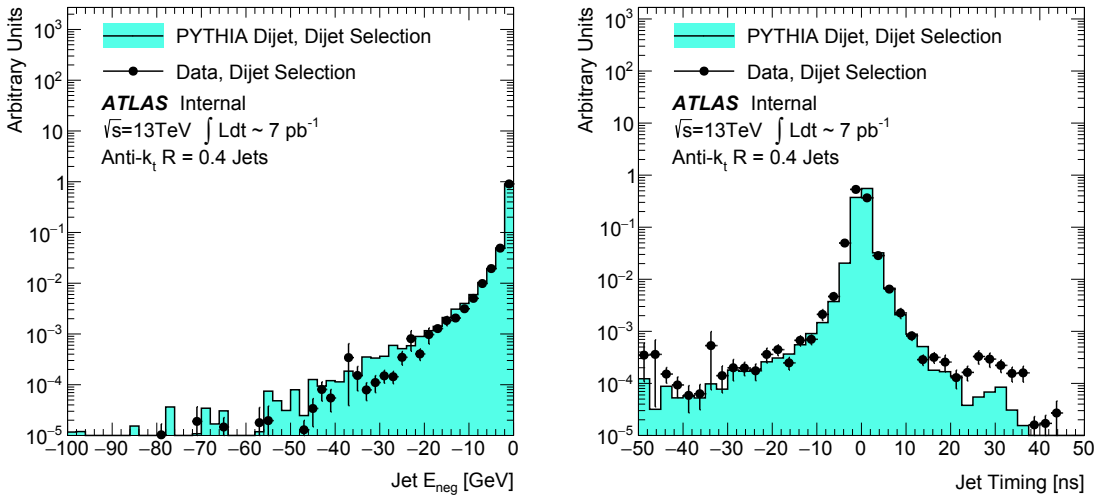


(a) (b)



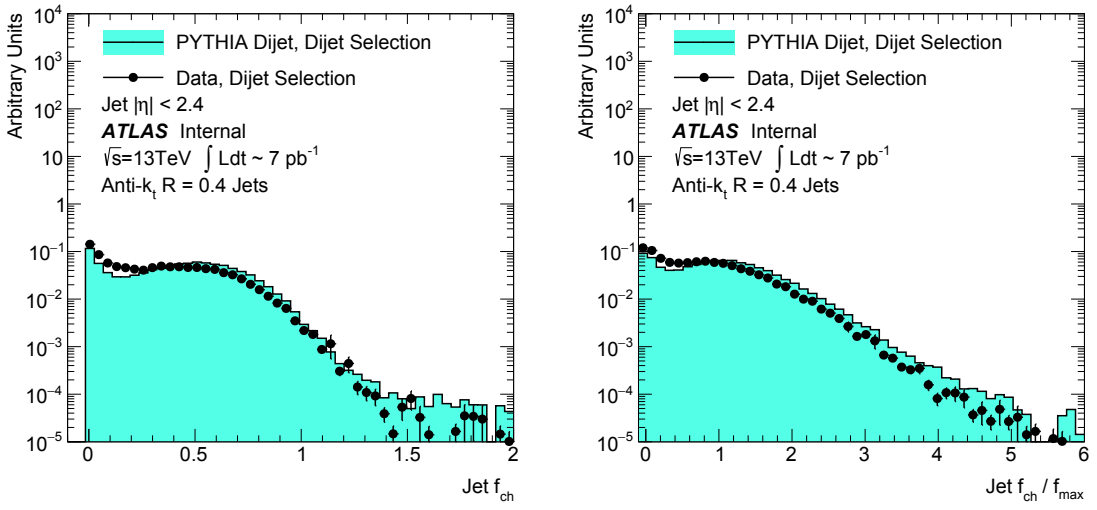
(c)

Figure A.13: Distributions of f_{EM} (a), f_{HEC} (b) and f_{max} (c) in the loose good jets sample (p_T cut relaxed to 20 GeV) for both data (black points) and the simulation (green histograms).



(a) (b)

Figure A.14: Distributions of E_{neg} (a) and t_{jet} (b) in the loose good jets sample (p_T cut relaxed to 20 GeV) for both data (black points) and the simulation (green histograms).



(a) (b)

Figure A.15: Distributions of f_{ch} (a) and f_{ch}/f_{max} (b) for $|\eta| < 2.4$ in the loose good jets sample (p_T cut relaxed to 20 GeV) for both data (black points) and the simulation (green histograms).

B

Beam Background Tagging Efficiency

The estimation of non-collision background in the signal region is obtained by correcting the number of events tagged as beam–induced–background by the efficiency of the tagger, as described in Section 7.2. However, several different sets of cuts can be applied on top of the signal region selection to construct a bib-enriched sample, and the measured tagging efficiency is not consistent across different fake jet selections. As the NCB yield in the signal region depends directly on the measured tagger efficiency, the systematic uncertainty on the yield is determined by evaluating the tagger efficiency for three separate BIB–enriched selections:

1. A BadTight jet sample consisting of events in the signal region in which the leading jet fails the tight cleaning criteria. The tagger efficiency measured in this sample is $25 \pm 0.2\%$. Using this efficiency, the total amount of non–collision–background with $E_T^{\text{miss}} > 250$ GeV in the signal region is 113 events.

2. A late jet sample which contains events in the signal region without tight cleaning applied, in which

the leading jet is out-of-time with $t > 5$ ns. The tagger efficiency measured in this sample is $45 \pm 0.7\%$. With this efficiency, the total amount of non–collision–background with $E_T^{\text{miss}} > 250$ GeV in the signal region is 63 events.

3. An early jet sample of events in the signal region without tight cleaning applied, in which the leading jet is out-of-time with $t < -5$ ns. The tagger efficiency measured in this sample is $22 \pm 0.4\%$. With this efficiency, the total amount of non–collision–background with $E_T^{\text{miss}} > 250$ GeV in the signal region is 128 events.

As the BadTight jet sample also includes all out–of–time jets (as shown in Figure B.1), the efficiency calculated from this selection is used for the nominal estimation of the non–collision–background yield of 113 events. As the early and late jet selections respectively produce NCB estimations of 128 and 63 events, a conservative 100 % systematic uncertainty is put on the NCB estimation. [1]

[1] The different tagging efficiency measured for the jets with $t \leq 0$ and $t > 0$ is likely due to the position of the CSC readout window. The fake jets with $t \leq 0$ are associated to the nominal radio-frequency bucket where the beam-induced muon create a signal in the incoming CSC station just at the edge of its readout window. The jets with $t > 0$ are associated with de-bunched ghost charge from later radio-frequency buckets and therefore the beam-induced muons arrive at least by 2.5ns later. This positions them further into the CSC readout window, resulting in higher efficiency of the tagging method.

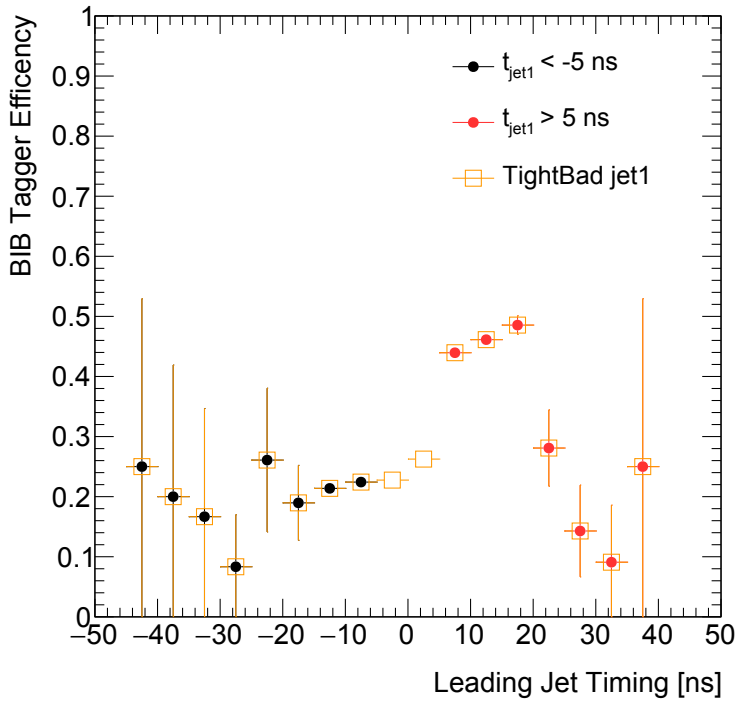


Figure B.1: The BIB tagger efficiency as a function of jet time for the three different BIB-enriched selections. The badTight sample selects all jets with $|t| > 5$.

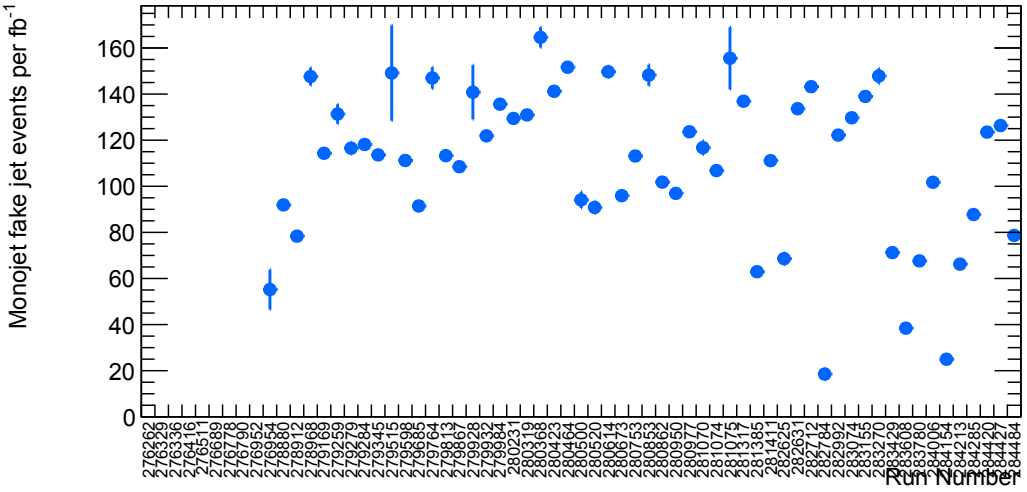


Figure B.2: The evolution of the fake jet rate in the full dataset, evaluated as the number of events in the BIB–enriched selection (for $E_T^{\text{miss}} > 250$ GeV) per 1 fb^{-1} of data.

C

Search for Dijet Resonances

C.1 Overview

The dijet analysis [124] is a search for massive particles decaying into jet pairs. As any new particles produced in LHC collisions must interact with the partons of the proton, the new particles can also produce quarks or gluons in the final state. The dijet analysis looks for mass resonances in the dijet spectrum, shown in Figure C.1. In the absence of any excess, this channel provides a powerful constraint on strongly coupled new physics.

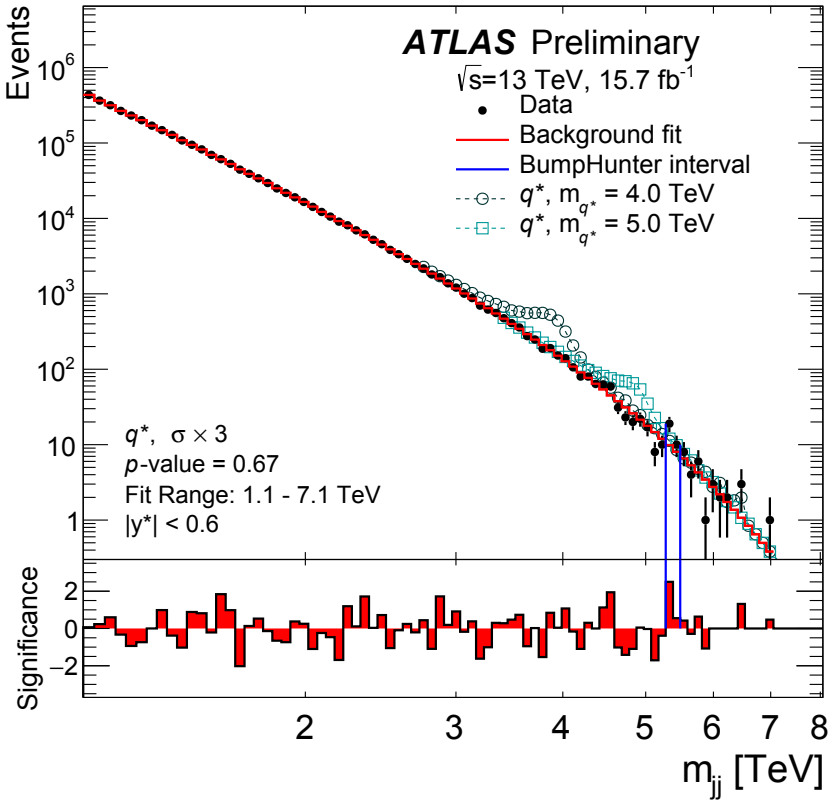


Figure C.1: The reconstructed dijet mass m_{jj} distribution using the data collected by the ATLAS detector in 2015 and 2016, corresponding to an integrated luminosity of 3.5 fb^{-1} and 12.2 fb^{-1}, respectively [124]. No excess is observed.

C.2 Limits

Limits on $q\bar{q} \to Z' \to q\bar{q}$ are presented for a selection of dijet searches to complement the limits shown in Figures 8.6 and 8.7.

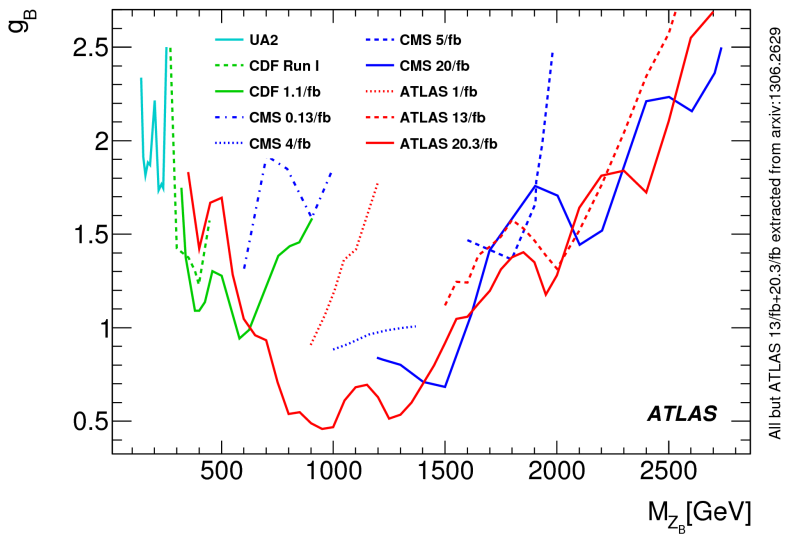


Figure C.2: 95%CL upper limits on predicted cross-section as a function of the coupling to quarks $g_B = 6g_q$ and the mass M_Z obtained from the$\sqrt{s} = 8$ TeV m_{jj} distribution [121].

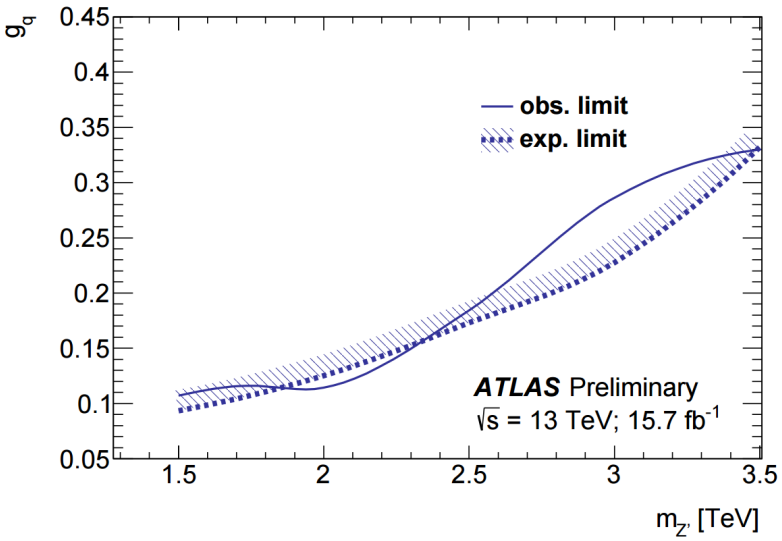


Figure C.3: 95%CL upper limits on predicted cross-section as a function of the coupling to quarks g_q and the mass M_Z obtained from the $\sqrt{s} = 13$ TeV m_{jj} distribution [124].

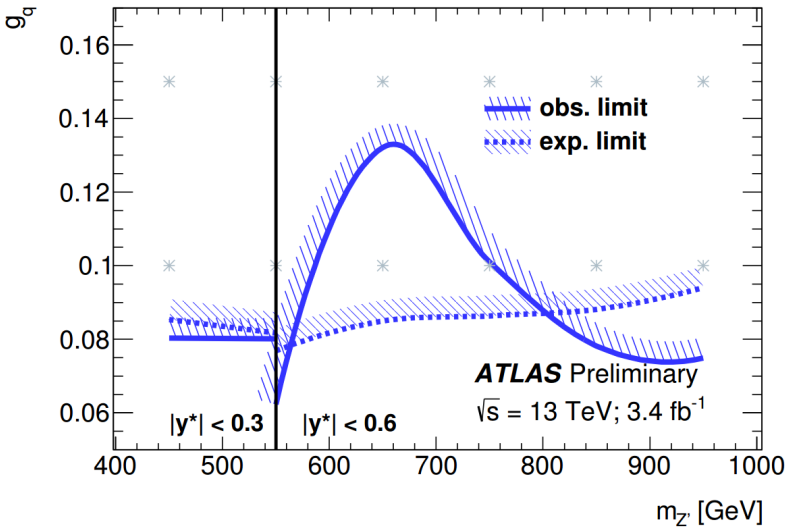


Figure C.4: 95%CL upper limits on predicted cross-section as a function of the coupling to quarks g_q and the mass M_Z obtained from the $\sqrt{s} = 13$ TeV trigger-level m_{jj} distribution [123].

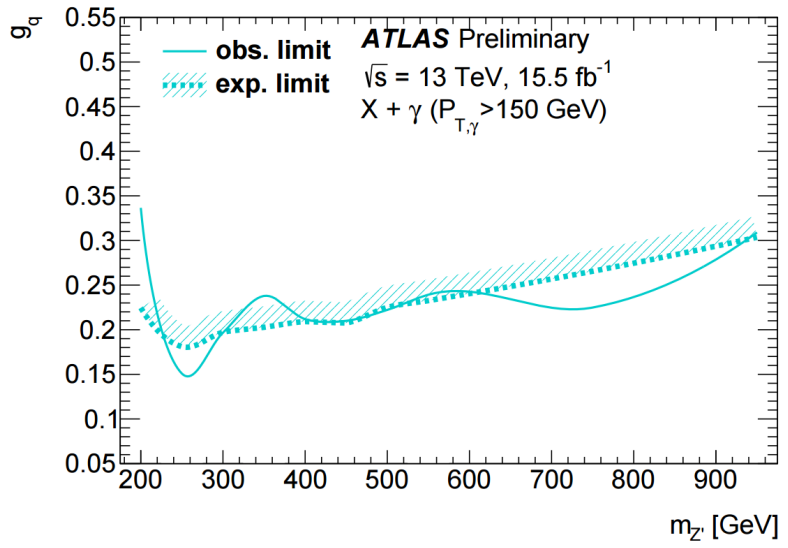


Figure C.5: 95%CL upper limits on predicted cross-section as a function of the coupling to quarks g_q and the mass M_Z obtained from the $\sqrt{s} = 13$ TeV dijet + ISR m_{jj} distribution [122].

References

[1] Gianfranco Bertone, Dan Hooper, and Joseph Silk. Particle dark matter: evidence, candidates and constraints. *Physics Reports*, 405(5–6):279 – 390, 2005. ISSN 0370-1573. doi: http://dx.doi.org/10.1016/j.physrep.2004.08.031. URL http://www.sciencedirect.com/science/article/pii/S0370157304003515.

[2] Gerard Jungman, Marc Kamionkowski, and Kim Griest. Supersymmetric dark matter. *Physics Reports*, 267(5):195 – 373, 1996. ISSN 0370-1573. doi: http://dx.doi.org/10.1016/0370-1573(95)00058-5. URL http://www.sciencedirect.com/science/article/pii/0370157395000585.

[3] ATLAS Collaboration. The ATLAS experiment at the CERN Large Hadron Collider. *JINST*, 3: S08003, 2008. doi: 10.1088/1748-0221/3/08/S08003.

[4] ATLAS Collaboration. Search for new phenomena in final states with an energetic jet and large missing transverse momentum in pp collisions at $\sqrt{s} = 13$ TeV using the atlas detector. *Phys. Rev. D*, 94:032005, Aug 2016. doi: 10.1103/PhysRevD.94.032005. URL http://link.aps.org/doi/10.1103/PhysRevD.94.032005.

[5] M. Milgrom. A modification of the newtonian dynamics - implications for galaxies. *Astrophysical Journal*, 270:371–38, 1983. doi: 10.1086/161131.

[6] K. G. Begeman, A. H. Broeils, and R. H. Sanders. Extended rotation curves of spiral galaxies - dark haloes and modified dynamics. *Monthly Notices of the Royal Astronomical Society*, 249:523–537, 1991. ISSN 0035-8711. doi: 10.1093/mnras/249.3.523.

[7] G.W. Collins. *The virial theorem in stellar astrophysics*. Astronomy and astrophysics series. Pachart Pub. House, 1978. URL https://books.google.com/books?id=F8-7AAAAIAAJ.

[8] F. Zwicky. Die rotverschiebung von extragalaktischen nebeln. *Helvetica Physica Acta*, 6:110–127, 1933.

[9] Aaron D. Lewis, David A. Buote, and John T. Stocke. Chandra observations of a2029: The dark matter profile down to below 0.01rvir in an unusually relaxed cluster. *The Astrophysical Journal*, 586(1):135, 2003. URL http://stacks.iop.org/0004-637X/586/i=1/a=135.

[10] Matthias Bartelmann and Peter Schneider. Weak gravitational lensing. *Physics Reports*, 340(4–5): 291 – 472, 2001. ISSN 0370-1573. doi: http://dx.doi.org/10.1016/S0370-1573(00)00082-X. URL http://www.sciencedirect.com/science/article/pii/S037015730000082X.

[11] J. Anthony Tyson, Greg P. Kochanski, and Ian P. Dell'Antonio. Detailed mass map of cl 0024+1654 from strong lensing. *The Astrophysical Journal Letters*, 498(2):L107, 1998. URL http://stacks.iop.org/1538-4357/498/i=2/a=L107.

[12] J. T. Peebles, P. J. E.; Yu. Primeval adiabatic perturbation in an expanding universe. *Astrophysical Journal*, 162:815, 1970. doi: 10.1086/150713.

[13] Wayne Hu and Scott Dodelson. Cosmic microwave background anisotropies. *Annual Review of Astronomy and Astrophysics*, 40(1):171–216, 2002. doi: 10.1146/annurev.astro.40.060401.093926. URL http://dx.doi.org/10.1146/annurev.astro.40.060401.093926.

[14] Planck Collaboration. Planck 2015 results. *Astronomy and Astrophysics*, 594:A11, 2016. doi: 10.1051/0004-6361/201526926. URL http://dx.doi.org/10.1051/0004-6361/201526926.

[15] David Griffiths. *Introduction to elementary particles*. 2008.

[16] F. Halzen and Alan D. Martin. *Quarks and leptons: an introductory course in modern particle physics*. 1984. ISBN 0471887412, 9780471887416.

[17] Christopher G. Tully. *Elementary particle physics in a nutshell*. 2011.

[18] K. A. Olive et al. Review of Particle Physics. *Chin. Phys.*, C38:090001, 2014. doi: 10.1088/1674-1137/38/9/090001.

[19] Matthew D. Schwartz. *Quantum Field Theory and the Standard Model*. Cambridge University Press, 2014. ISBN 1107034736, 9781107034730. URL http://www.cambridge.org/us/academic/subjects/physics/theoretical-physics-and-mathematical-physics/quantum-field-theory-and-standard-model.

[20] S. Dawson. Introduction to electroweak symmetry breaking. In *High energy physics and cosmology. Proceedings, Summer School, Trieste, Italy, June 29-July 17, 1998*, pages 1–83, 1998. URL http://alice.cern.ch/format/showfull?sysnb=0301862.

[21] ATLAS Collaboration. 2016. URL https://atlas.web.cern.ch/Atlas/GROUPS/PHYSICS/CombinedSummaryPlots/SM/index.html.

[22] Scott Dodelson and Lawrence M. Widrow. Sterile neutrinos as dark matter. *Phys. Rev. Lett.*, 72:17–20, Jan 1994. doi: 10.1103/PhysRevLett.72.17. URL http://link.aps.org/doi/10.1103/PhysRevLett.72.17.

[23] Leslie J Rosenberg and Karl A. van Bibber. Searches for invisible axions. *Physics Reports*, 325(1):1 – 39, 2000. ISSN 0370-1573. doi: http://dx.doi.org/10.1016/S0370-1573(99)00045-9. URL http://www.sciencedirect.com/science/article/pii/S0370157399000459.

[24] Kaustubh Agashe and Géraldine Servant. Warped unification, proton stability, and dark matter. *Phys. Rev. Lett.*, 93:231805, Dec 2004. doi: 10.1103/PhysRevLett.93.231805. URL http://link.aps.org/doi/10.1103/PhysRevLett.93.231805.

[25] Lyndon R Evans and Philip Bryant. LHC Machine. *J. Instrum.*, 3:S08001. 164 p, 2008. URL https://cds.cern.ch/record/1129806. This report is an abridged version of the LHC Design Report (CERN-2004-003).

[26] Oliver Buchmueller, Matthew J. Dolan, Sarah A. Malik, and Christopher McCabe. Characterising dark matter searches at colliders and direct detection experiments: vector mediators. *Journal of High Energy Physics*, 2015(1):1–33, 2015. ISSN 1029-8479. doi: 10.1007/JHEP01(2015)037. URL http://dx.doi.org/10.1007/JHEP01(2015)037.

[27] XENON100 Collaboration, E. Aprile et al. Limits on spin-dependent WIMP-nucleon cross sections from 225 live days of XENON100 data. *Phys. Rev. Lett.*, 111(2):021301, 2013. doi: 10.1103/PhysRevLett.111.021301.

[28] LUX Collaboration. Results on the spin-dependent scattering of weakly interacting massive particles on nucleons from the run 3 data of the lux experiment. *Phys. Rev. Lett.*, 116:161302, Apr 2016. doi: 10.1103/PhysRevLett.116.161302. URL http://link.aps.org/doi/10.1103/PhysRevLett.116.161302.

[29] C. Amole et al. Dark matter search results from the PICO-60 CF_3I bubble chamber. *Phys. Rev. D*, 93(5):052014, 2016. doi: 10.1103/PhysRevD.93.052014.

[30] PICO Collaboration, C. Amole et al. Improved Dark Matter Search Results from PICO-2L Run-2. *Submitted to: Phys. Rev. D*, 2016.

[31] Teresa Marrodan Undagoitia and Ludwig Rauch. Dark matter direct-detection experiments. *J. Phys.*, G43(1):013001, 2016. doi: 10.1088/0954-3899/43/1/013001.

[32] The Fermi-LAT Collaboration. The large area telescope on the fermi gamma-ray space telescope mission. *The Astrophysical Journal*, 697(2):1071, 2009. URL http://stacks.iop.org/0004-637X/697/i=2/a=1071.

[33] The Fermi-LAT Collaboration. Searching for dark matter annihilation from milky way dwarf spheroidal galaxies with six years of fermi large area telescope data. *Phys. Rev. Lett.*, 115:231301, Nov 2015. doi: 10.1103/PhysRevLett.115.231301. URL http://link.aps.org/doi/10.1103/PhysRevLett.115.231301.

[34] Lisa Goodenough and Dan Hooper. Possible Evidence For Dark Matter Annihilation In The Inner Milky Way From The Fermi Gamma Ray Space Telescope. Technical report, 2009.

[35] Samuel K. Lee, Mariangela Lisanti, Benjamin R. Safdi, Tracy R. Slatyer, and Wei Xue. Evidence for unresolved γ-ray point sources in the inner galaxy. *Phys. Rev. Lett.*, 116:051103, Feb 2016. doi: 10.1103/PhysRevLett.116.051103. URL http://link.aps.org/doi/10.1103/PhysRevLett.116.051103.

[36] Richard Bartels, Suraj Krishnamurthy, and Christoph Weniger. Strong support for the millisecond pulsar origin of the galactic center gev excess. *Phys. Rev. Lett.*, 116:051102, Feb 2016. doi: 10.1103/PhysRevLett.116.051102. URL http://link.aps.org/doi/10.1103/PhysRevLett.116.051102.

[37] Gary Steigman, Basudeb Dasgupta, and John F. Beacom. Precise relic wimp abundance and its impact on searches for dark matter annihilation. *Phys. Rev. D*, 86:023506, Jul 2012. doi: 10.1103/PhysRevD.86.023506. URL http://link.aps.org/doi/10.1103/PhysRevD.86.023506.

[38] Jalal Abdallah et. al. Simplified models for dark matter searches at the {LHC}. *Physics of the Dark Universe*, 9–10:8 – 23, 2015. ISSN 2212-6864. doi: http://dx.doi.org/10.1016/j.dark.2015.08.001. URL http://www.sciencedirect.com/science/article/pii/S2212686415000163.

[39] Antonio Boveia et. al. Recommendations on presenting LHC searches for missing transverse energy signals using simplified s-channel models of dark matter. Technical Report arXiv:1603.04156. CERN-LPCC-2016-001, Mar 2016. URL https://cds.cern.ch/record/2139134.

[40] H Georgi. Effective field theory. *Annual Review of Nuclear and Particle Science*, 43(1):209–252, 1993. doi: 10.1146/annurev.ns.43.120193.001233. URL http://dx.doi.org/10.1146/annurev.ns.43.120193.001233.

[41] Giorgio Busoni, Andrea De Simone, Enrico Morgante, and Antonio Riotto. On the validity of the effective field theory for dark matter searches at the {LHC}. *Physics Letters B*, 728:412 – 421, 2014. ISSN 0370-2693. doi: http://dx.doi.org/10.1016/j.physletb.2013.11.069. URL http://www.sciencedirect.com/science/article/pii/S0370269313009751.

[42] Daniel Abercrombie et al. Dark Matter Benchmark Models for Early LHC Run-2 Searches: Report of the ATLAS/CMS Dark Matter Forum. 2015.

[43] Mihailo Backović, Antony Martini, Olivier Mattelaer, Kyoungchul Kong, and Gopolang Mohlabeng. Direct detection of dark matter with maddm v.2.0. *Physics of the Dark Universe*, 9–10:37 – 50, 2015. ISSN 2212-6864. doi: http://dx.doi.org/10.1016/j.dark.2015.09.001. URL http://www.sciencedirect.com/science/article/pii/S2212686415000187.

[44] Antonio Boveia et. al. Recommendation of the LHC Dark Matter Working Group. Technical report.

[45] Lyndon Evans. The Large Hadron Collider. *Annual Review of Nuclear and Particle Science*, 61(1): 435–466, 2011. doi: 10.1146/annurev-nucl-102010-130438.

[46] Characterisation and mitigation of beam-induced backgrounds observed in the atlas detector during the 2011 proton-proton run. *Journal of Instrumentation*, 8(07):P07004, 2013. URL http://stacks.iop.org/1748-0221/8/i=07/a=P07004.

[47] J. P. Blewett. 200-GeV Intersecting Storage Accelerators. *eConf*, C710920:501, 1971.

[48] CMS Collaboration. The CMS experiment at the CERN LHC. *Journal of Instrumentation*, 3(08): S08004, 2008. URL http://stacks.iop.org/1748-0221/3/i=08/a=S08004.

[49] LHCb Collaoration. The LHCb Detector at the LHC. *JINST*, 3:S08005, 2008. doi: 10.1088/1748-0221/3/08/S08005.

[50] ALICE Collaboration. The ALICE experiment at the CERN LHC. *Journal of Instrumentation*, 3 (08):S08002, 2008. URL http://stacks.iop.org/1748-0221/3/i=08/a=S08002.

[51] Paul Collier for the LHC team. LHC Machine Status. CERN Resource Review Board, 2015. URL https://cds.cern.ch/record/2063924/files/CERN-RRB-2015-119.PDF.

[52] E Quaranta, R Bruce, L Lari, D Mirarchi, S Redaelli, A Rossi, B Salvachua, and G Valentino. Cleaning Inefficiency of the LHC Collimation System During the Energy Ramp: Simulations and Measurements. (CERN-ACC-2013-0043):3 p, May 2013. URL https://cds.cern.ch/record/1570396.

[53] Track Reconstruction Performance of the ATLAS Inner Detector at $\sqrt{s} = 13$ TeV. Technical Report ATL-PHYS-PUB-2015-018, CERN, Geneva, Jul 2015. URL http://cds.cern.ch/record/2037683.

[54] ATLAS Collaboration. 2012. URL https://twiki.cern.ch/twiki/bin/view/AtlasPublic/EventDisplayStandAlone#20_vertices.

[55] K.A. Olive and Particle Data Group. Review of particle physics. *Chinese Physics C*, 38(9):090001, 2014. URL http://stacks.iop.org/1674-1137/38/i=9/a=090001.

[56] The ATLAS collaboration. Monitoring and data quality assessment of the atlas liquid argon calorimeter. *Journal of Instrumentation*, 9(07):P07024, 2014. URL http://stacks.iop.org/1748-0221/9/i=07/a=P07024.

[57] The ATLAS collaboration. Readiness of the atlas liquid argon calorimeter for lhc collisions. *The European Physical Journal C*, 70(3):723–753, 2010. ISSN 1434-6052. doi: 10.1140/epjc/s10052-010-1354-y. URL http://dx.doi.org/10.1140/epjc/s10052-010-1354-y.

[58] ATLAS Collaboration. ATLAS Trigger Operations Public Results. 2015. URL https://twiki.cern.ch/twiki/bin/view/AtlasPublic/TriggerOperationPublicResults.

[59] Joao Pequenao and Paul Schaffner. An computer generated image representing how ATLAS detects particles. Jan 2013. URL https://cds.cern.ch/record/1505342.

[60] Performance of the ATLAS Inner Detector Track and Vertex Reconstruction in the High Pile-Up LHC Environment. Technical Report ATLAS-CONF-2012-042, CERN, Geneva, Mar 2012. URL https://cds.cern.ch/record/1435196.

[61] Track Reconstruction Performance of the ATLAS Inner Detector at $\sqrt{s} = 13$ TeV. Technical Report ATL-PHYS-PUB-2015-018, CERN, Geneva, Jul 2015. URL https://cds.cern.ch/record/2037683.

[62] Performance of primary vertex reconstruction in proton-proton collisions at $\sqrt{s}$ =7 TeV in the ATLAS experiment. Technical Report ATLAS-CONF-2010-069, CERN, Geneva, Jul 2010. URL https://cds.cern.ch/record/1281344.

[63] W Lampl, S Laplace, D Lelas, P Loch, H Ma, S Menke, S Rajagopalan, D Rousseau, S Snyder, and G Unal. Calorimeter Clustering Algorithms: Description and Performance. Technical Report ATL-LARG-PUB-2008-002. ATL-COM-LARG-2008-003, CERN, Geneva, Apr 2008. URL https://cds.cern.ch/record/1099735.

[64] Georges Aad et al. Topological cell clustering in the ATLAS calorimeters and its performance in LHC Run 1. (arXiv:1603.02934. CERN-PH-EP-2015-304), Mar 2016. URL http://cds.cern.ch/record/2138166.

[65] Matteo Cacciari, Gavin P. Salam, and Gregory Soyez. The Anti-k(t) jet clustering algorithm. *JHEP*, 04:063, 2008. doi: 10.1088/1126-6708/2008/04/063.

[66] Monte Carlo Calibration and Combination of In-situ Measurements of Jet Energy Scale, Jet Energy Resolution and Jet Mass in ATLAS. Technical Report ATLAS-CONF-2015-037, CERN, Geneva, Aug 2015. URL http://cds.cern.ch/record/2044941.

[67] The ATLAS collaboration. Jet energy measurement and its systematic uncertainty in proton–proton collisions at $\sqrt{s} = 7$ tev with the atlas detector. *The European Physical Journal C*, 75 (1):1–101, 2015. ISSN 1434-6052. doi: 10.1140/epjc/s10052-014-3190-y. URL http://dx.doi.org/10.1140/epjc/s10052-014-3190-y.

[68] Matteo Cacciari, Gavin P. Salam, and Gregory Soyez. The catchment area of jets. *Journal of High Energy Physics*, 2008(04):005, 2008. URL http://stacks.iop.org/1126-6708/2008/i=04/a=005.

[69] ATLAS Collaboration. Characterisation and mitigation of beam-induced backgrounds observed in the ATLAS detector during the 2011 proton–proton run. *JINST*, 8:P07004, 2013. doi: 10.1088/1748-0221/8/07/P07004.

[70] ATLAS Collaboration. Monitoring and data quality assessment of the ATLAS liquid argon calorimeter. *JINST*, 9:P07024, 2014. doi: 10.1088/1748-0221/9/07/P07024.

[71] ATLAS Collaboration. Jet energy measurement with the ATLAS detector in proton–proton collisions at $\sqrt{s} = 7$ TeV. *Eur. Phys. J. C*, 73:2304, 2013. doi: 10.1140/epjc/s10052-013-2304-2.

[72] ATLAS Collaboration. Search for new phenomena in final states with an energetic jet and large missing transverse momentum in pp collisions at $\sqrt{s}$ =8 TeV with the ATLAS detector. *Eur. Phys. J. C*, 75(7):299, 2015. doi: 10.1140/epjc/s10052-015-3517-3,10.1140/epjc/s10052-015-3639-7. [Erratum: Eur. Phys. J.C 75,no.9,408(2015)].

[73] ATLAS Collaboration. Tagging and suppression of pileup jets with the ATLAS detector. ATLAS-CONF-2014-018, 2014. URL http://cds.cern.ch/record/1700870.

[74] Improved electron reconstruction in ATLAS using the Gaussian Sum Filter-based model for bremsstrahlung. Technical Report ATLAS-CONF-2012-047, CERN, Geneva, May 2012. URL https://cds.cern.ch/record/1449796.

[75] Electron efficiency measurements with the ATLAS detector using the 2015 LHC proton-proton collision data. Technical Report ATLAS-CONF-2016-024, CERN, Geneva, Jun 2016. URL http://cds.cern.ch/record/2157687.

[76] Muon reconstruction performance in early □ s=13 TeV data. Technical Report ATL-PHYS-PUB-2015-037, CERN, Geneva, Aug 2015. URL http://cds.cern.ch/record/2047831.

[77] Performance of missing transverse momentum reconstruction for the ATLAS detector in the first proton-proton collisions at at $\sqrt{s}$= 13 TeV. Technical Report ATL-PHYS-PUB-2015-027, CERN, Geneva, Jul 2015. URL http://cds.cern.ch/record/2037904.

[78] Expected performance of missing transverse momentum reconstruction for the ATLAS detector at $\sqrt{s} = 13$ TeV. Technical Report ATL-PHYS-PUB-2015-023, CERN, Geneva, Jul 2015. URL https://cds.cern.ch/record/2037700.

[79] T. Gleisberg et al. Event generation with SHERPA 1.1. *JHEP*, 02:007, 2009. doi: 10.1088/1126-6708/2009/02/007.

[80] Tanju Gleisberg and Stefan Höche. Comix, a new matrix element generator. *JHEP*, 12:039, 2008. doi: 10.1088/1126-6708/2008/12/039.

[81] Fabio Cascioli, Philipp Maierhofer, and Stefano Pozzorini. Scattering Amplitudes with Open Loops. *Phys. Rev. Lett.*, 108:111601, 2012. doi: 10.1103/PhysRevLett.108.111601.

[82] Steffen Schumann and Frank Krauss. A Parton shower algorithm based on Catani-Seymour dipole factorisation. *JHEP*, 03:038, 2008. doi: 10.1088/1126-6708/2008/03/038.

[83] Stefan Höche, Frank Krauss, Marek Schönherr, and Frank Siegert. QCD matrix elements + parton showers: The NLO case. *JHEP*, 04:027, 2013. doi: 10.1007/JHEP04(2013)027.

[84] Jun Gao, Marco Guzzi, Joey Huston, Hung-Liang Lai, Zhao Li, et al. The CT10 NNLO Global Analysis of QCD. *Phys.Rev.*, D89:033009, 2014. doi: 10.1103/PhysRevD.89.033009.

[85] Stefano Catani, Leandro Cieri, Giancarlo Ferrera, Daniel de Florian, and Massimiliano Grazzini. Vector boson production at hadron colliders: a fully exclusive QCD calculation at NNLO. *Phys. Rev. Lett.*, 103:082001, 2009. doi: 10.1103/PhysRevLett.103.082001.

[86] Stefano Catani and Massimiliano Grazzini. An NNLO subtraction formalism in hadron collisions and its application to Higgs boson production at the LHC. *Phys. Rev. Lett.*, 98:222002, 2007. doi: 10.1103/PhysRevLett.98.222002.

[87] A. D. Martin et al. Parton distributions for the lhc. *Eur. Phys. J. C*, 63:189, 2009.

[88] S. Frixione, P. Nason, and G. Ridolfi. A Positive-Weight Next-to-Leading-Order Monte Carlo for Heavy Flavour Hadroproduction. *JHEP*, 09:126, 2007.

[89] Torbjorn Sjöstrand, Stephen Mrenna, and Peter Z. Skands. PYTHIA 6.4 Physics and Manual. *JHEP*, 05:026, 2006. doi: 10.1088/1126-6708/2006/05/026.

[90] J. Pumplin, D. R. Stump, J. Huston, H. L. Lai, Pavel M. Nadolsky, and W. K. Tung. New generation of parton distributions with uncertainties from global QCD analysis. *JHEP*, 07:012, 2002. doi: 10.1088/1126-6708/2002/07/012.

[91] Peter Zeiler Skands. Tuning Monte Carlo Generators: The Perugia Tunes. *Phys. Rev. D*, 82:074018, 2010. doi: 10.1103/PhysRevD.82.074018.

[92] D. J. Lange. The EvtGen particle decay simulation package. *Nucl. Instrum. Meth. A*, 462:152, 2001. doi: 10.1016/S0168-9002(01)00089-4.

[93] John M. Campbell, R. Keith Ellis, and Ciaran Williams. Vector boson pair production at the LHC. *JHEP*, 07:018, 2011. doi: 10.1007/JHEP07(2011)018.

[94] Simone Alioli, Paolo Nason, Carlo Oleari, and Emanuele Re. A general framework for implementing NLO calculations in shower Monte Carlo programs: the POWHEG BOX. *JHEP*, 06:043, 2010. doi: 10.1007/JHEP06(2010)043.

[95] Stefano Frixione, Paolo Nason, and Carlo Oleari. Matching NLO QCD computations with Parton Shower simulations: the POWHEG method. *JHEP*, 11:070, 2007. doi: 10.1088/1126-6708/2007/11/070.

[96] Paolo Nason. A New method for combining NLO QCD with shower Monte Carlo algorithms. *JHEP*, 11:040, 2004. doi: 10.1088/1126-6708/2004/11/040.

[97] Ulrich Haisch, Felix Kahlhöfer, and Emanuele Re. QCD effects in mono-jet searches for dark matter. *JHEP*, 12:007, 2013. doi: 10.1007/JHEP12(2013)007.

[98] Richard D. Ball et al. Parton distributions for the LHC Run II. *JHEP*, 04:040, 2015. doi: 10.1007/JHEP04(2015)040.

[99] G. Aad et al. The ATLAS Simulation Infrastructure. *Eur.Phys.J.*, C70:823–874, 2010. doi: 10.1140/epjc/s10052-010-1429-9.

[100] S. Agostinelli et al. GEANT4: A Simulation toolkit. *Nucl. Instrum. Meth. A*, 506:250, 2003. doi: 10.1016/S0168-9002(03)01368-8.

[101] Matteo Cacciari, Gavin P. Salam, and Gregory Soyez. The anti-k_t jet clustering algorithm. *JHEP*, 04:063, 2008. doi: 10.1088/1126-6708/2008/04/063.

[102] ATLAS Collaboration. Jet energy measurement with the ATLAS detector in proton-proton collisions at $\sqrt{s} = 7$ TeV. *Eur. Phys. J. C*, 73:2304, 2013. doi: 10.1140/epjc/s10052-013-2304-2.

[103] ATLAS Collaboration. Muon reconstruction performance of the ATLAS detector in proton–proton collision data at $\sqrt{s}$=13 TeV. 2016.

[104] ATLAS Collaboration. Electron efficiency measurements with the ATLAS detector using the 2012 LHC proton–proton collision data. ATLAS-CONF-2014-032, 2014. URL http://cdsweb.cern.ch/record/1706245.

[105] ATLAS Collaboration. Performance of Missing Transverse Momentum Reconstruction in Proton-Proton Collisions at 7 TeV with ATLAS. *Eur. Phys. J. C*, 72:1844, 2012. doi: 10.1140/epjc/s10052-011-1844-6.

[106] ATLAS Collaboration. Selection of jets produced in 13 TeV proton-proton collisions with the ATLAS detector. ATLAS-CONF-2015-029, 2015. URL http://cds.cern.ch/record/2037702.

[107] ATLAS Collaboration. Characterisation and mitigation of beam-induced backgrounds observed in the ATLAS detector during the 2011 proton-proton run. *JINST*, 8:P07004, 2013. doi: 10.1088/1748-0221/8/07/P07004.

[108] D Salek, D Berge, J Boyd, C Chavez, L Fiorini, and M Huhtinen. Beam Background Identification Method. Technical Report ATL-COM-DAPR-2012-001, CERN, Geneva, Mar 2012. URL https://cds.cern.ch/record/1429602.

[109] ATLAS Collaboration. Search for squarks and gluinos with the ATLAS detector in final states with jets and missing transverse momentum using 4.7 fb^{-1} of $\sqrt{s} = 7$ TeV proton-proton collision data. *Phys. Rev. D*, 87:012008, 2013. doi: 10.1103/PhysRevD.87.012008.

[110] Ansgar Denner, Stefan Dittmaier, Tobias Kasprzik, and Alexander Mueck. Electroweak corrections to monojet production at the LHC. *Eur. Phys. J. C*, 73:2297, 2013. doi: 10.1140/epjc/s10052-013-2297-x.

[111] Ansgar Denner, Stefan Dittmaier, Tobias Kasprzik, and Alexander Mueck. Electroweak corrections to dilepton + jet production at hadron colliders. *JHEP*, 06:069, 2011. doi: 10.1007/JHEP06(2011)069.

[112] Ansgar Denner, Stefan Dittmaier, Tobias Kasprzik, and Alexander Mueck. Electroweak corrections to W + jet hadroproduction including leptonic W-boson decays. *JHEP*, 08:075, 2009. doi: 10.1088/1126-6708/2009/08/075.

[113] ATLAS Collaboration. Search for pair-produced third-generation squarks decaying via charm quarks or in compressed supersymmetric scenarios in pp collisions at $\sqrt{s} = 8$ TeV with the ATLAS detector. *Eur. Phys. J. C*, 75:299, 2015. doi: 10.1140/epjc/s10052-015-3517-3.

[114] Glen Cowan, Kyle Cranmer, Eilam Gross, and Ofer Vitells. Asymptotic formulae for likelihood-based tests of new physics. *Eur. Phys. J. C*, 71:1554, 2011. doi: 10.1140/epjc/s10052-011-1554-0.

[115] Alexander L. Read. Presentation of search results: The CL(s) technique. *J. Phys. G*, 28:2693, 2002. doi: 10.1088/0954-3899/28/10/313.

[116] Felix Kahlhoefer, Kai Schmidt-Hoberg, Thomas Schwetz, and Stefan Vogl. Implications of unitarity and gauge invariance for simplified dark matter models. *Journal of High Energy Physics*, 2016 (2):16, 2016. ISSN 1029-8479. doi: 10.1007/JHEP02(2016)016. URL http://dx.doi.org/10.1007/JHEP02(2016)016.

[117] Planck Collaboration. Planck 2015 results. I. Overview of products and scientific results. 2015.

[118] G. et. al. Hinshaw. Nine-year Wilkinson Microwave Anisotropy Probe (WMAP) Observations: Cosmological Parameter Results. *ApJS*, 208:19, October 2013. doi: 10.1088/0067-0049/208/2/19.

[119] Mikael Chala, Felix Kahlhoefer, Matthew McCullough, Germano Nardini, and Kai Schmidt-Hoberg. Constraining dark sectors with monojets and dijets. *Journal of High Energy Physics*, 2015

(7):1–37, 2015. ISSN 1029-8479. doi: 10.1007/JHEP07(2015)089. URL http://dx.doi.org/10.1007/JHEP07(2015)089.

[120] ATLAS Collaboration. 2016. URL atlas.web.cern.ch/Atlas/GROUPS/PHYSICS/CombinedSummaryPlots/EXOTICS/index.html.

[121] ATLAS Collaboration. Search for new phenomena in the dijet mass distribution using pp collision data at $\sqrt{s} = 8$ TeV with the atlas detector. *Phys. Rev. D*, 91:052007, Mar 2015. doi: 10.1103/PhysRevD.91.052007. URL http://link.aps.org/doi/10.1103/PhysRevD.91.052007.

[122] Search for new light resonances decaying to jet pairs and produced in association with a photon or a jet in proton-proton collisions at $\sqrt{s} = 13$ TeV with the ATLAS detector. Technical Report ATLAS-CONF-2016-070, CERN, Geneva, Aug 2016. URL http://cds.cern.ch/record/2206221.

[123] Search for light dijet resonances with the ATLAS detector using a Trigger-Level Analysis in LHC pp collisions at $\sqrt{s} = 13$ TeV. Technical Report ATLAS-CONF-2016-030, CERN, Geneva, Jun 2016. URL http://cds.cern.ch/record/2161135.

[124] Search for New Phenomena in Dijet Events with the ATLAS Detector at $\sqrt{s}$=13 TeV with 2015 and 2016 data. Technical Report ATLAS-CONF-2016-069, CERN, Geneva, Aug 2016. URL https://cds.cern.ch/record/2206212.

[125] Sensitivity to WIMP Dark Matter in the Final States Containing Jets and Missing Transverse Momentum with the ATLAS Detector at 14 TeV LHC. Technical Report ATL-PHYS-PUB-2014-007, CERN, Geneva, Jun 2014. URL https://cds.cern.ch/record/1708859.